UNIVERSITY OF CALIFORNIA
RIVERSIDE

Whispering Gallery Mode Polymer Fiber Sensors Fabricated by Near-Field Electrospinning

A Dissertation submitted in partial satisfaction
of the requirements for the degree of

Doctor of Philosophy

in

Materials Science and Engineering

by

Joseph Earl Cheeney

March 2019

Dissertation Committee:

Dr. Elaine D. Haberer, Chairperson
Dr. Nosang V. Myung
Dr. Ming Liu

The Dissertation of Joseph Earl Cheeney is approved:

_____

_____

_____

Committee Chairperson

University of California, Riverside

Acknowledgements

I would like to thank my advisor Dr. Elaine D. Haberer without who's help I could not accomplish this research. She guided me in my understanding of the theory of whispering gallery modes, their benefits, and how they can be utilized for sensing applications. She also taught me a lot about thoroughly analyzing data and presenting the new information in a straightforward and cohesive manner. I gained a lot of experience in my years that will be useful in the future.

I would also like to thank Dr. Nosang V. Myung for his guidance in the electrospinning process and for allowing me to use his materials and equipment to perform the fabrication and characterization of these materials.

I am also grateful to my lab mate Stephen T. Hsieh for his help in performing confocal fluorescence measurements, development of the fiber crosslinking process, and for providing valuable insight for the electrospinning and WGM measurement processes.

I would also like to thank Dr. Chris Horner and Dr. Jin Nam for building the near-field electrospinning system during his time at UCR as a graduate student. The equipment served my research purposes well and without it the work would not have been accomplished.

I would also like to thank Dr. Dan Borchardt for training and allowing me to use the equipment in the Analytical Chemistry Instrumentation Facility that were critical for the completion of my research.

I would like to express my gratitude toward my lab mates Tam-Triet Ngo Duc, Joshua Plank, and Zaira Alibay for their participation in my group meeting presentations, which helped me examine my work from a different perspective.

Finally, I would also like to thank my parents who helped me through my time in graduate school with their support and patience. Despite all my challenges, they were always encouraging me to work my hardest. Without their help, I would not have made it this far.

Dedicated to my friends, family,

and parents without whose help I could

not have completed this work.

ABSTRACT OF THE DISSERTATION

Whispering Gallery Mode Polymer Fiber Sensors Fabricated by Near-Field Electrospinning

by

Joseph Earl Cheeney

Doctor of Philosophy, Graduate Program in Materials Science and Engineering
University of California, Riverside, March 2019
Dr. Elaine D. Haberer, Chairperson

Because of their ability to serve in chemical and biological applications, there is a growing need for sensitive, compact, readily fabricated, and inexpensive chemical sensors. In recent years, devices that utilize whispering gallery modes (WGMs) have proven versatile in many such applications, however, these reports have typically used fabrication techniques that are either complex, do not produce sensitive devices, or are costly. One possible solution is to use polymer materials in conjunction with near-field electrospinning (NFES). This direct-write fabrication approach enables fast, yet precise positioning of micron-sized fibers for low-cost, scalable sensor manufacturing. Moreover, NFES can be used to incorporate additional functionality such as emitters for optically active sensing or receptors for enhanced selectivity. Here, fluorescent dye-doped polymer fiber refractive index sensors that support WGMs within the fiber cross-section were demonstrated. Poly(vinyl) alcohol resonators were first simulated with finite-difference time-domain simulations to show that the devices needed to be several microns in size and a few hundred nanometers from the substrate to support resonance. Polymer

solutions of 25 wt% PVA and doped at with varied amounts of Rhodamine 6G were mixed and shown to have consistent physicochemical properties. Resonators were fabricated using NFES by drawing fibers from the polymer solution onto substrates patterned with deep trenches. The electrospun fibers ranged from 2 to 33 μm in diameter, displayed smooth surfaces, and had circular cross sections. Using microphotoluminscence, resonant groups of peaks with Q factors as high as 14,191 were observed in the emission range of the dye, from 590-700 nm. Using size-dependent mode spacing predicted by finite-difference time domain simulations, as well as a mode-fitting technique, the resonances were identified as WGMs. The response of the resonance peaks to exposure to isopropanol and methanol vapors was evaluated using a range of fiber diameters. The fibers were also crosslinked to make them water insoluble and their in-air and in-water resonance capabilities were analyzed. The crosslinked fibers displayed Q factors as high as 19,700 when measured in air and values as high as 7,500 when measured in water. Furthermore, aqueous sensing of ethanol was performed. The WGM resonators fabricated here have demonstrated the potential of near-field electrospun polymer-based fibers for sensing applications.

Table of Contents

Chapter 1. Introduction 1

1.1 Motivation 1

1.2 WGM Resonators 2

1.2.1 Background 2

1.2.2 Whispering Gallery Mode Sensing Mechanisms 5

1.3 WGM Materials, Geometries, and Fabrication Methods 8

1.3.1 Material Selection 9

1.3.2 Fabrication via Near-Field Electrospinning 9

1.4 Research Scope 11

Chapter 2. Finite Difference Time Domain (FDTD) Simulations 14

2.1 Introduction 14

2.2 Experimental Details 14

2.3 Results and Discussion 17

2.3.1 WGM Confirmation in Simulations for the PVA in Air System 18

2.3.2 Analysis of Spectra for the PVA-Air System 18

2.3.3 Analysis of Spectra for the PVA-Water System 24

2.4 Conclusions 28

Chapter 3. Physicochemical and Optical Characterization of PVA and R6G-PVA Solutions 30

3.1 Introduction 30

3.2 Experimental Details 31

3.3 Results and Discussion 34

3.3.1 Physicochemical Characterization of PVA Solutions 34

3.3.2 Optical Characterization of Mixed PVA and R6G-PVA Solutions 36

3.4 Conclusions 41

Chapter 4. Fiber Fabrication and Morphological Characterization 43

4.1 Introduction 43

4.2 Experimental Details 44

4.3 Results and Discussion 47

4.3.1 Effect of Applied Voltage and Stage Speed on Fiber Diameter on SiO_2/Si Substrates 47

4.3.2 Effect of Time on Fiber Diameter 49

4.3.3 Effect of R6G Incorporation on Fiber Diameter 51

4.3.4 Effect of Substrate on Fiber Diameter 52

4.3.5 Scribe Mark Characterization for Suspending Fibers 56

4.3.6 Morphological Characterization of R6G-PVA Fibers on Glass Substrates 58

4.3.7 Crosslinking and Morphological Characterization on Crosslinked Fibers.....59
4.4 Conclusions 63
Chapter 5. WGM Detection, Characterization, and Sensing 66
5.1 Introduction 66
5.2 Experimental Details 67
5.3 Results and Discussion 69
5.3.1 Emission, Mode Assignment, and Polarization Studies 69
5.3.2 Explanation of Peak Groups 72
5.3.3 Free Spectral Range Analysis 74
5.3.4 Quality Factor Analysis 76
5.3.5 Yield Experiment 77
5.3.6 Lasing Experiment 79
5.3.7 Bulk Refractive Index Sensing 79
5.3.7.1 Isopropanol Vapor Sensing of As-Spun Fibers 81
5.3.7.2 Methanol Vapor Sensing 83
5.3.7.3 Refractive Index Sensing in Aqueous with Crosslinked Fibers 85
5.4 Conclusions 89
Chapter 6. Conclusions 94

Chapter 7. Future Work 99

Bibliography 104

Figure List

Figure 1.1: Schematic depicting a WGM in a circular cavity. The black arrows indicate the reflection of light around the inside periphery of the cavity. The lighter green around the resonator represents the evanescent field. 3

Figure 1.2: Schematic denoting the orientation of the **E** and **H** fields for the TM and TE polarizations in a WGM. 4

Figure 1.3: Schematic depicting a typical WGM with resonance on the inside perimeter of a circular cavity before any exposure to an analyte molecule, a) typical WGM sensing process showing an introduction of an analyte, causing an changed environmental refractive index and peak red-shift and b) introduction of the analyte to the system with surface diffusion occurring, initially creating a reduced RI at the edge of the resonator as indicated by the lighter shading of blue. Then moving on to full diffusion of the analyte creating a swollen resonator. Lastly, the peak wavelength tracking with analyte diffusion beginning with stable resonance, a blue-shift upon surface diffusion, and subsequent red-shift as diffusion penetrates deeper into the resonator. 7

Figure 2.1: a) Section of Lumerical FDTD user interface with the various components labelled and b) 2D rendering of simulation with the various components indicated. 15

Figure 2.2: a) Portion of spectra of a 5 μm diameter resonator with first and second order modes present. Electric field profiles are next to their respective peaks with wavelength, radial order, and AMN indicated. b) Spectra of resonators with increasing diameters. 19

Figure 2.3 a) FSR as a function of diameter for the PVA-air system and b) Q factor as a function of diameter. 20

Figure 2.4: a)-f) Electric field profiles of the resonators at increasing diameters and g) plot showing evanescent wave depth and n_{eff} with increasing resonator diameters. 23

Figure 2.5: a) Spectra of resonators at increasing diameters for the in-aqueous system. b) FSR as a function of increasing diameter and c) Q factor as a function of increasing diameter. 25

Figure 2.6: a)-e) Electric field profiles of the resonators at increasing diameters for in-aqueous system and f) plot showing the change in evanescent wave depth and n_{eff} with increasing diameter. 27

Figure 2.7: a) Evanescent wave penetration and Q factors for different modes at increasing wavelengths for the 10 μm in-aqueous system and b)-e) field profiles at increasing mode wavelengths. 29

Figure 3.1: Schematic of solution mixing process. a) PVA and magnetic stir bar placed in vial, b) R6G added, c) Millipore water added, and d) solution mixed in a water bath on a hot plate. 32

Figure 3.2: a) Absorption coefficient spectra of R6G-PVA thin films, b) absorption coefficient vs R6G concentration at selected wavelengths. 37

Figure 3.3: a) emission spectra of thin films and b) normalized intensity vs R6G concentration at 580 nm. 38

Figure 3.4: a) Refractive index vs wavelength for R6G-PVA films and b) average RI between 580 – 700 nm for thin films at their respective concentrations. 40

Figure 4.1: a) Schematic of NFES system showing fiber formation in a zig-zag pattern on a collection substrate and b) Optical image of NFES of R6G-PVA taking place on a glass substrate. The arrow indicates the direction of the stage travel. 45

Figure 4.2: Fiber diameter as a function of stage speed at two voltages. The insets are optical images showing the parallel fiber patterns and reduced fiber diameters at different stage speeds. 47

Figure 4.3: Average fiber diameters as a function of time of electrospinning on two different days. 50

Figure 4.4: Histograms showing fiber diameter distributions of Pure-PVA fibers and R6G-PVA fibers. 51

Figure 4.5: Histogram showing fiber diameter distributions between fibers electrospun at 0.5 mm/s on SiO_2/Si and glass substrates. 53

Figure 4.6: a) Fiber diameter vs stage speed for R6G-PVA fibers on glass substrates, b)-e) optical images showing the different fiber diameters at various stage speeds, and f) fiber distribution histograms of fibers electrospun at different stage speeds. 55

Figure 4.7: Characterization of scribe mark depth showing a) optical image of scribe mark, b) 3D rendering of the scribe mark in a), c) plot monitoring scribe depth along the width of the scribe mark, and d) histogram showing distributions of scribe mark depths over 15 different measurements. 57

Figure 4.8: SEM images showing a) suspended fibers electrospun over a scribe mark, b) and c) perspective and top-down images showing surface texture of electrospun fibers, and d) cross-section of fiber showing circularity. 58

Figure 4.9: Optical images showing taper along the z-axis of the fibers. The scale bar is 100 μm. 59

Figure 4.10: Fiber diameter distribution histograms of R6G-PVA fibers before and after crosslinking treatment. 61

Figure 4.11: Crosslinked fibers a) before and b) after being submerged in water for 24 hours demonstrating their ability to remain viable after exposure to water. Scale bar is 100 μm. 62

Figure 4.12: a) Raman spectra of crosslinked and not crosslinked pure-PVA thin films confirming the presence of GA and, b) and c) SEM images showing surface texture of crosslinked R6G-PVA fibers. 64

Figure 5.1: Schematic of µPL system. The path of the excitation beam is tracked in green and the path of the emission is tracked in red. 68

Figure 5.2: Vapor sensing setup. The sample is placed in a petri dish under the µPL objective. Small volumes of IPA or methanol were pumped into the chamber and the spectrum was incrementally measured. 69

Figure 5.3: Confocal fluorescence image showing R6G fluorescence down the length of the fibers. 70

Figure 5.4: a) Spectra of 4.2 µm fiber showing groups of peaks with different polarizations and b) µPL spectra with polarizer of a 4.7 µm fiber showing longer and shorter wavelength groups of peaks having different polarizations. 71

Figure 5.5: a) Spectra taken at different positions along the z-axis of a fiber showing a change in the peak with dominant intensity from a shorter wavelength to a longer wavelength and b) schematic showing different WGM having dominant excitation along the z-axis of a fiber with a taper. 73

Figure 5.6: a) Spectra showing an increased Q and decreased FSR with increase in diameter and b) plot of FSR vs Diameter of several fibers. 75

Figure 5.7: a) Highest Q peak from the as-spun fibers, b) highest Q peak measured of a crosslinked fiber, and c) plot showing increase in Q with diameter for both as-spun and crosslinked fibers. 78

Figure 5.8: a) Spectra of a fiber at different excitation intensities and b) plot of peak intensity as a function of excitation power. The inset shows the same plot from 0 – 0.5 μW excitation showing linear increase in intensity with power. 80

Figure 5.9: a) Stacked spectra showing the shift of peak wavelength over time exposed to IPA vapor and b) plot tracking change in peak wavelength over time of sensors with three different diameters. 81

Figure 5.10: a) Peak position over time of a 5.1 μm resonator after exposure to methanol and b) peak position over time of a 6.2 μm crosslinked resonator after exposure to methanol. 84

Figure 5.11: a) 15.9 μm fiber submerged in water used for sensing ethanol, b) stacked spectra showing peak shift at different ethanol concentrations in water. 86

Figure 5.12: a) Plot monitoring peak shift with additions of ethanol, and b) plot monitoring peak position at different ethanol concentrations showing a sensitivity of more than 190 nm/RIU. 88

Figure 5.13: a) Stacked spectra presence of groups of peaks as well as peak shift with increased ethanol concentration of an 18.3 μm fiber, b) plot showing peak

wavelength vs RI of sensing experiment showing sensitivity of 156.8 nm/RIU, and c) plot showing reduced Q factor with increased solution RI. 90

Figure 7.1 a) Confocal fluorescence image of CdSe QD doped fiber and b) spectra of fiber showing WGMs along the QD fluorescence backbone. 101

List of Tables

Table 1: Physicochemical properties of R6G-PVA solutions at different dye concentrations. 34

Table 2: Chart comparing WGM devices based on Q factor and diameter. 92

Chapter 1. Introduction

1.1 Motivation

In recent years, there has been an increasing need for highly sensitive, compact, and low-cost sensors capable of detecting and quantifying miniscule changes in the surrounding environment. Typically, small sensors on the micro- or nano- scale show great utility due to their compact design as well as high sensitivity. Micron-scale resonance-based optical sensors have recently been utilized because of their response time, sensitivity, sensing specificity, and low cost. These sensors exploit light confinement in a dielectric material to form an optical cavity. These cavities can only support specific resonant frequencies of light as dictated by the device's geometry and material. Often, the optical cavities can be in the form of distributed bragg reflectors[1–3], photonic crystals[4,5], or whispering gallery mode (WGM). Of these, whispering gallery mode (WGM) resonators are particularly advantageous devices. First discovered by Lord Rayleigh in 1910 in the form of acoustic resonances [6], these devices work by confining light along the periphery of a typically circular higher refractive index (RI) cavity placed in a lower RI environment via total internal reflection. This low-loss confinement allows the light to recirculate inside the cavity many times, making these resonators suitable for low threshold lasing applications. This recirculation at the cavity-environment interface

increases mode interaction with surrounding analytes, making them highly sensitive devices. Furthermore, their compact size makes them easily transportable. These devices can be made from a wide range of dielectric materials including semiconductor[7–12], glass[13–15], and polymers[16–19] and can be classified as either active (having an emitter incorporated) or passive (require optical coupling for detection). Furthermore, their compact size allows them to be fabricated in dense configurations, such as arrays. These devices have demonstrated use in important micro- and nanophotonic devices such as low-threshold lasers[16,17,20], frequency combs[21,22], and waveguides[23] as well as in sensing applications such as bulk chemical sensors[24–28], label-free biosensors at the individual virus[29,30] or individual molecule[13,31–33] levels, and single atomic ion detection[34]. For this work, active polymer WGM resonators were fabricated using an electrospinning process. Their resonance capabilities were quantified and they were used to detect the presence of organic solvent in both vapor and liquid form.

1.2 WGM Resonators

1.2.1 Background

WGMs are a class of geometry dependent resonators made from higher RI dielectric materials surrounded in a lower RI environment. Figure 1 shows a schematic of a WGM resonator. The cavities are typically circular in design which is critical for their

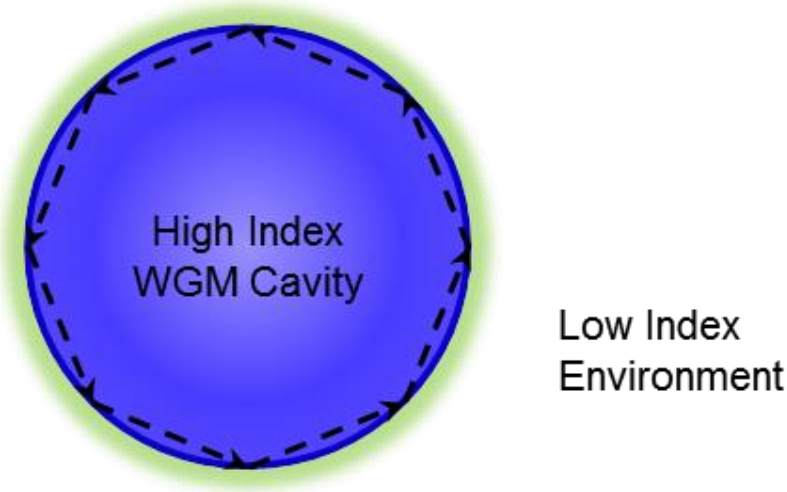

Figure 1.1: Schematic depicting a WGM in a circular cavity. The black arrows indicate the reflection of light around the inside periphery of the cavity. The lighter green around the resonator represents the evanescent field.

function, as discussed later. The light confined inside the resonator reflects around the inside the closed-concave surface of the material (represented by the black dashed arrows) via total internal reflection. To satisfy the requirements for total internal reflection, a high incident angle is required. A small evanescent wave, represented by the green shadow, extends a short distance into the environment.

WGM resonances satisfy the equation:

$$m\lambda = 2\pi R n_{eff} \quad (1)$$

Where "m" is referred to as the azimuthal mode number (AMN) and indicates the integer number of wavelengths that circumnavigate the cavity. "λ" is the mode wavelength, 2πR is the optical path length and the circumference of the device, and "n_{eff}" is a weighted

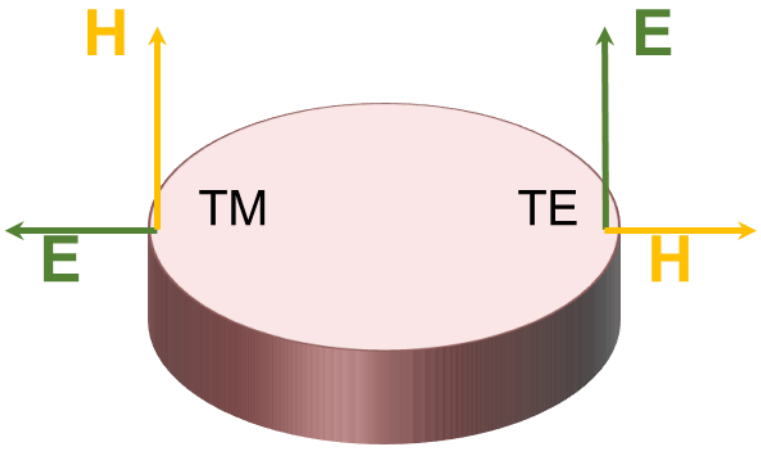

Figure 1.2: Schematic denoting the orientation of the **E** and **H** fields for the TM and TE polarizations in a WGM.

average of the RIs for the mode that exists inside and outside the cavity. The modes in a cavity can have different radial mode orders as well. Radial mode orders describe the number of electric field maxima that exist along the radial direction of the resonator. Furthermore, WGMs support two types of polarizations: transverse magnetic (TM) and transverse electric (TE), as shown in Figure 1.2. TM modes have their electric field vector perpendicular to the resonator surface and TE modes have it parallel to the resonator surface.

Another categorization of WGMs is by having active (fluorescent emitter contained in the cavity) or passive (no fluorescent emitter) resonators. While they are typically more efficient at supporting resonance and are more sensitive, they lack practicality because detecting WGMs in passive cavities requires precise positioning of either an optical fiber or another structure to come within a few hundred nanometers of

the device to allow coupling from a tunable laser [29,31,35]. Active resonators are more practical because a fluorescent emitter, such as a dye[16,28,36], quantum dot[20,37], or rare-earth ions[38,39], is incorporated. These emitters can be excited with an external source such as a laser or LED and the emission couples into the WGM. These WGMs can then be detected using free-space optics. Despite absorption or scattering losses often being associated with active resonators, they can still support high quality resonance. This advantage makes active resonators more practical for many sensing and optical applications, such as lasers.

1.2.2 Whispering Gallery Mode Sensing Mechanisms

Typically, WGMs are used as sensors by detecting a resonance wavelength, λ, shift, though other sensing processes such as Q spoiling[30] and mode splitting exist[33]. There are two primary mechanisms for sensing analytes with a WGM peak shift: either a change in the effective refractive index (a weighted average of the refractive indices between the mode contained in the cavity and the mode outside the cavity in the form of an evanescent wave), n_{eff}, or a change in radius, R. The amount of wavelength shift can be represented with the equation:

$$\frac{\Delta\lambda}{\lambda} = \frac{\Delta R}{R} + \frac{\Delta n}{n} \quad (2)$$

The first, as shown in Figure 1.3a involves a change in n_{eff}. The top of the figure shows a resonator in ambient conditions. An analyte, such as an organic solvent, is introduced into the sensing environment in either a liquid or gaseous solution. The result is a change in the environmental refractive index. Because there is an evanescent wave that extends into the environment, the n_{eff} changes, typically increases, and causes a detectable red-shift of the spectrum.

The second mechanism by which WGMs can sense is an increased optical path length. If the analyte is, for example, a virus or a large molecule that binds to the surface of the resonator, the path length of light can increase, causing a red-shift in peak wavelength. In ordinary WGM systems, sensing an analyte is detected via a peak red-shift, however, it is important to mention another sensing phenomenon observed in WGMs that utilize polymers[40–42] that involves solvent diffusion. When a polymer is exposed to gases or liquids that can diffuse into the resonator, a peak shift based on solvent uptake by the polymer is observed. There are two major processes affecting the WGM mode position: solvent diffusion over the mode volume and polymer swelling and the peak can be tracked as shown at the bottom of Figure 1.3b. Upon exposure, the analyte begins to diffuse into the surface of the resonator over the mode volume. As soon as diffusion begins, the two mechanisms compete for shifting the peak. While the analyte is diffusing over the mode volume, a blue-shift caused by a reduction in n_{eff} is dominant, however, as diffusion goes further into the resonator the blue-shift ceases, polymer swelling beings to dominate, causing in increase in R and a subsequent red-shift is observed.

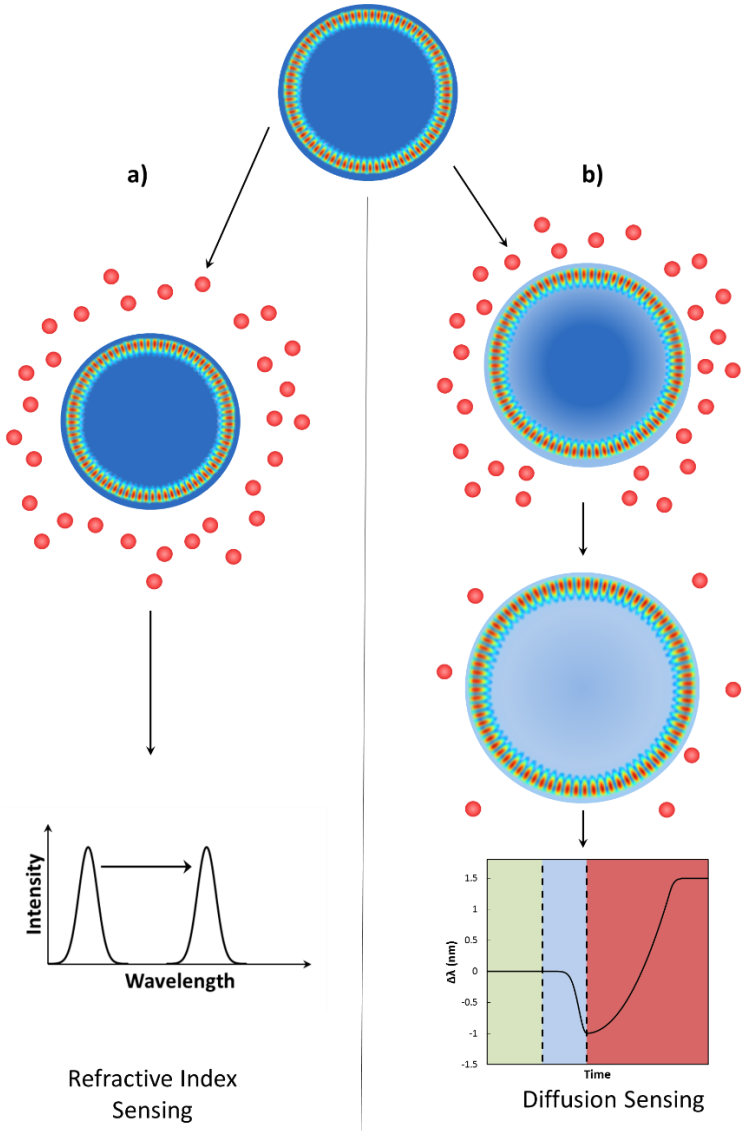

Figure 1.3: Schematic depicting a typical WGM with resonance on the inside perimeter of a circular cavity before any exposure to an analyte molecule, a) typical WGM sensing process showing an introduction of an analyte, causing an changed environmental refractive index and peak red-shift and b) introduction of the analyte to the system with surface diffusion occurring, initially creating a reduced RI at the edge of the resonator as indicated by the lighter shading of blue. Then moving on to full diffusion of the analyte creating a swollen resonator. Lastly, the peak wavelength tracking with analyte diffusion beginning with stable resonance, a blue-shift upon surface diffusion, and subsequent red-shift as diffusion penetrates deeper into the resonator.

1.3 WGM Materials, Geometries, and Fabrication Methods

While these WGM devices have demonstrated high levels of performance, they are often inhibited by the complexity and cost of their fabrication, their lack of manufacturing scalability, or the precise alignment required for measurements. Ideally, a WGM device will have a simple and scalable fabrication technique, with easy measurement methods, and precise and orderly placement. Polymer-based resonators can satisfy some of these requirements because they have easier processability, allowing them to be fabricated with several different techniques and geometries. For instance, Grossmann et. al. used photolithography and a surface-tension induced smoothing technique to make conical-shaped resonators[16,43] and others have used photolithography to make microdisk and microring resonators[44–46].While it can produce many resonators in a small area, photolithography, is expensive and requires cleanroom facilities. Microspheres are an easily produced and common geometry utilized for WGM resonators having shown repeated capabilities in sensing and lasing[19,36,37,47], however, they lack precise and ordered deposition. Polymer fibers have also demonstrated WGM capabilities and can be produced with inexpensive fabrication methods. For instance, Anand et. al. and Linslal et. al. produced a hollow dye-doped polymer fibers via a thermal drawing method[48,49]. Ta et. al. produced poly(methyl methacrylate) fibers via a direct drawing method[17,21]. Gu et. al. made polymer bottle resonators on an optical fiber via a self-assembly technique[50].While these methods are inexpensive, they have not yet shown to produce fiber with orderly deposition and scalability, which may find application for device arrays and multiplexed sensing.

1.3.1 Material Selection

Poly(vinyl) Alcohol (PVA) is a well-studied polymer that was chosen for the host matrix. It is water soluble, non-toxic, biocompatible, and inexpensive. It is comprised of repeated carbon chains with a single -OH functional group. Typically, the molecular weight of PVA ranges from around 9000 g/mol – 186,000 g/mol. Like many carbon-based polymers, PVA absorbs in the UV region, but remains transparent through the visible spectral region, making it advantageous for optical applications in the visible wavelength range. It has a refractive index of around 1.5 in the visible region [51]. PVA has shown to have a breadth of applications including textiles [52], biomedical applications [53], and adhesives [54].

Rhodamine 6G was chosen as the fluorescent dye because it is also water soluble, well-studied, has a very high quantum yield of 0.95 [55], and is inexpensive. Though its optical properties vary slightly depending on the matrix and the concentration, in PVA, it displays its highest absorption peak at 537 nm and it has a peak emission intensity around 558 nm. These properties have made it useful for applications in dye-lasers [17,56], biological marking [57], and WGM resonators [16,17,58].

1.3.2 Fabrication via Near-Field Electrospinning

One promising technique for high-volume, rapid manufacturing of polymer fiber WGM cavities is electrospinning. By adjusting the spinning parameters, this method can

be used to fabricate various morphologies and structures including simple homogeneous, bead-like, porous, hollow, and coaxial core-shell polymer fibers, among others[59]. A straightforward apparatus is used to pump a polymer solution through a hypodermic needle positioned a few centimeters from the substrate (or collector). A voltage applied between the needle and collector draws the solution from the needle, depositing fibers on the collector. Electrospinning has been used to fabricate a handful of active optical resonators used as lasers[60–63] and organic solvent vapor sensors[64]. Reports include dye-doped polymer fibers which support Fabry-Perot modes along their length[62] and 3-D resonances within their non-circular cross-sections[60]. In addition, random electrospun fiber networks have formed ring resonators[64] and electrospun fibers on which charged microdroplets of polymer gain medium were deposited have generated bead-like, bottle microresonators[63]. While electrospinning can rapidly produce many fibers, it lacks the ability to precisely position fibers on a substrate. Recently, a similar technique called near-field electrospinning (NFES) has emerged[65]. Notably, NFES has demonstrated the precision and control required to fabricate well-organized fiber meshes[66], as well as to suspend fibers between posts just a few tens of microns in diameter[67]. Typically, the polymer fibers produced by NFES thus far are on the order of tens to hundreds of nanometers in diameter, too small to support high quality WGMs.

1.4 Research Scope

In this work, we first simulated, then fabricated and investigated NFES of micron-scale, dye-doped poly(vinyl) alcohol (PVA) fibers, and the high quality (Q) optical resonances supported by their smooth, circular cross-sections. Sizeable weight percent solutions of high molecular weight PVA were used in conjunction with reduced stage speeds to direct write suspended fibers approximately 2 to 33 μm in diameter. The emission from these slightly tapered, optically-active resonators revealed groups of sharp peaks ascribed to a combination of WGMs and spiral or conical modes. The longest wavelength peak within each group was identified as an in-plane WGM using mode polarization, Mie theory-based mode assignment, and free spectral range (FSR) measurements over a range of diameters. WGM quality factors as high as ~14,000 were observed for larger fiber diameters. The NFES fibers were crosslinked via glutaraldehyde (GA) treatment, increasing the maximum measured WGM cavity Q to approximately 19,700. Finally, bulk refractive index sensing was achieved using isopropanol (IPA) or methanol vapor and for in-air sensing and ethanol-water as an aqueous model system. The success of NFES, a potentially low-cost, large-scale manufacturing technique, in producing micron-sized fibers that support WGMs and are highly sensitive to environmental changes is an important step toward scalable production of affordable chemical sensors and biosensors.

Chapter 2 discusses the Finite-Difference Time-Domain (FDTD) simulations performed to determine the size range of resonators that would need to be fabricated to support WGM resonance. The simulations also provided valuable insight into the

expected FSRs, Q factors, evanescent field penetration, and n_{eff} values across a range of diameters that the system would produce for both in-air and in-aqueous systems.

In Chapter 3, the process for mixing the PVA and R6G-PVA solutions is developed and shown to be repeatable. The solutions were characterized for their physicochemical properties to determine baseline solution parameters and because the solution and physicochemical properties heavily influence fiber morphology during electrospinning. The solutions were also spin-coated and optically characterized for absorption, emission, and RI over a range of R6G concentrations and wavelengths to determine which would be best for supporting resonance.

Chapter 4 describes the NFES of the dye-polymer solutions. Parameters such as applied voltage, substrate, and stage speed are varied to determine their effect on fiber morphology, specifically fiber diameter, to produce fibers of the size necessary to support WGM resonance. Morphological characterization was done on fibers to exhibit the writing pattern and the ability to suspend fibers, as well as show the fiber's diameters, surface roughness and circularity. Fibers that have been crosslinked are also characterized for the presence of the crosslinking agent, and morphologically characterized for diameter and surface roughness for comparison with as-spun fibers. The fibers are also demonstrated to be water-stable, an important quality for later aqueous sensing experiments.

Chapter 5 begins by showing optical characterization that was done on the electrospun fibers, namely photoluminescence and confocal fluorescence measurements

to demonstrate dye incorporation and dye uniformity into the fibers. WGM resonance was also demonstrated and characterized for its FSR and Q factors and was compared to earlier simulations. It was shown that NFES is a viable fabrication method for micron-scale PVA WGM resonators with Q factors that are very competitive with other dye-doped polymer WGM systems. Because device sensitivity will change with resonator size, sensing experiments are shown over a range of fiber diameters, demonstrating the ability for these WGM devices to detect a change in the surrounding environment via vapor diffusion into the resonators. Furthermore, WGM resonance and ethanol sensing is demonstrated and quantified for aqueous solutions when using crosslinked fibers.

This dissertation shows that NFES can be successfully utilized to fabricate fibers that contain high-quality WGM resonance Furthermore, the fibers can be utilized for vapor and aqueous sensing applications. This work would aid in utilizing NFES for WGM sensor fabrication. Future work could include incorporating receptor materials for sensor specificity, multiplexing for simultaneous analyte detection, and optical applications such as lasing.

Chapter 2. Finite Difference Time Domain (FDTD) Simulations

2.1 Introduction

To simulate the WGMs, finite-difference time-domain (FDTD) simulations were performed (Lumerical FDTD). The simulation software is a 2-D or 3-D time-dependent Maxwell equation solver for nano- or micron-scale photonic devices. The software sets up a mesh grid set to a specified resolution then solves Maxwell's equations inside each grid box, assuming continuous boundary conditions. Typically, a smaller mesh grid increases resolution, but demands longer computing time. Performing the simulations allowed for the visualization and analysis of the WGMs via their squared electric field profiles and spectra for both in-air and in-aqueous systems. Specifically, important properties were determined such as the minimum size device that could support resonance, how resonance changed with diameter, and how far the evanescent wave penetrated into the surrounding environment.

2.2 Experimental Details

Figure 2.1a,b shows portions of the software's user interface. The left-hand column shown in Figure 2.1a contains icons for all the simulations components to be

defined and Figure 2.1b shows a schematic with the simulation components labelled. These components are the object, the environment, excitation sources, the mesh size (which dictates accuracy), spectrum monitors, field profiles at specified resonant wavelengths, a field decay monitor, and Q factor monitors and are labelled in the figure. Since our WGMs were contained in the cross-sections of a fiber, a 2-D material with refractive index 1.50 (set to match PVA[51]) was placed in the center of the simulation region. Furthermore, using a 2-D material substantially reduced computational time.

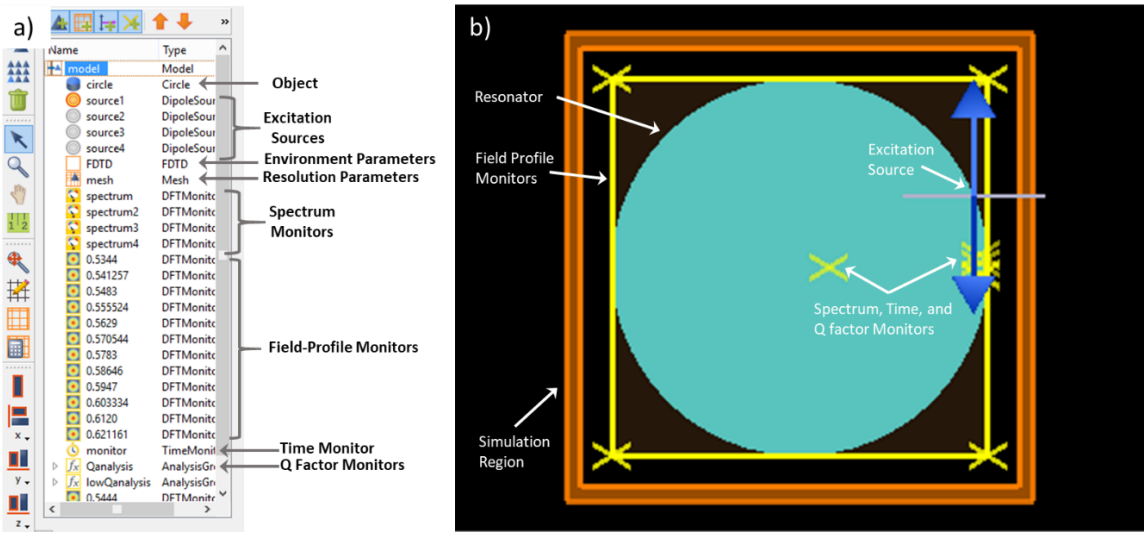

Figure 2.1: a) Section of Lumerical FDTD user interface with the various components labelled and b) 2D rendering of simulation with the various components indicated.

The diameter of the cross-section was varied for the simulations, but was kept on the micron-scale, as that is the size range of many comparable polymer WGM resonators. The surrounding environment, represented by the icon labeled “FDTD”, was sized to fully encapsulate the 2D circle past its boundary. Initially, the environment had an index

of refraction set to 1, because the system was in air. For water simulations, the index of refraction was changed to 1.333, the well-known refractive index of water. The mesh-region was defined to also encapsulate the entire system with a specified mesh size. The mesh size was used using an automated function that was built into the software to perform a simulation that gave a good balance of accuracy and time.

Multiple dipole emission sources were placed a few tens of nanometers inside the cross-section because they act as a point source resonator, and appropriately model fluorescent dye emission. They were placed near the edge of the cross-section to facilitate WGM resonance to minimize selection of Fabry-Perot resonances across the diameter. Their peak emission wavelength was set at 580 nm and the emission profile ranged from 500 nm – 700 nm. Furthermore, they were all oriented such that only one mode polarization (TM) would appear in the spectra and field profiles. Multiple spectrum monitors for analyzing electric field intensity as a function of wavelength were also placed a few tens of nanometers inside and along the edge of the cross-section to capture the WGM resonances at the position of the mode. Because a single monitor would not lie perfectly on a mode across all wavelengths, the spectra reported are an average of four spectra, each taken from one of these spectrum monitors. The simulations were set to run for 2000 femtoseconds to allow the resonance ample time to decay, which is important for the Q factor analysis. A time monitor was also placed on the mode to measure resonance decay over time, which was used to determine the Q factors of the resonances. After an initial simulation was performed and its spectrum was analyzed, field profile monitors were defined to encapsulate the entire resonator and set to render a spatially

resolved image of $|\mathbf{E}|^2$ at the resonant wavelengths. The simulation was then run another time to obtain the electric field profile images. To measure the evanescent wave penetration from the profiles, Imagej was used. A vector that quantified the field intensity with position was placed along the radial direction of the resonator through the boundary. The evanescent wave depth was quantified when the peak intensity of the evanescent wave reduced to 1/e of its initial value. The profiles were also used to quantify the AMN and radial mode order.

2.3 Results and Discussion

The FDTD simulations were analyzed to first confirm the presence of WGMs and then to quantify the WGM resonance by measuring the FSRs, n_{eff}, and Q factors and the evanescent wave penetration. These properties were analyzed as a function of the resonator diameter. One important objective of the simulations was to determine what minimum size of resonator would be able to adequately sustain WGM resonance for PVA in both air and in water. This required obtaining a high Q factor and preventing any mode overlap that would make peak distinction and analysis difficult for future sensing experiments. Furthermore, if the evanescent wave penetrates too far outside the resonator, optical coupling with the fiber substrate may take place that will reduce the cavity's resonance capability. As such, investigation of the field profiles was performed to determine the evanescent wave penetration.

2.3.1 WGM Confirmation in Simulations for the PVA in Air System

A complete analysis of an individual spectrum between 550 nm and 580 nm for a 5 μm diameter resonator is shown in Figure 2.2a. In addition to being accompanied by its electric field profile, each mode is labeled with its peak wavelength, mode order, and AMN. The red "petal" shapes on the field profiles represent electric field maxima and minima, indicating that two consecutive extrema represent a single wavelength of light. The field profiles indicate that the modes at 556 nm and 570 nm are first order radial modes. By halving the number of the red extrema in the profiles, the modes are found to have AMN values of 38 and 37, respectively. Two second order radial modes also appear around 562 nm and 576 nm with AMN values of 33 and 32, respectively. The smaller AMN values are expected for the higher order modes, due to a shorter path length. Because the field profile images reveal a pattern of intense electric field circumnavigating the inside periphery of the cross-sections, which is characteristic of WGM resonances, these modes can be confirmed as WGMs[68,69].

2.3.2 Analysis of Spectra for the PVA-Air System

Resonator diameters were varied between 2 and 7 μm in 1 μm increments. The simulation failed to produce WGMs at diameters below 2 μm indicating that WGMs were not supported, therefore, the fibers fabricated later would need to have diameters larger than this. Figure 2.2b shows the spectra for 2 μm, 4 μm, 5 μm, and 7 μm diameters. The spectrum for the 2 μm cross-section shows just two broad, widely-spaced peaks. In general, as diameters increased, the spectra of the resonators displayed sharper peaks,

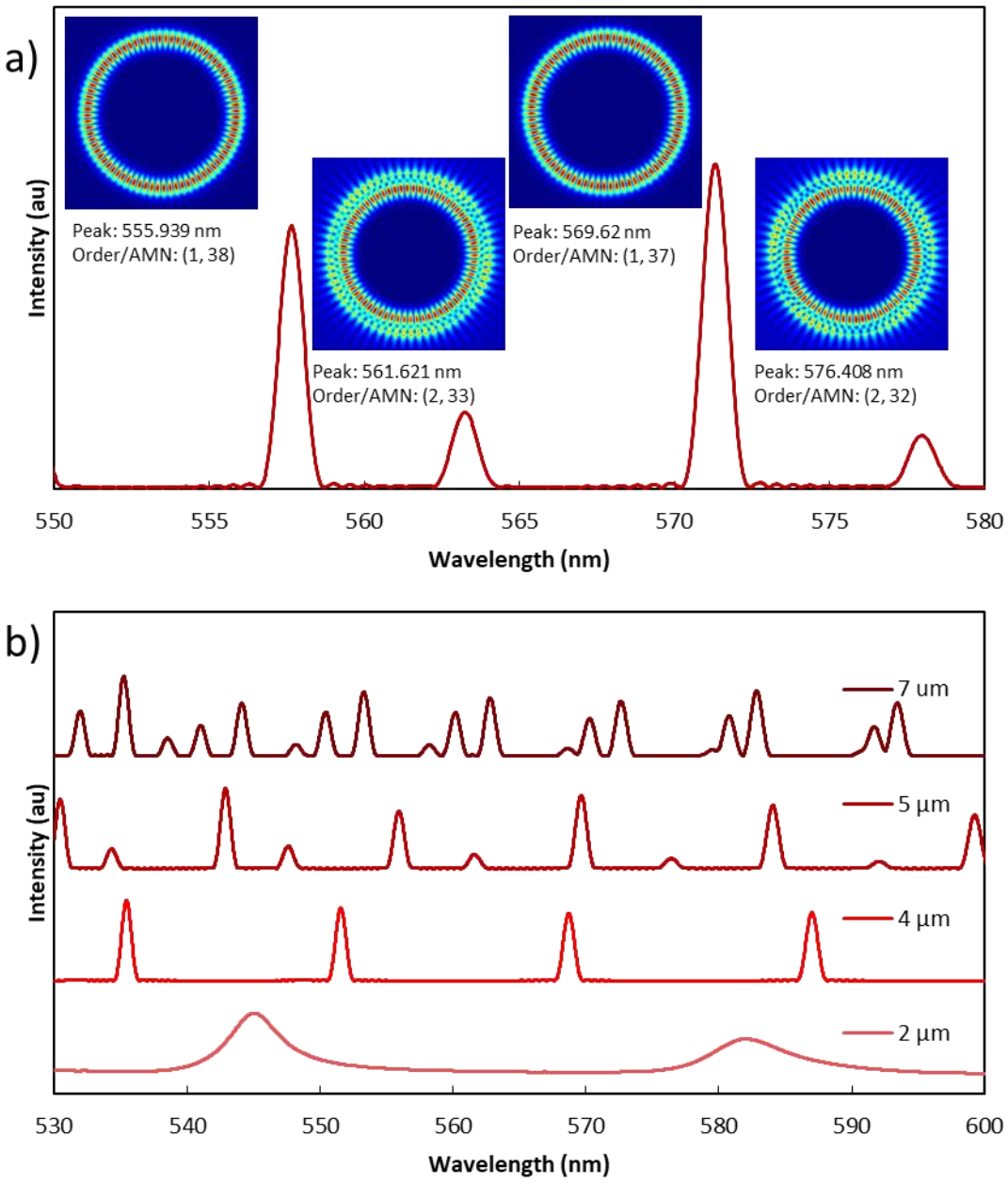

Figure 2.2: a) Portion of spectra of a 5 µm diameter resonator with first and second order modes present. Electric field profiles are next to their respective peaks with wavelength, radial order, and AMN indicated. b) Spectra of resonators with increasing diameters.

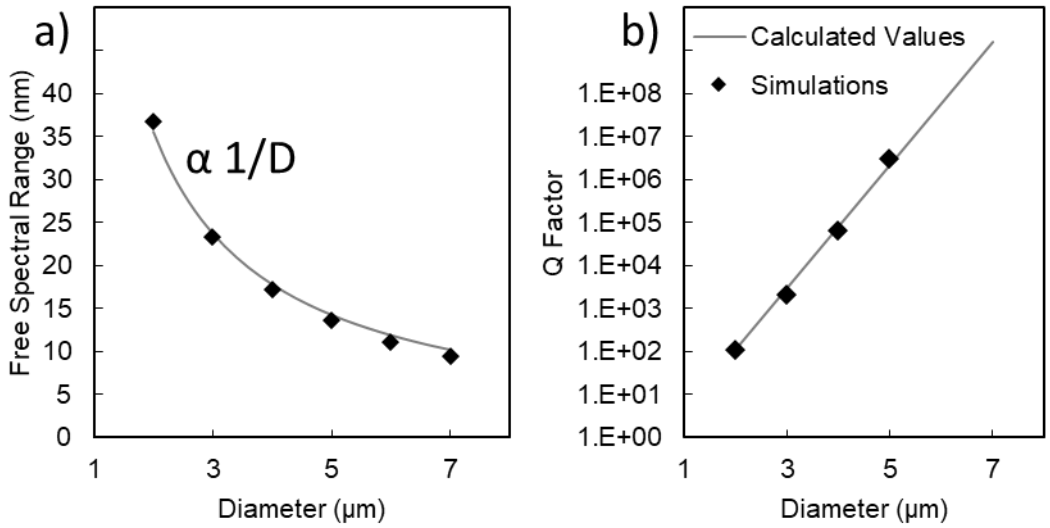

Figure 2.3 a) FSR as a function of diameter for the PVA-air system and b) Q factor as a function of diameter.

indicative of higher Q factors as well as more frequent peaks, indicative of lower FSRs, which is characteristic of WGMs. A notable observation in the 5 μm and 7 μm resonators is the emergence of a second group of lower-intensity peaks. The higher intensity peaks are first order resonances while the lower intensity peaks are second order resonances. Furthermore, the 7 μm spectrum shows the emergence of third order peaks next to even more numerous first and second order peaks. Above 570 nm, the higher order modes began to merge with the lower order modes, indicating that the two modes were occupying the same wavelength. This mode overlap made field profile and Q factor analysis challenging, as discussed later.

The FSR of consecutive, first order radial resonances is plotted with the black data set in Figure 2.3a. The values decrease from 37 nm to 9.5 nm in a 1/diameter trend, as predicted by the equation:

$$FSR = \frac{\lambda^2}{Ln_{eff}} \quad (3)$$

where L is the resonator path length. For WGMs, the cavity circumference, 2πD, is nominally the path length (L). From this equation, an approximate optical path length and diameter can be deduced from the FSR, which will serve as a method to confirm WGM resonance in the fabricated devices.

Q factor is known to be limited by three parameters[70,71]: radiative decay, material absorption, and surface roughness. These parameters combine to contribute to Q as such:

$$Q^{-1} = Q_{rad}^{-1} + Q_{Abs}^{-1} + Q_{Surf}^{-1} \quad (4)$$

Typically, resonators are limited by surface roughness or material absorption, but since neither of these were accounted for in the simulations, the Qs here were limited by radiative decay. This contribution, as determined by Slusher et. al.[72] is:

$$Q_{rad}^{-1} = \frac{1}{7} e^{2\frac{2\pi R n_{eff}}{\lambda}\left[\tanh^{-1}\left(\sqrt{1-1/n_{eff}^2}\right) - \sqrt{1-1/n_{eff}^2}\right]} \quad (5)$$

which predicts that Q factor will increase exponentially with an increase in diameter. Figure 2.3b confirms this by showing a log-linear plot of the Q factor for the peak nearest 558 nm (to match the R6G dye) as a function of diameter as well. The simulated Qs increases exponentially between 2 μm and 5 μm, from ~$1x10^2$ to ~$3x10^6$, respectively. The value calculated from Equation 5 is plotted as a line as well. Up until 5 μm, the values are nearly coinciding, indicating that the equation is accurate. However, the values diverge for resonators larger than 5 μm, which is believed to be a result of the convoluted modes that appear in the larger diameter resonators. Regardless, experimentally obtained WGM resonance is typically limited by either surface scattering or material absorption, so these simulations show the device theoretical Q factors.

To further examine the resonant modes, figures 2.4a-f show electric field profiles for each resonator diameter, again of the wavelength nearest 558nm. The petal-shaped extrema go around the inside of the cross-section while the much smaller extrema on the outside of the cross-section represent the evanescent wave extending into the environment. With the increase in size, a few phenomenon are observed. First, the evanescent wave penetration is much greater in the lower diameter resonators and second, the larger diameter field profiles show a significant amount of convolution with higher order radial modes.

Figure 2.4g shows a plot of the evanescent wave penetration depth with increasing diameter. At a 2 μm resonator, the depth was greater than the boundaries of the field profile monitor so its value could not be quantified. However, when the diameter increases, the penetration decreases from 430 nm at 3 μm 210 nm at 5 μm. Evanescent

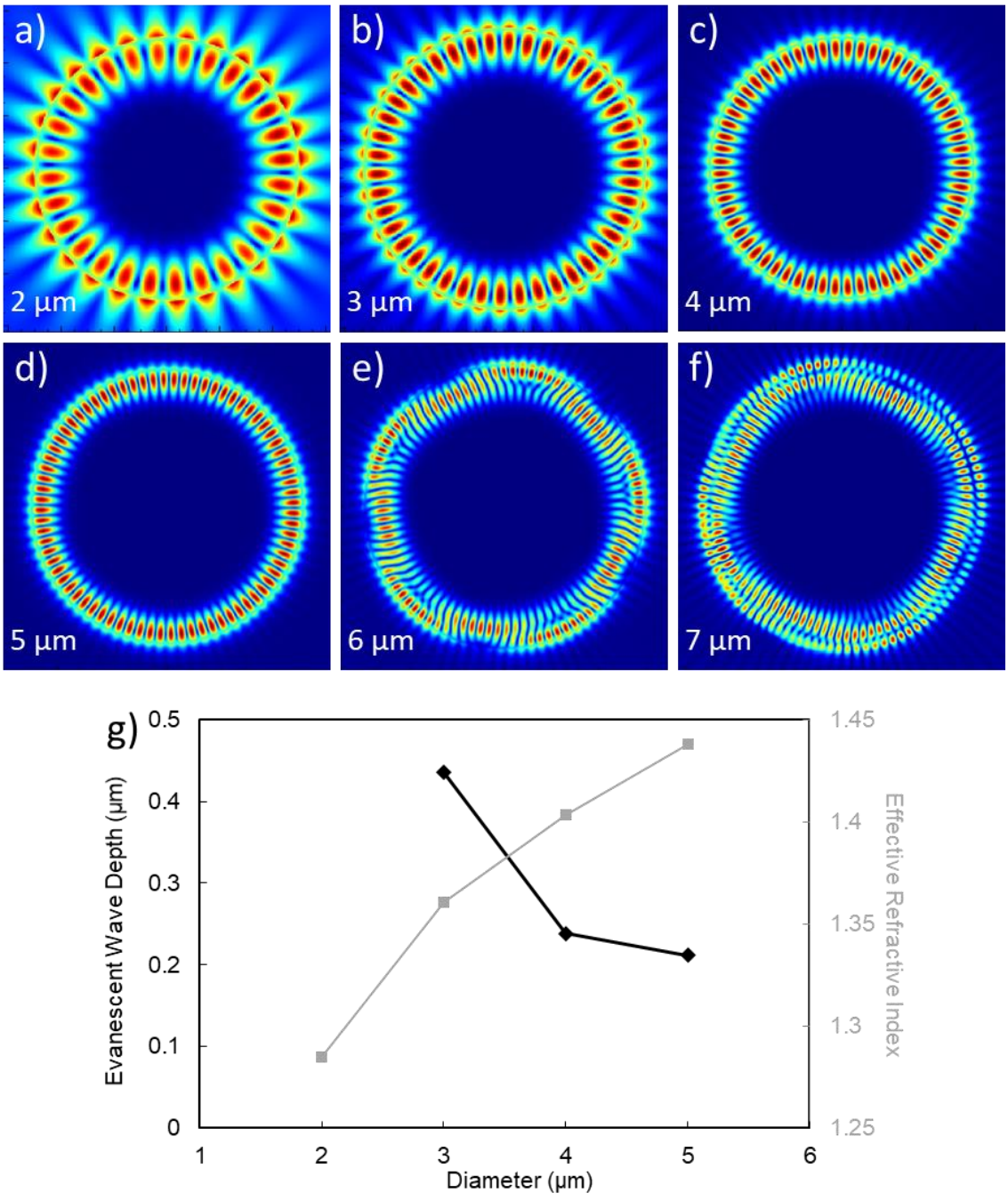

Figure 2.4: a)-f) Electric field profiles of the resonators at increasing diameters and g) plot showing evanescent wave depth and n_{eff} with increasing resonator diameters.

field penetration measurements could not be accurately performed at 6 μm and 7 μm diameters due to the mode convolution with higher radial order modes, as the higher order modes have larger evanescent waves. Since the highest measured evanescent wave penetration is around 430 nm, the fabricated fibers should be suspended at least this distance to prevent any evanescent wave coupling to the substrate. Briefly, Figure 2.4g also shows that the n_{eff} (calculated from Equation 3) increases with diameter from 1.28 at 2 μm to around 1.44 at 5 μm. This trend of smaller resonators having a lower n_{eff} is expected, since n_{eff} is a weighted average of the field inside and outside the resonator and the smaller resonators have a larger evanescent wave. This analysis gives a range of values that can be useful when performing mode fitting analysis for the devices.

2.3.3 Spectral Analysis for the PVA in Water System

As mentioned in the experimental details, the only adjustments done for the water system simulations was a change in the environmental RI to match water and change in the range of diameters analyzed. Similar to how the air simulations showed no resonance below 2 μm, the water simulations showed no resonance for diameters below 6 μm, indicating that aqueous devices should be at least this size. The reason for the required increase in size is the smaller refractive index mismatch between resonator and environment. Figure 2.5a shows incremental spectra between 6 μm and 10 μm diameters. At 6 μm, low intensity, broad peaks are observed and as D increases, the peaks become sharper and more closely spaced. One interesting characteristic of the water system is that

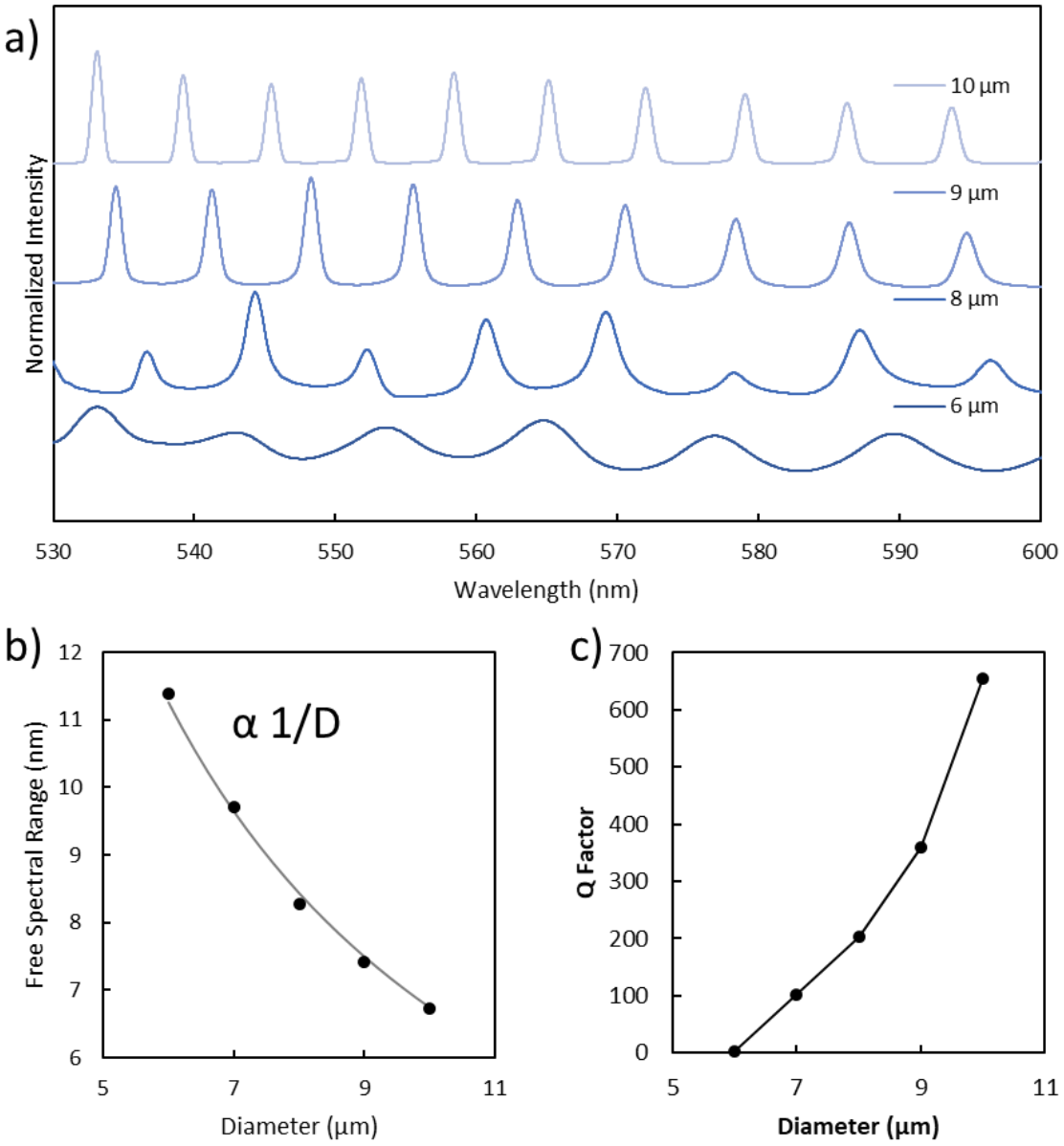

Figure 2.5: a) Spectra of resonators at increasing diameters for the in-aqueous system. b) FSR as a function of increasing diameter and c) Q factor as a function of increasing diameter.

even at 10 μm, there was no emergence of higher order modes, indicating that this system does not support resonance as well as the air system, which is also due to the closer RI between resonator and environment. The same quantitative analysis on FSR and Q that was done in air was applied to the water system. As shown in Figure 2.5b, the FSR values are still proportional to 1/diameter but are much lower in this system due to the large increase in fiber diameter and the increase in n_{eff}. Once again, this gives an indication for FSR values that can be expected for the fabricated devices. Furthermore, the values for Q are shown in Figure 2.5c. While Q still increases exponentially with diameter, it does so less rapidly. The values range from ~3 at 6 μm up to just 650 at 10 μm. This information indicates that viable resonators for sensing applications will need to be significantly larger for the aqueous system than they are for the air system.

The field profiles are shown in figure 2.6a-e. The field profile for the 6 μm resonator has poor optical confinement, as the only regions that display an intense field are near the location of the emission sources. As the diameter increases the resonance becomes much more contained. No mode convolution from higher order modes is observed, even as diameter increases to 10 μm. The resonators here have visibly larger evanescent waves, however, the appropriate quantification of their depth could not be done because the profile monitor did not extend far enough away from the resonator boundary in all cases except 10 μm, discussed in the next paragraph. Despite the resonators having a visibly larger evanescent wave than the in-air resonators, values for n_{eff} range between 1.41-1.44. These values are larger than the air system because of the higher RI of the environment.

Finally, Figure 2.7a quantifies evanescent wave penetration as a function of resonance wavelength for the 10 µm resonator. As the peak wavelength increases, the evanescent wave extends further into the environment to values as high as 1,400 nm. For resonators this size, they should be greater than 1,400 nm from the substrate when measured in water. Figure 2.7b-d shows field profiles of three modes in this system. Again, as the wavelength gets longer, the evanescent wave can be seen penetrating further into the environment as the regions further away from the resonator get lighter in shade. For bulk RI sensing purposes, this indicates that the longer wavelength peaks will

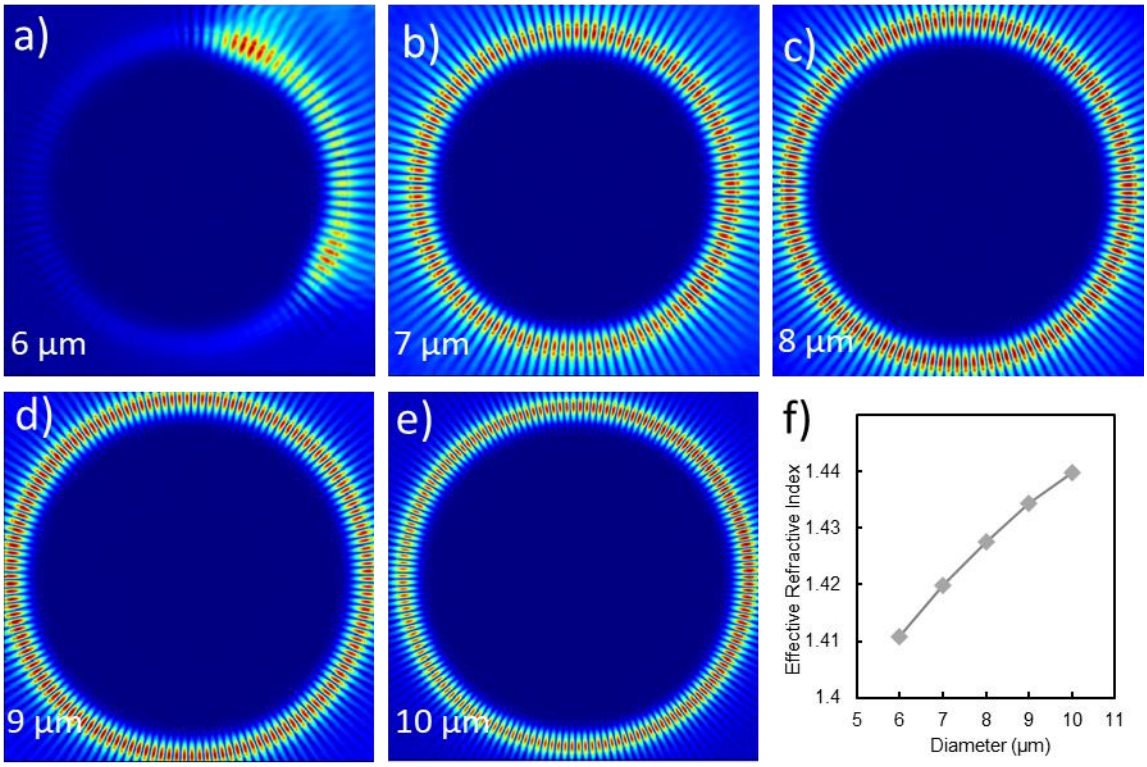

Figure 2.6: a)-e) Electric field profiles of the resonators at increasing diameters for in-aqueous system and f) plot showing the change in n_{eff} with increasing diameter.

be more sensitive because the change in n_{eff} will be more drastic with a larger evanescent wave, however, Figure 2.7a also plots mode Q factor as a function of wavelength. It can be seen steadily decreasing with increasing wavelength. While these longer wavelength modes may be more sensitive to RI change, a low-Q system may be more difficult to detect a wavelength shift. For sensing experiments, the longest viable wavelength should produce the greatest sensitivity.

2.4 Conclusions

In conclusion, FDTD simulations gave valuable insight to our electrospun-fiber WGM system in both air and aqueous environments. For air, resonance was not supported below 2 μm and for aqueous it was not supported below 6 μm. This indicated that our fibers needed to be at least this size for their respective environments. FSR values decreased with increasing diameter and were much smaller for the aqueous system due to the larger size and higher n_{eff}. Resonance Q factors improved with increasing diameters. The Q factors were much higher for the air systems, due to the higher RI mismatch between resonator and environment. Higher order modes were observed in the air systems and subsequent mode convolution that made mode discrimination more difficult. Field profile analysis showed that the evanescent wave penetrated around 430 nm into the environment for the air system and around 1,400 nm for the aqueous system, indicating the devices should be at least that far from the substrates to prevent optical coupling in their respective systems. Lastly, evanescent penetration increased in the longer wavelength modes, indicating that these modes will be more sensitive, however,

this comes at the cost of a reduced Q factor, which may make sensing more difficult in this wavelength region.

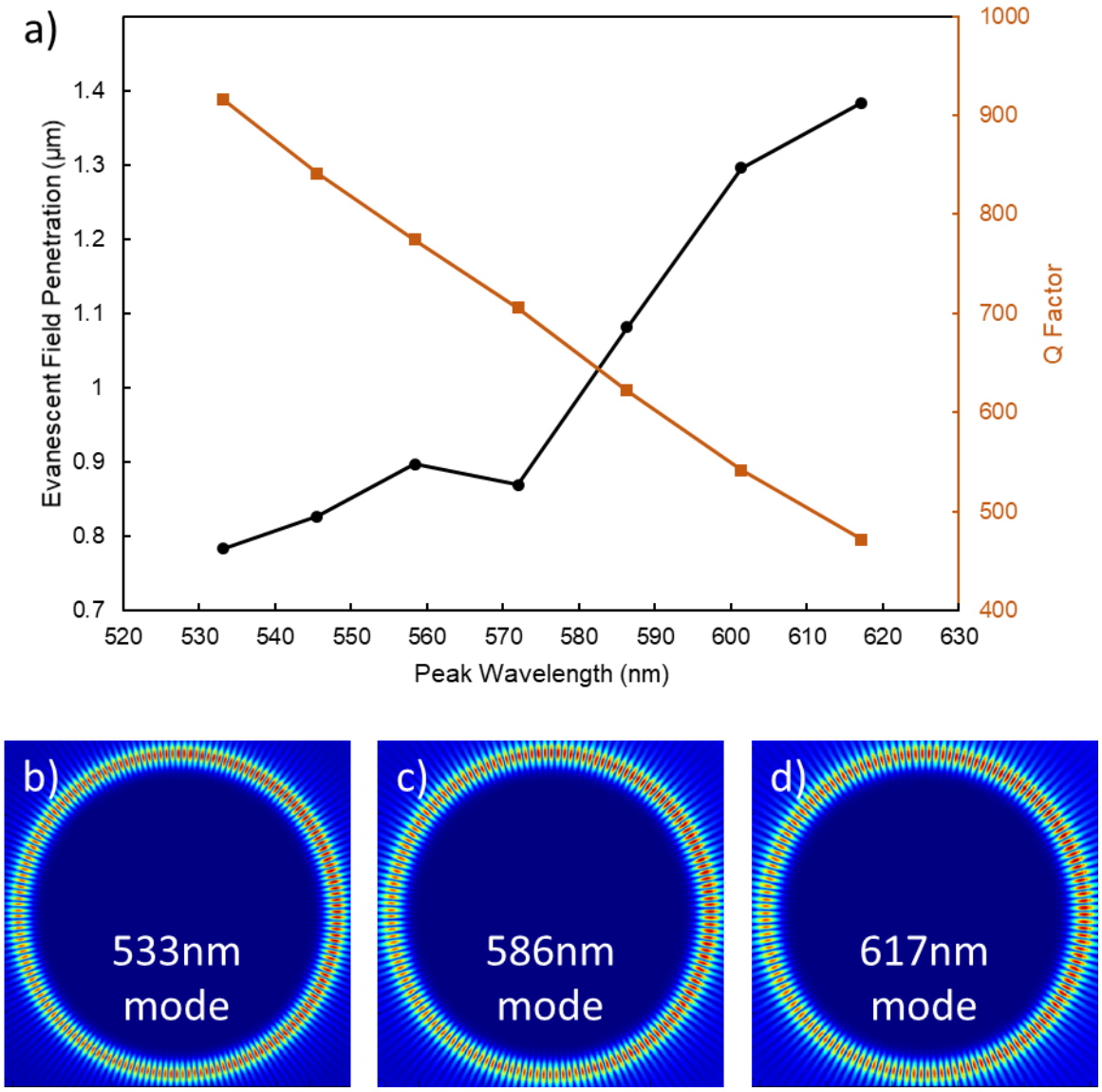

Figure 2.7: a) Evanescent wave penetration and Q factors for different modes at increasing wavelengths for the 10 μm in-aqueous system and b)-e) field profiles at increasing mode wavelengths.

3 Physicochemical and Optical Characterization of PVA and R6G-PVA Solutions

3.1 Introduction

Because they dictate the electrospun fiber morphology, a few important physicochemical properties of the PVA solution were characterized. Specifically, viscosity, surface tension, and conductivity measurements of newly mixed PVA and R6G-PVA solutions were performed to evaluate the robustness of the mixing process and evaluate baseline solution parameters. Viscosity, often referred to as a solution's "thickness", quantifies the resistance to shear stress of a solution. A higher viscosity indicates more shear resistance and that increased shear resistance leads to a larger fiber diameter[59,73,74]. Often, electrospinning is used to fabricate small, sub-micron fibers, but since this work required large fibers, a relatively high viscosity will be required. Surface tension describes the amount of attraction of surface molecules to the rest of the solution. If a solution has a too high of a surface tension, electrospinning may not initiate or the electrospinning jet may be unstable[59]. Lastly, conductivity quantifies a material's ability

to conduct electricity. An increased conductivity leads to smaller fiber diameters, so, ideally, a lower conductivity would be obtained. The solutions were also spin coated into thin films for optical characterization i.e. absorption, emission, and RI measurements to determine what concentration of R6G dye would be sufficient for later WGM experiments.

3.2 Experimental Details

PVA powder (Sigma Aldrich, molecular weight 13,000 – 23,000 g/mol, 98% hydrolyzed,) was measured and placed in a 20 mL glass vial (27 mm x 59 mm diameter and length outer measurements) as shown in Figure 3.1a). For pure PVA solutions, Millipore water was added to the PVA to make a 25 wt% solution. For solutions containing dye, R6G powder was added to the PVA before adding the Millipore water, Figure 3.1b and 3.1c. Solutions were mixed for two hours in a hot water bath set at 80^{O}C with a magnetic stir bar set to 800 RPM, figure 3.1d. The solution was placed in ambient conditions to cool for one hour with no further mixing before physicochemical characterization. To measure and minimize any solution inconsistencies, viscosity (Brookfield LV DV-I/ Prime Viscometer), surface tension (DuNuoy ring surface tensiometer), and conductivity (Lab Quest 2 conductivity probe) measurements were performed immediately following cooling.

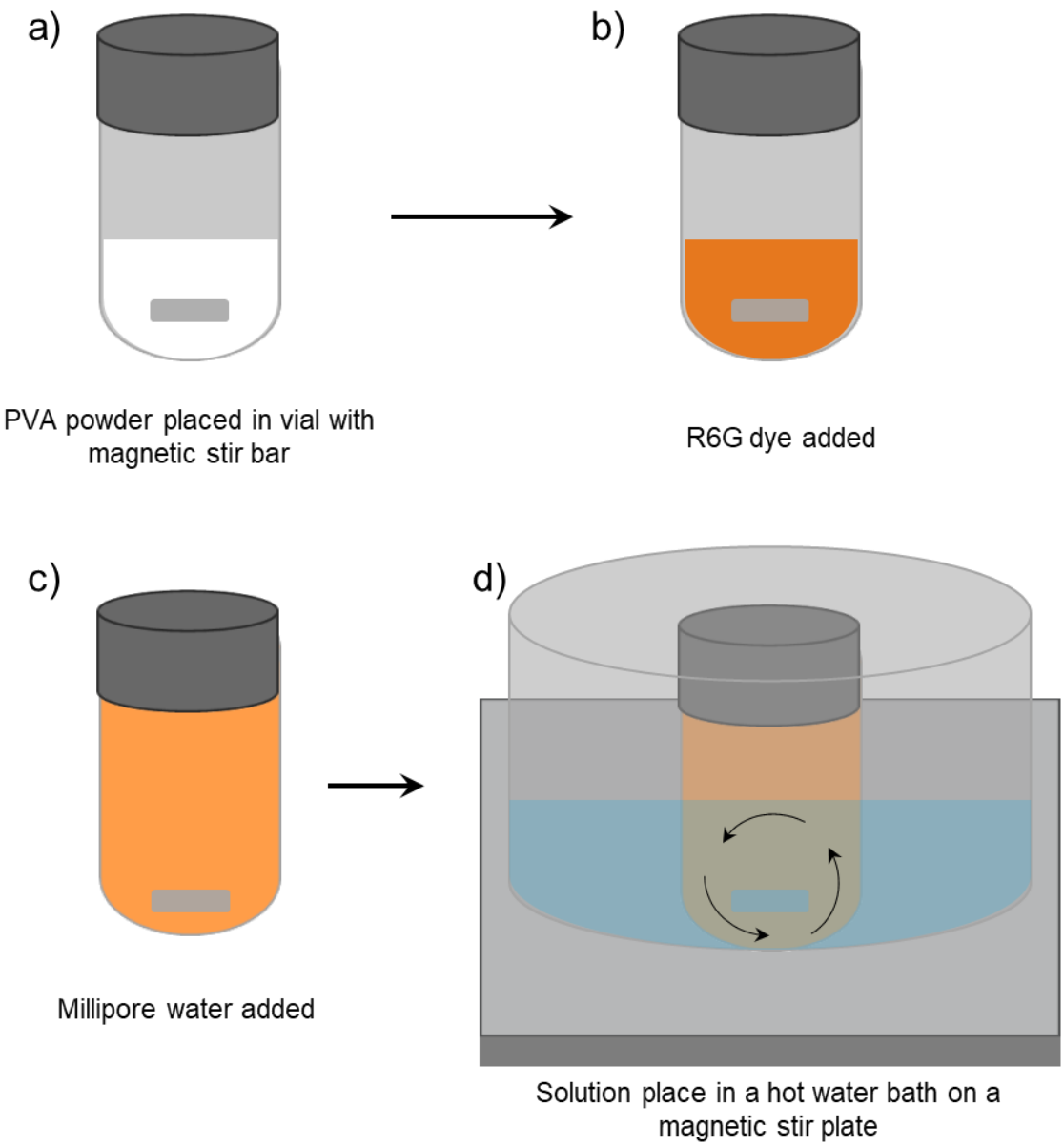

Figure 3.1: Schematic of solution mixing process. a) PVA and magnetic stir bar placed in vial, b) R6G added, c) Millipore water added, and d) solution mixed in a water bath on a hot plate.

To measure the optical properties of the PVA-R6G, the solutions were spin coated onto 25 x 75 x 1 mm glass microscope slides to produce thin films. Having thin films allowed the water to be evaporated, creating a material with identical composition to the electrospun fibers. The slides were fixed on a vacuum seal and solution was deposited on top of them. The spin coater was ramped up to 500 RPM at 100 RPM/s, then it was ramped up to 3000 RPM at 600 RPM/s where it was left for 20 seconds. Finally, the spin coater was decelerated back to 0 RPM at 600 RPM/s. Following spin coating, the slides were placed on a hot plate for 5 minutes at 50^{o}C. The thicknesses of the thin films were measured using a surface profilometer (Dektak). Absorption measurements of the thin films were made using a spectrophotometer (Varian Cary 500). The scans were from 300 – 750 nm at 1 nm increments with a 0.1 second integration time. Fluorescence measurements were performed (six months after spin coating the solution) using fluorometer (Horiba QM 400) from 540-700 nm at 532 nm excitation with 0.5 nm entrance slits, at a 45^{o} angle, 0.5 nm exit slits, 0.5 nm increments, and 0.1 second integration time. Lastly, RI measurements were made on the thin films (also six months after the spin coating was done) using an ellipsometer (UVISEL Spectroscopic Phase Modulated) from 400-800 at an angle of incidence of 70 degrees, an integration time of 250 milliseconds and with 5 nm increments.

3.3 Results and Discussion

3.3.1 Physicochemical Characterization of PVA Solutions

Table 1 shows physicochemical measurements of a representative selection of the solutions that were mixed. The pure PVA solutions had average viscosity, surface tension, and conductivity measurements of 689.65 ± 82.4 cP, 56.75 ± 1.9 dynes/cm, and 2671 ± 108.8 μS/cm, respectively. The standard deviations for both surface tension and conductivity were less than 5%, which was easily acceptable for our purposes. The standard deviation for the viscosity measurements was larger, at 12%. The reason for the larger standard deviation is that the PVA, being a relatively low molecular weight, expedites a gelation effect of the polymer solutions by facilitating the hydrogen bonding process between the polymer chains, more-rapidly increasing the viscosity[75,76] than what may be expected in a solution with a higher molecular weight PVA. This makes the viscosity measurements less consistent among solutions. Nonetheless, this deviation in

Table 1: Physicochemical properties of R6G-PVA solutions at different dye concentrations.

R6G Concentration (mgR6G/gPVA)	Viscosity (cP)	Conductivity (μS/cm)	Surface Tension (dynes/cm)	N
Pure PVA	689.7 ± 82.4	2671 ± 109	57 ± 2	4
0.9	884.4 ± 17.1	2521 ± 45	55 ± 0	2
1.8	753.3	2554	53	1
3.5	717.5 ± 74	2726 ± 102	56 ± 1	3

viscosity measurements is still relatively small. Furthermore, the hydrogen bonds can be broken with mechanical agitation[75], which would happen to some degree during the electrospinning when the solution is pumped through a syringe and needle. Therefore, the discrepancy was not anticipated to have a detrimental effect in electrospinning the solutions, though it was investigated and will be discussed in the next chapter.

The R6G-PVA solutions were made at a few different R6G concentrations as shown in Table 1. The R6G concentrations analyzed were 0.9, 1.8, and 3.5 mgR6G/gPVA, which were selected based around a report by Ta et. al.[17] Since all three concentrations were low compared to the amount of PVA used, the dye incorporation was not expected to have any significant impact on the physicochemical measurements.

Comparing the physicochemical values across the different dye concentrations and pure PVA solutions reveals that physicochemical values remained relatively unaffected by R6G incorporation. Similar to the pure PVA solutions, the standard deviation for each of the R6G-PVA solutions values for surface tension and conductivity was less than 4%, indicating a robust process. However, the solution's again showed viscosities with higher standard deviations, though not higher than in the pure PVA case. The larger standard deviation was attributed to the same reason for the pure solution. This confirms that the R6G does not significantly contribute to the solutions physicochemical properties and will not have a noticeable impact on electrospinning. Furthermore, the robustness of the solution mixing process is verified.

3.3.2 Optical Characterization of Mixed PVA and R6G-PVA Solutions

To determine which dye concentration be sufficient to support WGM resonances, the pure PVA solution and R6G-doped solutions were spin coated onto glass slides to produce thin films which were subsequently optically characterized for their absorption coefficient, fluorescence, and RI. The objective was to obtain a solution with a large absorption that also maintained a low amount of absorption for a large portion of the emission range and to avoid any fluorescence quenching that may occur at higher R6G concentrations. To analyze a wide range of R6G concentrations, the selected values were 0.5, 0.9, 1.8, and 3.5 mgR6G/gPVA.

To determine peak excitation wavelength, absorption measurements of the films were performed and the spectra were converted to absorption coefficient by dividing by the thin film thickness. The thicknesses of the films are 4.538, 4.562, 4.750, and 5.039 μm for 0.5, 0.9, 1.8, and 3.5 mgR6G/gPVA, respectively. The spectra are shown in Figure 3.2a. Three peaks are observed. A shorter peak at 350 nm, a shoulder near 500 nm, and the maximum R6G absorption peak at 537 nm. Since the pure PVA film shows no absorption from 300 nm – 750 nm, all peaks were characteristic of the R6G. As expected, the film with the highest R6G concentration also showed the highest amount of absorption. The highest peak was at 537 nm for every dye doped film. This is further shown in Figure 3.2b which shows the absorption coefficient as a function of R6G concentration at three specified wavelengths: peak absorption, peak emission, and zero emission. The absorption coefficient at peak

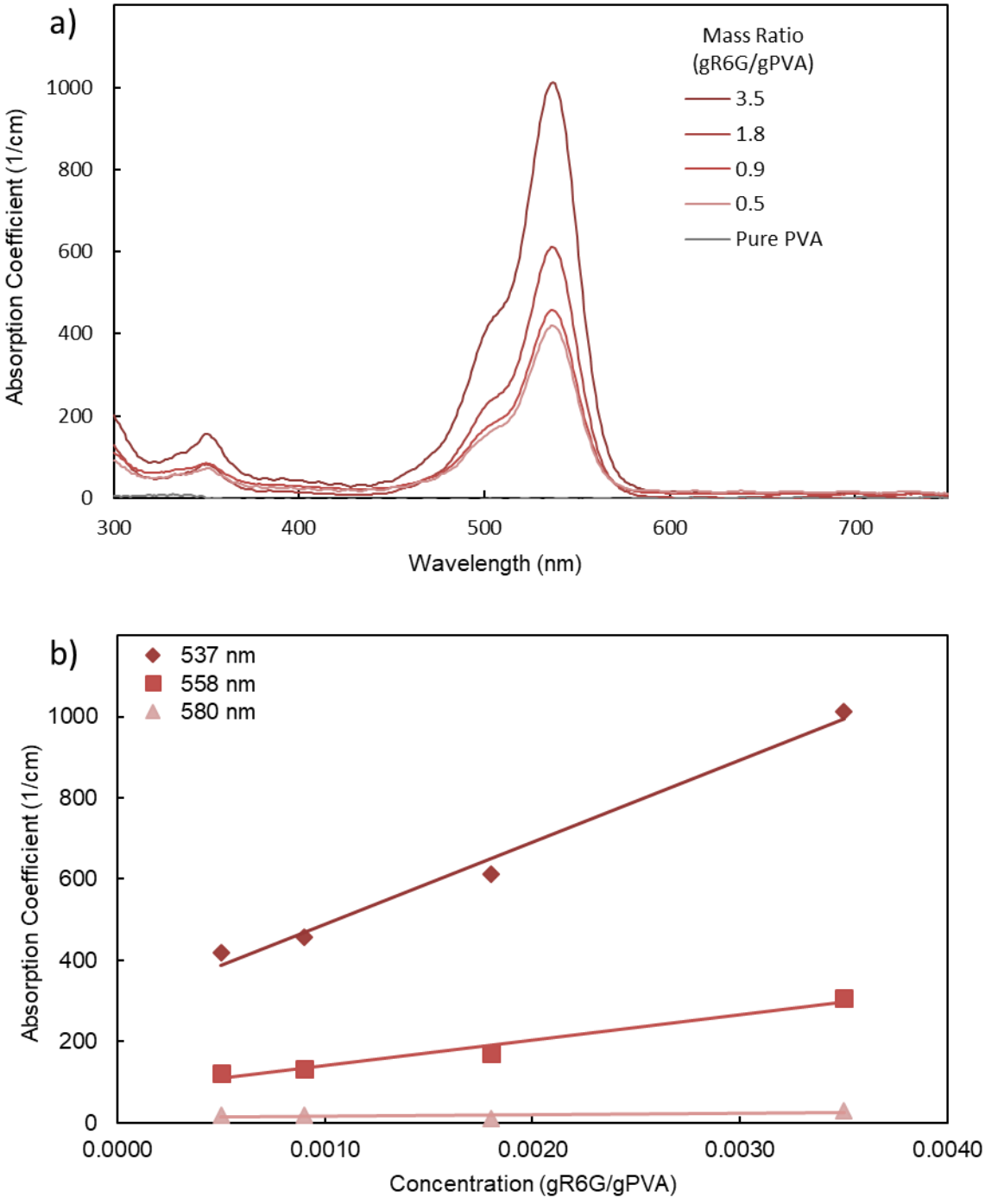

Figure 3.2: a) Absorption coefficient spectra of R6G-PVA thin films, b) absorption coefficient vs R6G concentration at selected wavelengths.

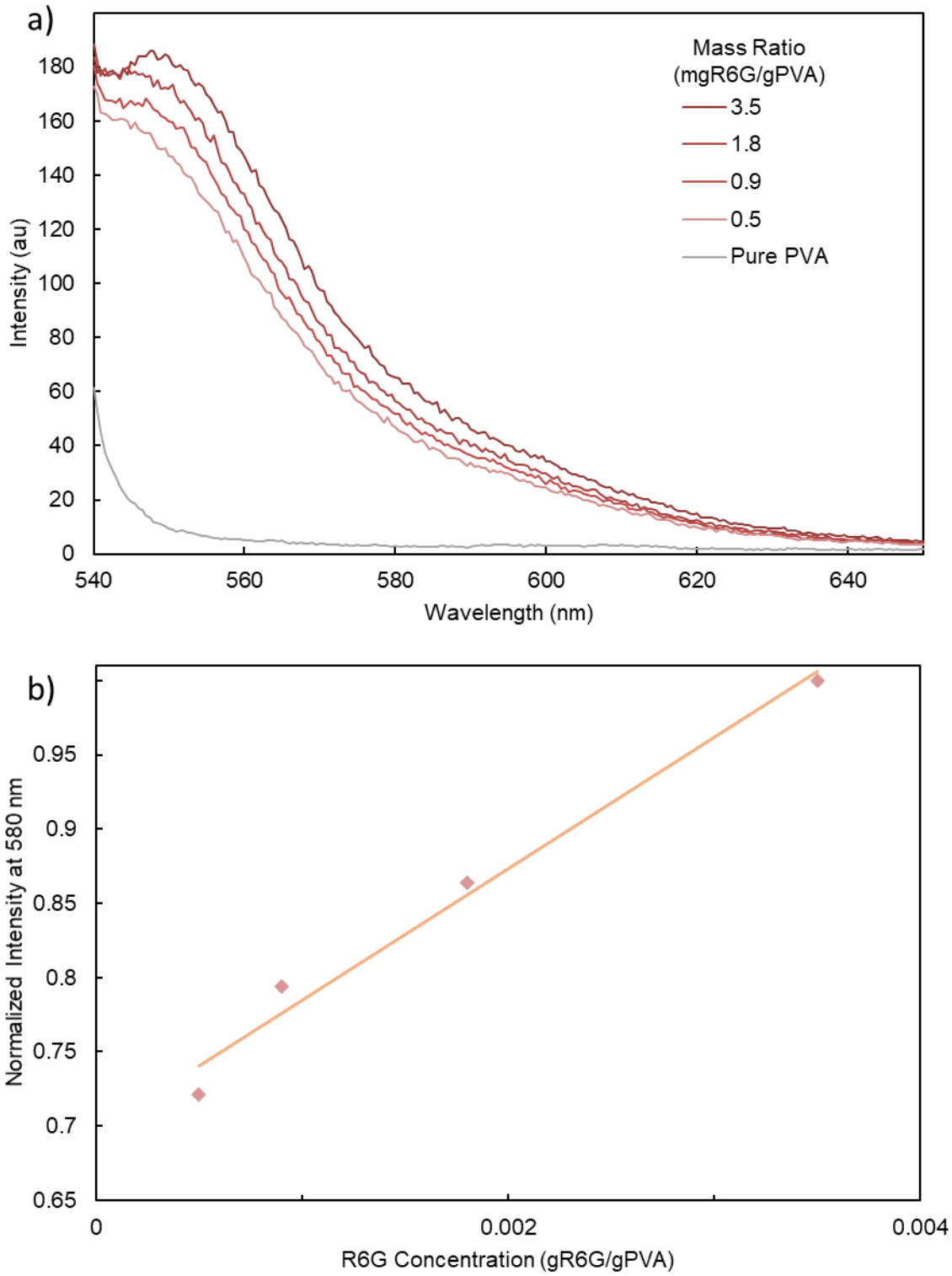

Figure 3.3: a) emission spectra of thin films and b) normalized intensity vs R6G concentration at 580 nm.

absorption shows a linear increase with concentration. The known peak emission wavelength of 558 nm showed the same linear trend. Furthermore, there is still substantial absorption here, indicating that resonance will be stifled, despite having the most fluorescence. Finally, the absorption coefficient is almost zero at all concentrations for the 580 nm data point (and longer). Because of this, the highest Q factor resonance is expected to be observed longer than 580 nm, regardless of R6G concentration.

The next step was to determine the concentration of dye to use that would give an adequate intensity emission signal, so photoluminescence measurements of each of the thin films were taken. The emission spectra are shown in Figure 3.3a. The pure PVA sample showed no PL emission, indicating that all emission was coming from R6G. Across all samples, a slight increase in PL is seen near 540 nm. This increase is simply the tail end of the excitation source and is not significant in the PL analysis. The peak emission intensity was shown to increase with increasing R6G concentration and peak PL signal was around 550 nm at the lowest concentration. As the concentration increased to 3.5 mgR6G/gPVA, a red shift of ~5 nm was observed. This shift is believed to be caused by photon reabsorption due to the dye molecule's close proximity to each other. Because there is no absorption in wavelengths above 580 nm, the PL intensities in the region of 580 nm and longer were examined further. The emissions intensities increase linearly with dye concentration as shown in Figure 3.3b. Since the highest concentration gave the highest PL intensity, it was determined that to produce the highest intensity WGM resonance, using the 3.5 mgR6G/gPVA concentration would give ample emission in our electrospun fibers.

Because the ability for the devices to support resonance strongly depends on RI, measurements were performed on the thin films. If there were any major differences depending on R6G concentration, the ability for the device to sustain resonance will also be affected; if RI is increased, the ability of the device to resonate will be improved. The RI data is plotted as a function of wavelength in Figure 3.4a. The data shows that despite the increasing concentration of R6G dye, the spectra all remain relatively constant from 580 – 700 nm. The value for RI is slightly lower than reported in the literature[51]. Furthermore, the average values between 580-700 nm for all concentrations are shown in Figure 3.4b. At 3.5 mgR6G/gPVA, the RI is 1.4642 ± 0.0059. Furthermore, the values all lie very close to one another, indicating that the RI remains consistent through the emission wavelengths. For this reason, we know the RI at different R6G concentrations

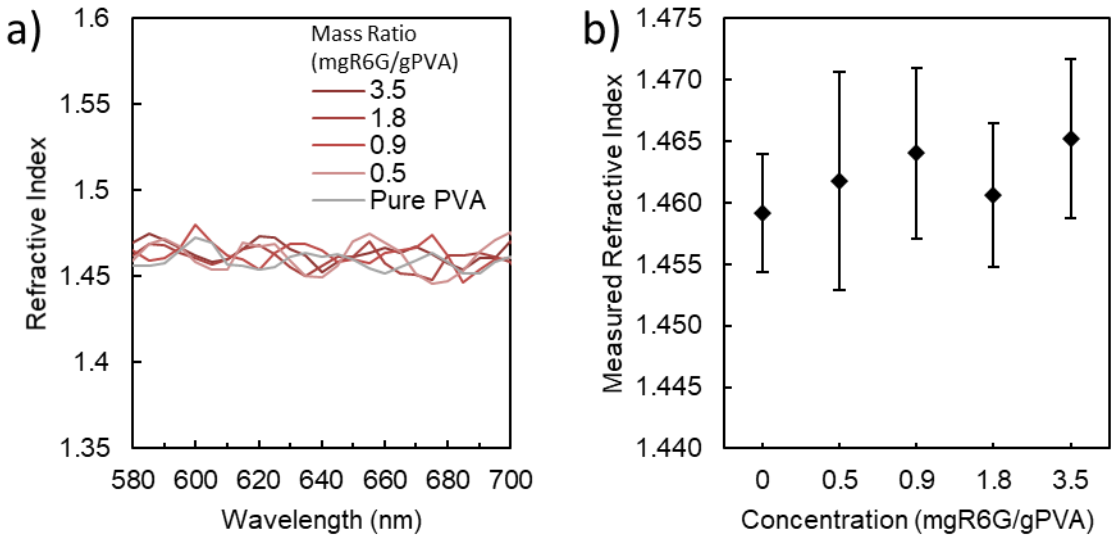

Figure 3.4: a) Refractive index vs wavelength for R6G-PVA films and b) average RI between 580 – 700 nm for thin films at their respective concentrations.

would not have a significant role in affecting resonance. Lastly, since the value for RI was set higher for the FDTD simulations, this indicates that the values found for FSR, and n_{eff} may be slightly different than what was experimentally measured later.

3.4 Conclusions

The main contributors to the physiological properties of the solutions measured here is their combination of molecular weight and wt%[59,74,77]. This work used a much lower molecular weight and much higher wt% than other NFES reports[65,67,78–81]. The combination of high wt% and low molecular weight was used because it contributed to a higher solution viscosity. Consequently, it should also contribute to a higher diameter and more uniform fiber when electrospun[73]. The higher wt% also led to a small decrease in surface tension (which is ordinarily dictated by choice in solvent) and an increase in conductivity. While the physicochemical properties are known to play a vital role in other morphological features of electrospun fibers such as the formation of beads[82,83] and pores[84], these were not taken into consideration for this work. Because the values for conductivity, and surface tension remained consistent across all solutions and the slightly higher deviation in viscosity can be accounted for, the process to consistently mix the 25 wt%, 13,000-23,000 g/mol was demonstrated. Furthermore, because the addition of R6G did not significantly alter the physicochemical properties, having R6G in the solution was not expected to have any significant effect on the electrospinning.

After performing optical characterization on spin coated thin films of our R6G PVA solutions. It was determined that increasing dye concentration increases material absorption, though all absorption stops after around 580 nm and is not therefore expected to affect WGM resonance longer than those wavelengths. According to the emission spectra, the intensity increases linearly with concentration above 580 nm as well. Because of this, the highest analyzed concentration of 3.5 mgR6G/gPVA was further investigated for electrospinning WGM resonators. Lastly, ellipsometry measurements showed that the addition of dye does not affect the RI and thus should not have any bearing on WGM resonance, though, the measured values will likely be slightly different than the simulations.

Chapter 4. Fiber Fabrication and Morphological Characterization

4.1 Introduction

To fabricate polymer fibers with diameters large enough to support WGM resonance for in-air and in-aqueous as determined from the FDTD simulations, NFES was used to fabricate fibers initially on SiO_2/Si substrates. Electrospinning parameters such as tip-to-collector distance, voltage, and stage speed can be altered to produce the desired fiber morphologies. Here, the fiber diameters were characterized by varying the applied voltage, stage speed, age of the solution, and R6G incorporation. Later, the substrate was changed to glass (a transparent substrate was necessary for subsequent fluorescence imaging because excitation and collection happened on opposite sides of the sample). The effect of this change in substrate on fiber diameter was analyzed across a range of stage speeds. As revealed in chapter 2, the resonators needed to be a few hundred nanometers from the substrate to prevent unwanted optical coupling. Scribe marks of an appropriate width and depth on the substrates provided trenches to allow the electrospun fibers to be suspended. Further morphological characterization needed to be performed to analyze fiber surface roughness and circularity, which are important for

supporting resonance. For this, scanning electron microscopy (SEM) was used. Other morphological feature such as the amount of taper along fiber length was also quantified as it may influence resonance elements along the z-axis; this would not have been discovered in the 2D FDTD simulations. One benefit to using the PVA system was that the polymer is water soluble, however, later applications required sensing in water. Because of this, the fibers were crosslinked to make them water insoluble for aqueous sensing experiments. The crosslinked fibers were characterized for their water stability, the effect of crosslinking on fiber diameter, the presence of the crosslinking agent, and any changes in fiber morphology such as surface roughness.

4.2 Experimental Details

A schematic of NFES is shown in Figure 4.1a with a corresponding optical image of NFES taking place shown in Figure 4.1b. The dye-doped polymer solution was loaded into a 1 mL syringe and pumped through a 27-gauge blunt-tip hypodermic needle at a rate of 10 µL/h using a syringe pump (NE-1010, New Era). A high voltage source (NO3.5HP8.5, Acopian) was used to apply 2 kV between the needle tip and substrate. The SiO_2/Si substrates had dimensions of 15 x 15 x 0.5 mm and the glass substrates had dimensions 15 x 15 x 1 mm. The substrates were placed on top of an X-Y stage (A-LSQ300D, Zaber) programmed so fiber would be deposited in a parallel-line pattern, as shown in Figure 4.1a. The substrate was previously scribed with lines perpendicular to

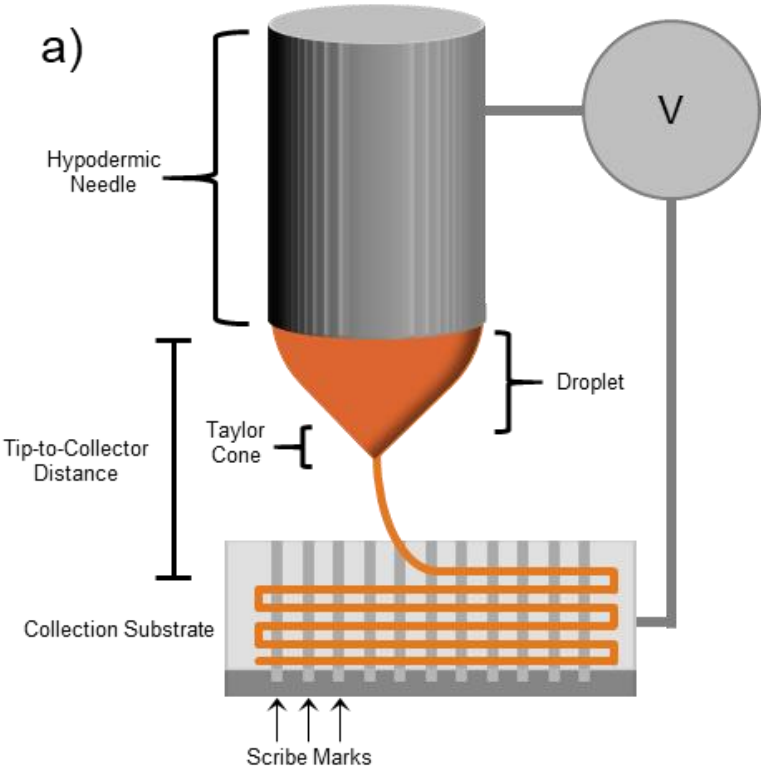

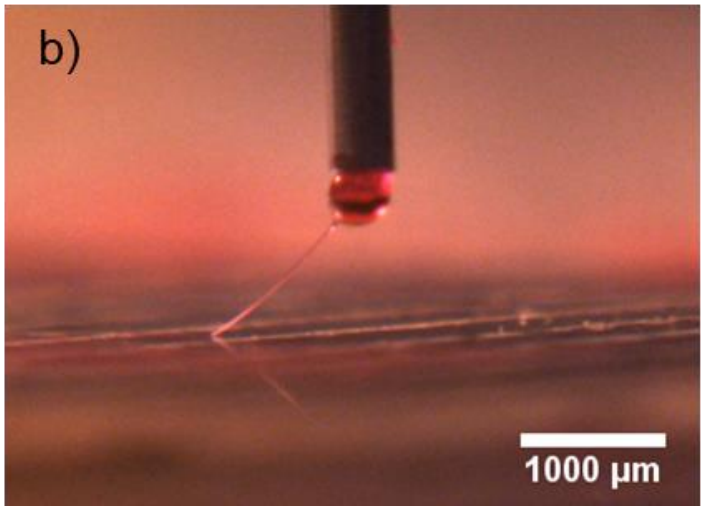

Figure 4.1: a) Schematic of NFES system showing fiber formation in a zig-zag pattern on a collection substrate and b) Optical image of NFES of R6G-PVA taking place on a glass substrate. The arrow indicates the direction of the stage travel.

the fiber deposition direction to allow fibers to be suspended. Fibers were written ~200 µm apart from each other. The needle tip-to-collector (T-t-C) distance was fixed at 1.25 mm. Electrospinning was performed under ambient temperature, pressure, and humidity. Though these conditions can affect fiber morphology[59,85], they were not controlled. Electrospun fibers were optically characterized using a digital optical microscope (KH-7700, Hirox) with a 35x objective and built-in measurement software. For cross-sectioning, the ends of the fibers were glued to the substrate, immersed in liquid nitrogen, and the substrate was broken along a scribe. While still in liquid nitrogen, the samples were placed in a vacuum desiccator for 24 hours to prevent condensation from forming on the fibers. An SEM (Vega3, Tescan) was used to image fiber morphology of the as-spun fibers and another SEM (NNS450, FEI) was used for the crosslinked fibers.

To crosslink the PVA fibers, a three-step process was used that was in part derived from previous reports[86,87]. After gluing the ends of the fibers to the substrate, the fibers were placed in a closed chamber and simultaneously exposed to vapor from a 1 M HCl solution and a 50% GA solution for 24 hours. Next, the fibers were exposed to vapor from a 5 M HCl solution and a 50% GA solution for 24 hours. For the last step, the fibers were completely submerged in a 50% GA solution for 24 hours, rinsed thoroughly with water, and allowed to dry in a vacuum chamber with dessicant. For further analysis, Raman spectra was taken of crosslinked and pure PVA thin films (LabRam, Horiba Scientific).

4.3 Results and Discussion

4.3.1 Effect of Applied Voltage and Stage Speed on Fiber Diameter on SiO_2/Si Substrates

To examine the effect of applied voltage and stage speed on fiber diameter, electrospinning experiments were performed. It is expected that an increased voltage will lead to a larger electric field, causing a greater force that will overcome the surface tension of the polymer and initiate fiber formation[59,85]. Figure 4.2 shows a plot of fiber diameter vs stage speed at two applied voltages: 1.0 kV to 1.5 kV. Lower voltages were not examined because the electric field was not strong enough to induce fiber formation.

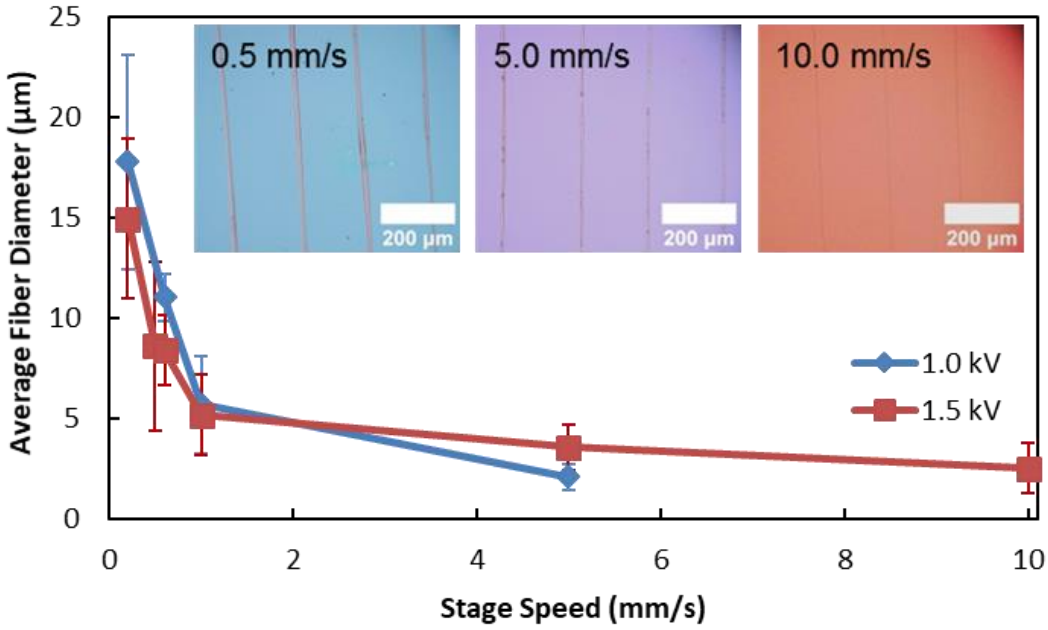

Figure 4.2: Fiber diameter as a function of stage speed at two voltages. The insets are optical images showing the parallel fiber patterns and reduced fiber diameters at different stage speeds.

Conversely, higher applied voltages were not examined because the electric field was near the dielectric breakdown of air. When higher voltages were used, an arc formed. Despite being a 50% increase in voltage, each data point produced no noticeable change in fiber diameter. This shows that, for this polymer system, the applied voltage does not have a significant impact on fiber diameter. For these reasons, it was determined that a suitable applied voltage to electrospin at was the highest applied voltage that allowed electrospinning without arcing: 1.5 kV in the case using the SiO_2/Si substrates.

The fiber diameters were also measured as a function of stage speed. The stage speed was varied between 0.2 mm/s and 10 mm/s while electrospinning. It should be noted that when electrospinning ceased, it was typically by spontaneously breaking of fiber formation. This phenomenon introduced a tradeoff when it came to stage speed: faster stage speeds allowed more fiber to be deposited because more fiber could be deposited before electrospinning broke. Conversely, slower stages speeds would deposit fewer fibers before electrospinning broke but produced larger fiber diameters that would be more likely to support optical resonance. Figure 4.2 shows that when stage speed increased the fiber diameter decreased. This is because the x-y stage moves faster than the fiber is extracted from the droplet. As a result, the fiber was pulled mechanically pulled from the droplet as well as electrospun as it was drawn onto the substrate. This mechanical drawing elongated the fiber and decreased the fiber diameter[79]. Examining the 1.5 kV curve reveals that at 10 mm/s, the average fiber diameter was its lowest: 2.52 ± 1.27 μm. As the stage speed decreased, the fiber diameter becomes 3.59 ± 1.13 μm at 5 mm/s, and increases to 14.93 ± 3.98 μm at 0.2 mm/s. The insets of the figure show

optical images of fibers at three different stage speeds (different colors correspond to different SiO_2 layer thickness). The fibers become visibly larger at slower stage speeds. This information was utilized to adjust the average fiber diameter to the size range that is needed to support WGM resonance as predicted by FDTD simulations. A stage speed of 0.5 mm/s was selected to electrospin all further samples at because it was slow enough to allow the fibers to remain large enough to easily support WGM resonances, but also fast enough that it allowed long sections of fiber to be easily deposited on each sample. An average of 19 lines of fiber out of a possible 61 were deposited on each substrate at this stage speed.

4.3.2 Effect of Time on Fiber Diameter

As mentioned in chapter 3, the viscosity for this low molecular weight solution increases rapidly over time. To determine if this rapid change in viscosity had a significant role in affecting fiber diameter, the fiber diameter was compared across multiple consecutively electrospun samples. Figure 4.3 shows a plot of average fiber diameter from sample-to-sample as a function of the solution's age for two separate electrospinning days. It took approximately 30 minutes to electrospin each sample, so data points are placed accordingly, with the first point place at 30 minutes. Typically, three or four samples were made in each electrospinning session, so the time spent electrospinning rarely was longer than two hours. Data taken on 8/2/2016 showed that there was a slight increase in average fiber diameter across samples. The diameters went

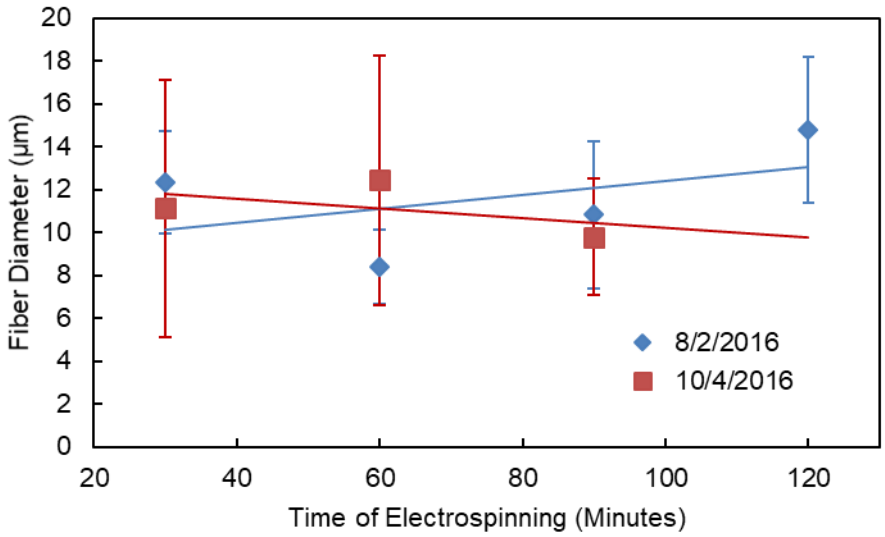

Figure 4.3: Average fiber diameters as a function of time of electrospinning on two different days

from 12.3 µm for the first sample up to 14.8 µm to the final sample. Despite not being a large increase, this trend of increasing diameter with an increase in viscosity is expected; however, the fibers electrospun on 10/4/2016 under identical conditions shows the opposite trend. The first sample gives a diameter of 11.1 µm and the last gives a diameter of just 9.8 µm. Once again, the difference in fiber diameters over time was not large. The observation of the opposite trends in fiber diameters on different days, along with the large standard deviations in fiber diameters indicated that any change in solution viscosity over the two hours of electrospinning did not play a significant role in dictating fiber diameter. This may be due to the mechanical agitation the solution undergoes while being pumped through the syringe[76].

4.3.3 Effect of R6G Incorporation on Fiber Diameter

R6G powder was incorporated into the PVA solutions at a concentration of 0.0007 gR6G/gPVA, electrospun, and the subsequent diameters were analyzed. This was the highest dye concentration in which electrospinning was observed while using the SiO_2/Si substrates. Figure 4.4 shows the histogram of fiber diameters of pure PVA fibers and R6G-PVA fibers. The average diameters for the pure PVA fibers is 11.4 ± 3.1 μm

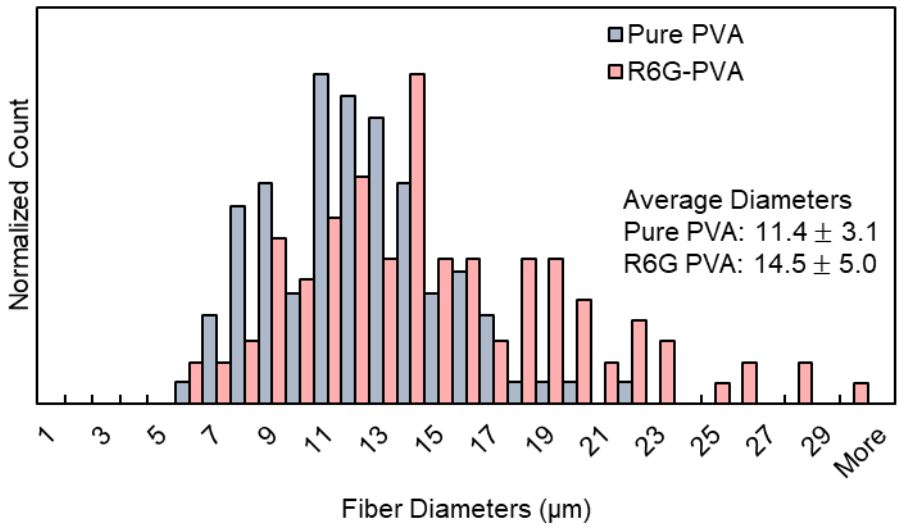

Figure 4.4: Histograms showing fiber diameter distributions of Pure-PVA fibers and R6G-PVA fibers.

while for the R6G-PVA fibers it is 14.5 ± 5.0 μm. Despite there being an increase in fiber diameter of 3 μm in the R6G-doped case, the standard deviation is also much greater. Inspection of the histogram reveals that both groups of fibers have very similar size distributions, however, the R6G-doped fibers had a few more data points in the 20+ μm

range. These data points are likely caused by dried out portions of the droplet being deposited along with the fiber, causing sections of fiber with relatively enormous diameters. These data points created both the larger average and standard deviation for the dye doped fibers and are not believed to be a product of the dye incorporation. Judging from the distributions as a whole, the addition of R6G-dye does not appear to have a significant effect on fiber diameter. This corroborates the solution physicochemical measurements where the incorporation of R6G dye did not significantly change the values of viscosity, surface tension, and conductivity and, subsequently, did not change electrospun fiber diameters.

4.3.4 Effect of Substrate on Fiber Diameter

To perform subsequent optical characterization, a transparent substrate was needed, and the substrate was changed to glass. Upon making this change, it was observed that electrospinning initiated more readily on a 1.0 mm thick glass substrate than a 0.5 mm thick SiO_2/Si wafer. As previously mentioned, on the SiO_2/Si wafer, the average amount of lines being deposited on a single substrate was 19, with the most being 45. On the glass substrates, otherwise electrospun under identical conditions, the average number of fibers deposited on the glass substrates was 40, with the most being 56. The fiber diameters were measured and Figure 4.5 shows the normalized histograms of the R6G-doped PVA fiber diameters electrospun on glass and SiO_2/Si. Both display the same Gaussian distributions and have similar average diameters. The average diameters are

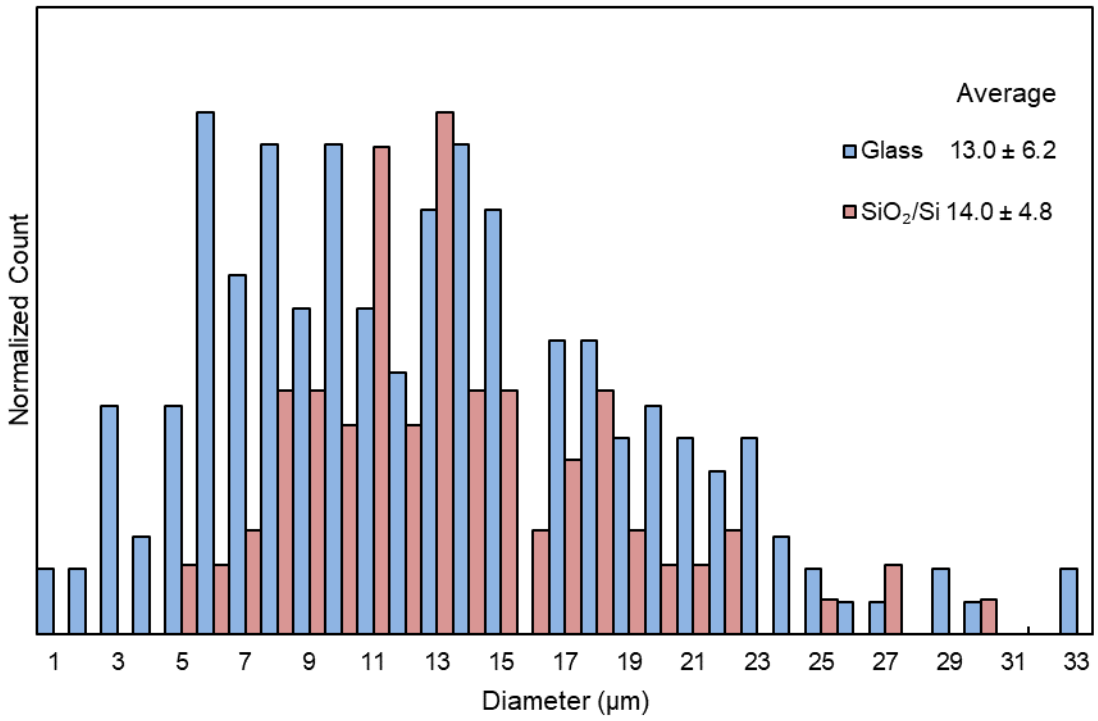

Figure 4.5: Histogram showing fiber diameter distributions between fibers electrospun at 0.5 mm/s on SiO_2/Si and glass substrates.

14.0 ± 4.8 μm for the SiO_2/Si substrate and 13.0 ± 6.2 μm for the glass substrate. This further indicates the robustness of the NFES process for this system as the change in substrate does not have a large affect in altering diameters. Finally, as mentioned in the effect of applied voltage section, the optimal applied voltage was the highest it could be without arcing, 1.5 kV in the case of the SiO_2/Si wafers. However, after changing the substrate to glass, the applied voltage was able to be increased to 2.0 kV because no arcing took place due to the extra thickness of the glass substrates which reduced the net

electric field between tip and collector, so 2.0 kV was subsequently used for further electrospinning purposes.

Lastly, the electrospinning analysis was extended to glass substrates and is shown in Figure 4.6. Figure 4.6a shows that fiber diameter was dependent on stage speed. Diameters increased drastically as stage speed was reduced to 0.5 mm/s. Furthermore, the values for the diameters on glass are nearly identical with the values on SiO_2/Si, again indicating that the stage speed is the dominant parameter for controlling diameter for these solution conditions. Optical images of fibers for each electrospinning condition, in addition to histograms of fiber diameter, are shown in Figures 4.6b-e and Figure 4.6f, respectively. The diameters are visibly larger at the slower stage speeds. Using a stage speed of 10 mm/s the average fiber diameter was 2.8 ± 1.3 μm, whereas a reduced stage speed of 0.5 mm/s increased the average diameter to 12.4 ± 5.9 μm. Thus, average fiber size was tuned by more than a factor of 4. Another observation is the breadth of fiber diameters that were produced. As the stage speed was reduced to 0.5 mm/s, a breadth of diameters ranging from ~2-33 μm are produced. This range of diameters will be useful for a comprehensive analysis of resonators across a large range of diameters. Stage speed can control the degree of mechanical drawing of the polymer solution during spinning, greatly influencing fiber diameter[67,88]. Similar trends have also been observed for stage speeds 2 to 40 times larger than used in these studies[67,79,86]. Furthermore, the fiber diameter's produced in this study are either larger or of similar diameters for other electrospun polymer resonators[60–63]. The combination of electrospinning parameters (e.g. solution, pattern dimensions, etc.) used here approached the spatial limitations of our

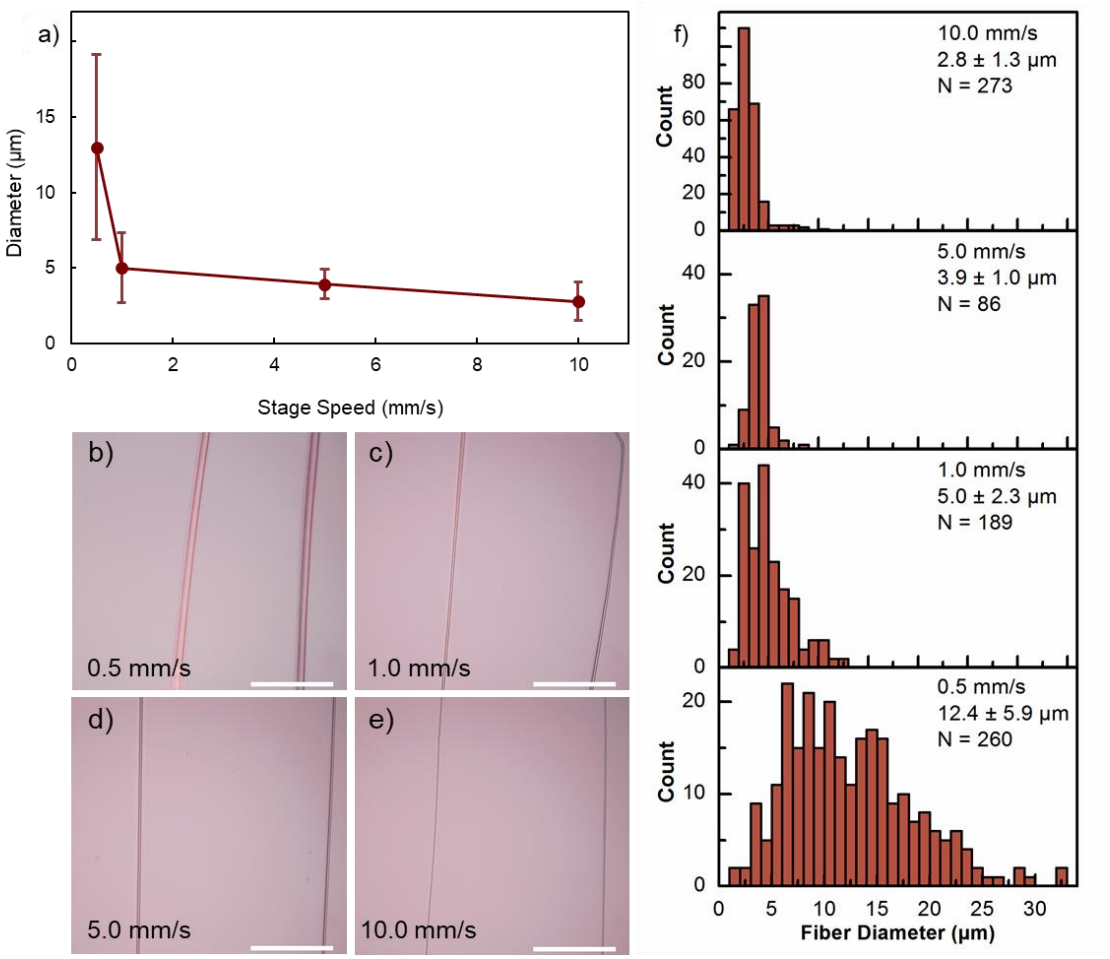

Figure 4.6: a) Fiber diameter vs stage speed for R6G-PVA fibers on glass substrates, b)-e) optical images showing the different fiber diameters at various stage speeds, and f) fiber distribution histograms of fibers electrospun at different stage speeds.

apparatus and controller. As a result, scan rate impacted pattern fidelity with write deviations increasing at higher speeds, particularly near end points. The use of rather viscous, high weight percent polymer solution and reduced stage speed enabled fabrication of larger fibers. The sizable diameters generated by a 0.5 mm/s stage speed

were compatible with observation of high quality WGMs, therefore fibers electrospun with these conditions were selected for further study.

4.3.5 Scribe Mark Fabrication and Characterization for Spinning Suspended Fibers

To suspend the fibers, a diamond scribe was used to create 5 - 10 parallel trenches onto the glass substrates where the fibers would be deposited perpendicular to the marks. The trenches were characterized for their width and depth. The results are shown in Figure 4.7. Figure 4.7a shows a representative image of a typical scribe mark. Major striations on the substrate can be seen due to the fracture surfaces of the glass when scribed. A darker line can be seen going down the middle of the image, which is where the largest portions of substrate were removed. Small residual pieces of glass that were not fully removed or cleaned off can also be seen throughout the image, though they would likely not affect electrospinning or resonance. Despite not being uniform, scribe marks were typically around a few hundred microns in width. Figure 4.7b shows a three-dimensional rendering of the trench with a cross-section marked by the blue plane. Figure 4.7c shows the profile of the depth of that cross-section. The maximum depth of the trench is around 40 μm, which is much larger than the depth the FDTD simulations determined the evanescent field penetrated (~340 nm), even for the smallest diameter fiber. For a more comprehensive analysis of scribe depth, Figure 4.7d shows a histogram of 15 different depth measurements. Every trench measured was deeper than 5 μm, with

an average depth of ~20 µm, and was a few hundred microns in length, indicating that these marks would allow resonance without any unwanted coupling to the substrate.

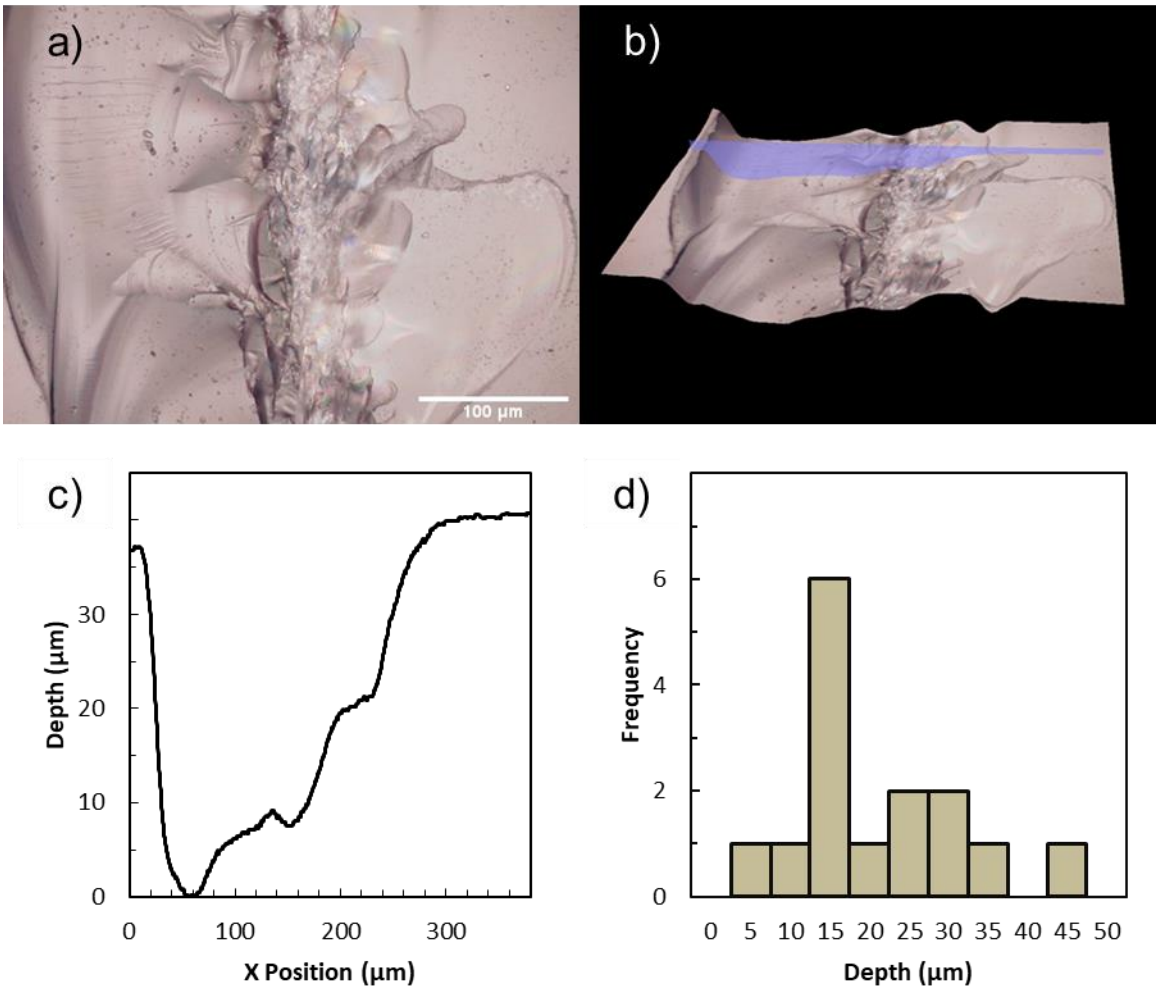

Figure 4.7: Characterization of scribe mark depth showing a) optical image of scribe mark, b) 3D rendering of the scribe mark in a), c) plot monitoring scribe depth along the width of the scribe mark, and d) histogram showing distributions of scribe mark depths over 15 different measurements.

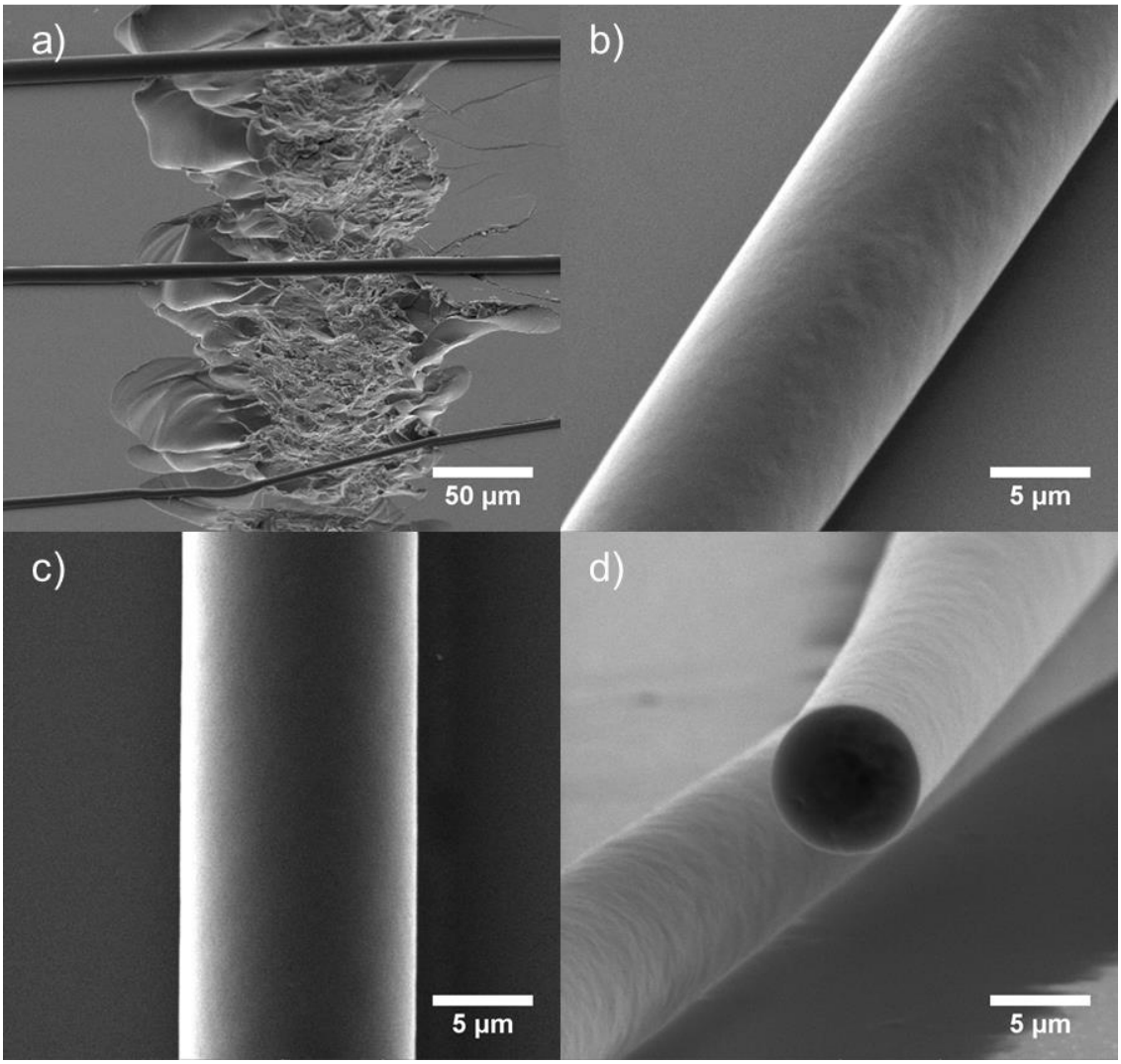

Figure 4.8: SEM images showing a) suspended fibers electrospun over a scribe mark, b) and c) perspective and top-down images showing surface texture of electrospun fibers, and d) cross-section of fiber showing circularity

4.3.6 Morphological Characterization of R6G-PVA Fibers on Glass Substrates

Using a scan rate of 0.5 mm/s, R6G-PVA fibers were electrospun on a glass substrate. Figure 4.8a shows SEM images of dye-doped polymer fibers suspended across

a scribe mark, respectively. No sagging or drooping was observed. Higher magnification electron microscope images, shown in Figures 4.8b and 4.8c, revealed smooth fiber surfaces without significant striations or ridges. Moreover, fiber cross-sections produced with the freeze-snap technique were circular, and void of flat regions or significant distortions in shape, as shown in Figure 4d. As revealed in Figure 4.9, fiber diameter was found to vary gradually with length, and no bead-like structures were observed. More

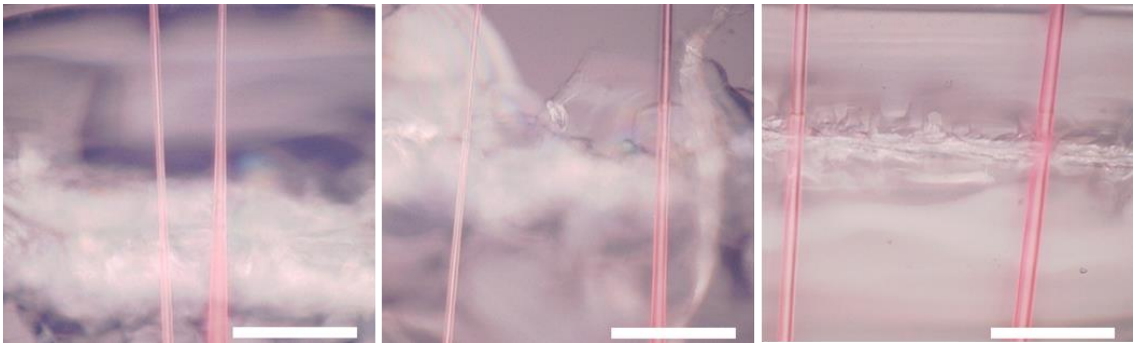

Figure 4.9: Optical images showing taper along the z-axis of the fibers. The scale bar is 100 μm.

than 15 fibers, with over 200 μm in length analyzed on each, indicated an average diameter change of 0.037 ± 0.034 μm per micron of fiber length. This observed taper is expected to play a role in the observed resonances.

4.3.7 Crosslinking and Morphological Characterization on Crosslinked Fibers

A three-step GA treatment was used to crosslink dye-doped PVA fibers, rendering them insoluble in aqueous solution that was, in part, based on previous reports[86,87] and, in

part developed in this work. Figure 4.10 compares fiber diameters of a sample before and after the crosslinking process. Fiber diameters increased approximately 13% from 12.4 μm to 14.0 μm, which is believed to be due to swelling and/or polymer relaxation associated with the water-based crosslinking process. Furthermore, additional fiber curvature developed and can be seen in Figure 4.11a. Figure 4.11 shows GA-treated PVA fibers immersed in water for 24 h remained impervious to dissolution and no additional distortion in shape was observed, though the fibers did migrate a small amount across the substrate.

Raman spectra of pure-PVA and crosslinked pure-PVA thin films from 750 cm^{-1} – 1600 cm^{-1} are shown in Figure 4.12. A majority of the signal can be attributed to the bonds of the PVA molecules[89,90]. However, the peaks that appear at ~804 cm^{-1} and ~1247 cm^{-1} on the crosslinked PVA spectrum may be indicative of the presence of pure GA in the film, though several other pure-GA peaks were not observed (1201, 1638, 1676, and 1710 cm^{-1}), likely due to the small amount of GA that actually gets incorporated into the membrane. The presence of bonds that were specific to PVA crosslinked with GA were not observed. This is likely because those Raman peaks are expected to be very low signal[90]. Nonetheless, since GA appears to be present and the fibers demonstrated water stability, the crosslinking process was deemed sufficient for aqueous sensing experiments.

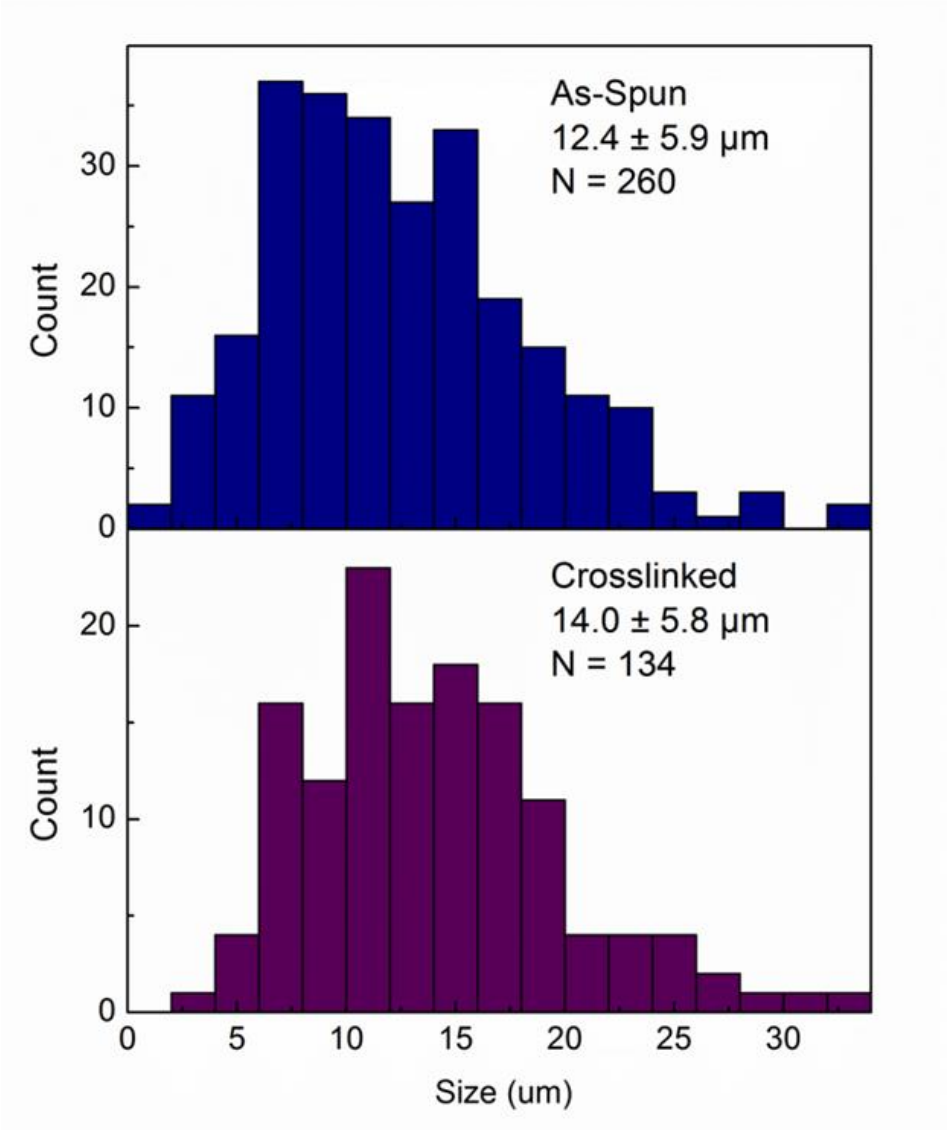

Figure 4.10: Fiber diameter distribution histograms of R6G-PVA fibers before and after crosslinking treatment.

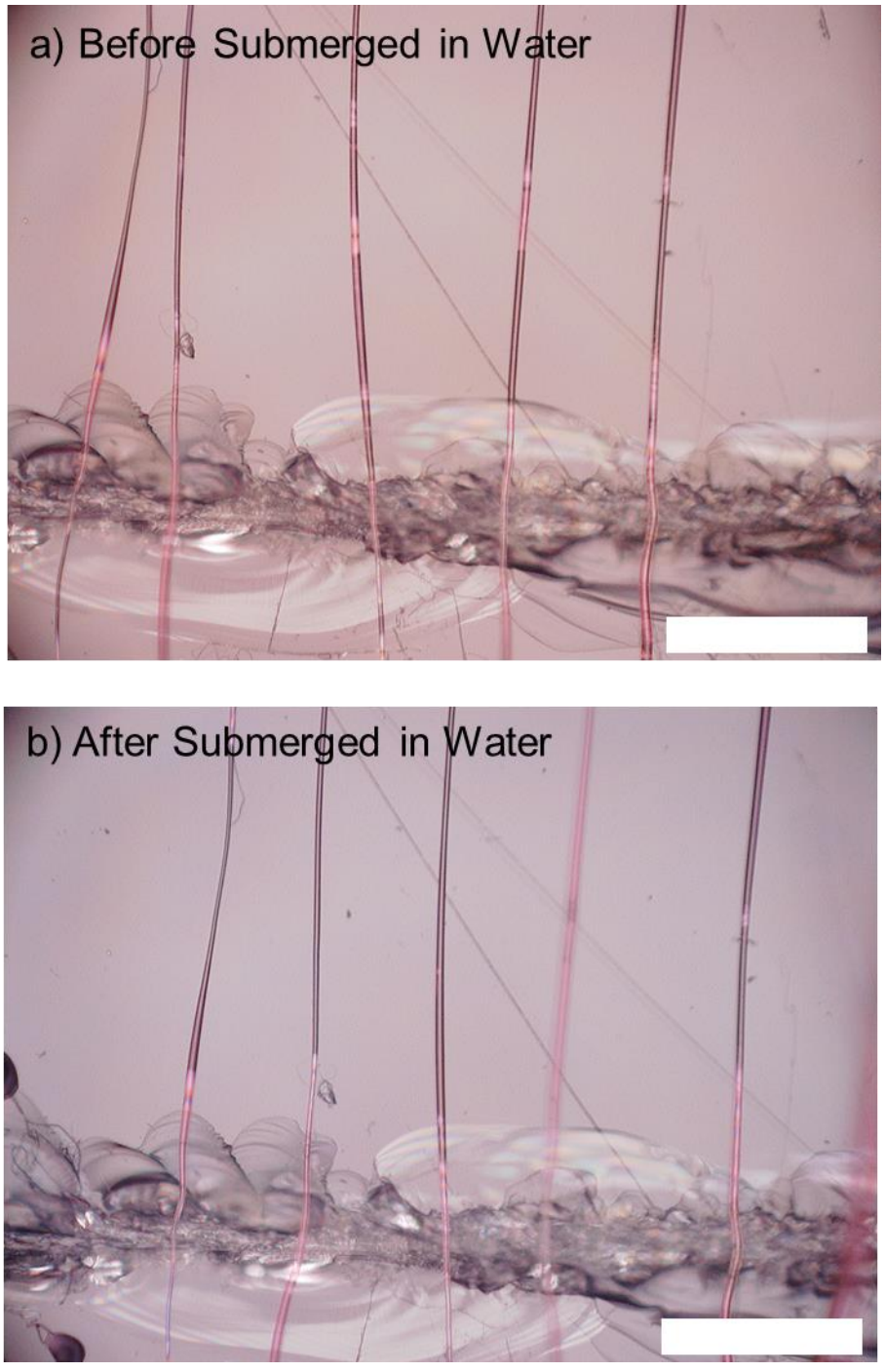

Figure 4.11: Crosslinked fibers a) before and b) after being submerged in water for 24 hours demonstrating their ability to remain viable after exposure to water. Scale bar is 100 µm.

SEM characterization was also performed to evaluate any change in surface texture of the fibers due to the crosslinking process, as shown in Figures 4.12b,c. Near the base of the fibers, some residual material can be seen on the substrate. This is believed to be polymerized GA leftover from the crosslinking process as it was not seen in the SEM images of the as-spun fibers in Figure 4.8. Furthermore, this residue was not seen around the fibers in suspended regions and was not expected to restrict resonance. The images show the fiber's surfaces remain smooth and do not indicate any noticeable changes in surface roughness on the fibers when compared to Figure 4.8b,c, which indicates that crosslinked fibers maintained their structure and should remain capable of supporting WGM resonance.

4.4 Conclusions

The applied voltage, stage speed, R6G incorporation, time of electrospinning, and substrates were all varied during the near-field electrospinning fiber characterization. The applied voltage, time of electrospinning, and the incorporation of R6G dye was determined to have an insignificant effect on the fiber diameter for samples made on SiO_2/Si substrates. The stage speed showed a 6x increase in fiber diameter as the stage speed was reduced from 10 mm/s to 0.2 mm/s. This parameter was utilized to optimize the production of fibers on each substrate, allowing for many lines of fiber to be written, while maintaining the size range needed to see WGM resonances. The stage speed that

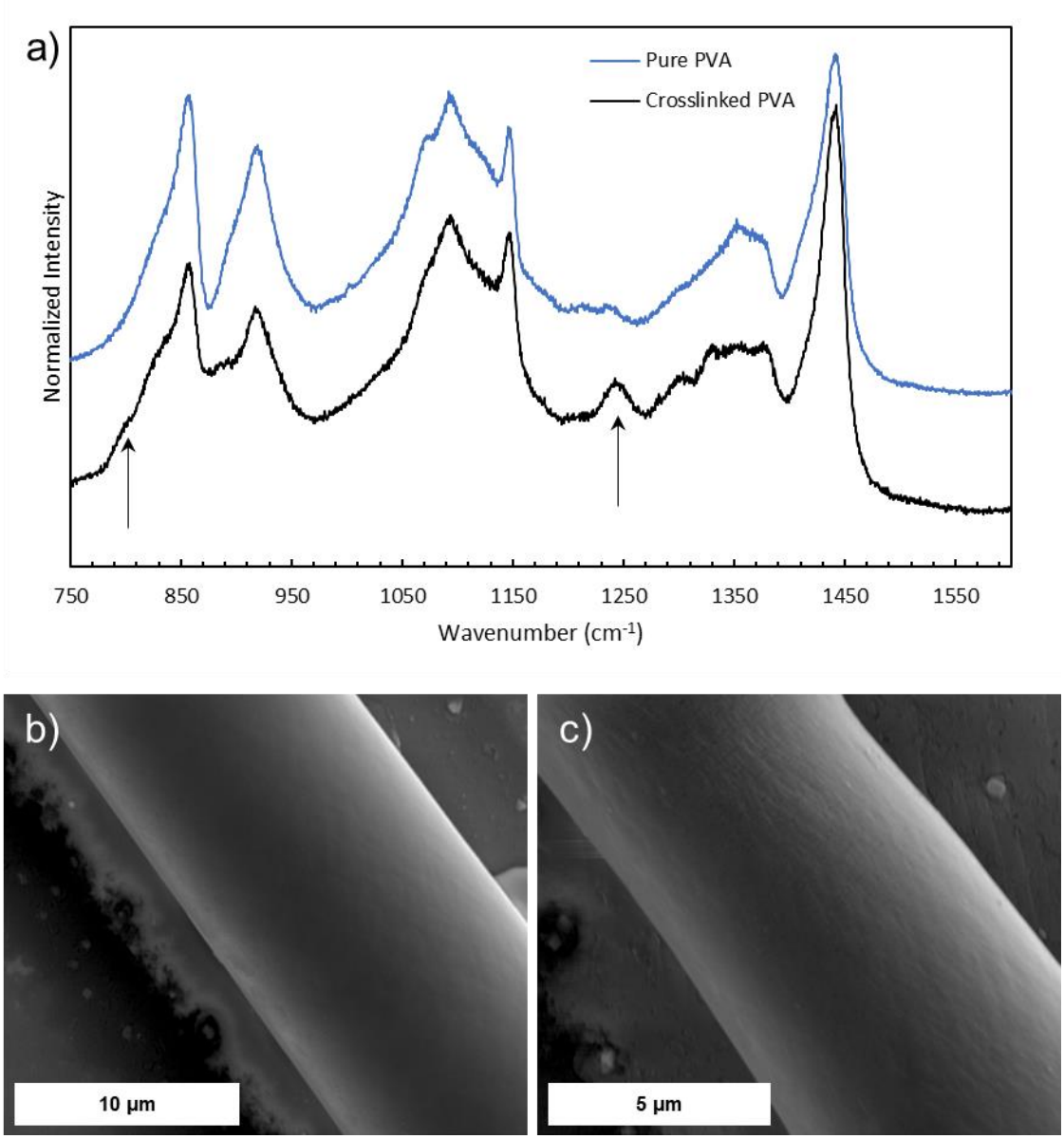

Figure 4.12: a) Raman spectra of crosslinked and not crosslinked pure-PVA thin films confirming the presence of GA and, b) and c) SEM images showing surface texture of crosslinked R6G-PVA fibers.

gave both many fibers written while maintaining fibers in the desired size range for electrospinning was determined to be 0.5 mm/s.

It was determined that changing the substrate from 0.5 mm thick SiO_2/Si to 1.0 mm thick glass did not substantially change the fiber's morphology. The fibers diameters were almost identical over the entire range of stage speeds for both substrates. Histograms showed that fibers electrospun at 0.5 mm/s showed a large breadth of fiber diameters, which would be useful for a comprehensive WGM study. SEM characterization showed fibers with smooth surfaces, circular cross-sections, and the ability to be suspended over scribe marks. Analysis with optical images showed the fibers had a gradual taper along the z-axis, which may affect their resonance ability. Crosslinking these fibers demonstrated their ability to become water stable, though a small increase in fiber diameter was observed. Raman spectra confirmed the presence of pure GA in the PVA, but did not show crosslinking-specific bonds due to a weak signal. Finally, SEM showed that the crosslinked fibers maintained their smooth surfaces and their structure.

Chapter 5. WGM Detection, Characterization, and Sensing

5.1 Introduction

Finally, WGM resonance needed to be detected in the fibers. Since the fibers had an emitter incorporated, a microphotoluminescence (μPL) system could be used. To verify the resonance was coming from WGMs, a mode-fitting process specific to WGMs, FSR analysis and comparison to the FDTD simulations, and polarization experiments needed to be performed. The effect of the previously measured taper along the fiber z-axis on optical resonance also needed to be investigated further. The Q factor needed to be measured as it quantifies the device's ability to contain resonance and serves as a basis for comparison among resonators with different diameters and with resonators from previous reports. By varying the input power and measuring the output power, the resonator's continuous wave (cw) lasing capabilities could be investigated, also, which could give valuable insight to their potential applications in optoelectronic devices. To demonstrate the sensing capability, organic solvent vapor sensing was performed with both as-spun and crosslinked fibers, however, device sensitivity was not able to be quantified with this system. Quantifiable sensing experiments with the crosslinked fibers

in an aqueous solutions demonstrated the device's use as bulk refractive index sensors. The device sensitivity was also measured for comparison to the literature.

5.2 Experimental Details

Confocal fluorescence microscopy (SP5, Leica Microsystems) was used to image of the dye-doped fibers. A laser confocal system (LabRam, Horiba Scientific) was used to evaluate the dye-doped PVA fiber WGM resonators. A schematic is shown in Figure 5.1. A single fiber was optically excited with 1 μW from a 532 nm CW laser (Ventus, Laser Quantum) focused to a spot size of approximately 3 μm using a 50x objective (NA = 0.75). Resonator emission was collected with the same objective, directed through a longpass filter (> 532 nm), and analyzed using a charge-coupled device (CCD) spectrometer with an 1800 lines/mm^{-1} grating.

For vapor sensing experiments performed on both as-spun and crosslinked fibers, shown in Figure 5.2, the sample was placed in a petri dish that was sealed with parafilm. Small quantities of liquid organic solvent (isopropanol or methanol) were pumped into the chamber through a small opening in the side of the dish. For ethanol sensing experiments in an aqueous environment, the sample was submerged in a pool of water in a petri dish, this time, the dish was not sealed. The ethanol concentration of the solution was varied from 0% - 30% by volume. The volume of the pool was kept constant. A 50x long-working-distance (NA = 0.50) objective was used, and the excitation power was

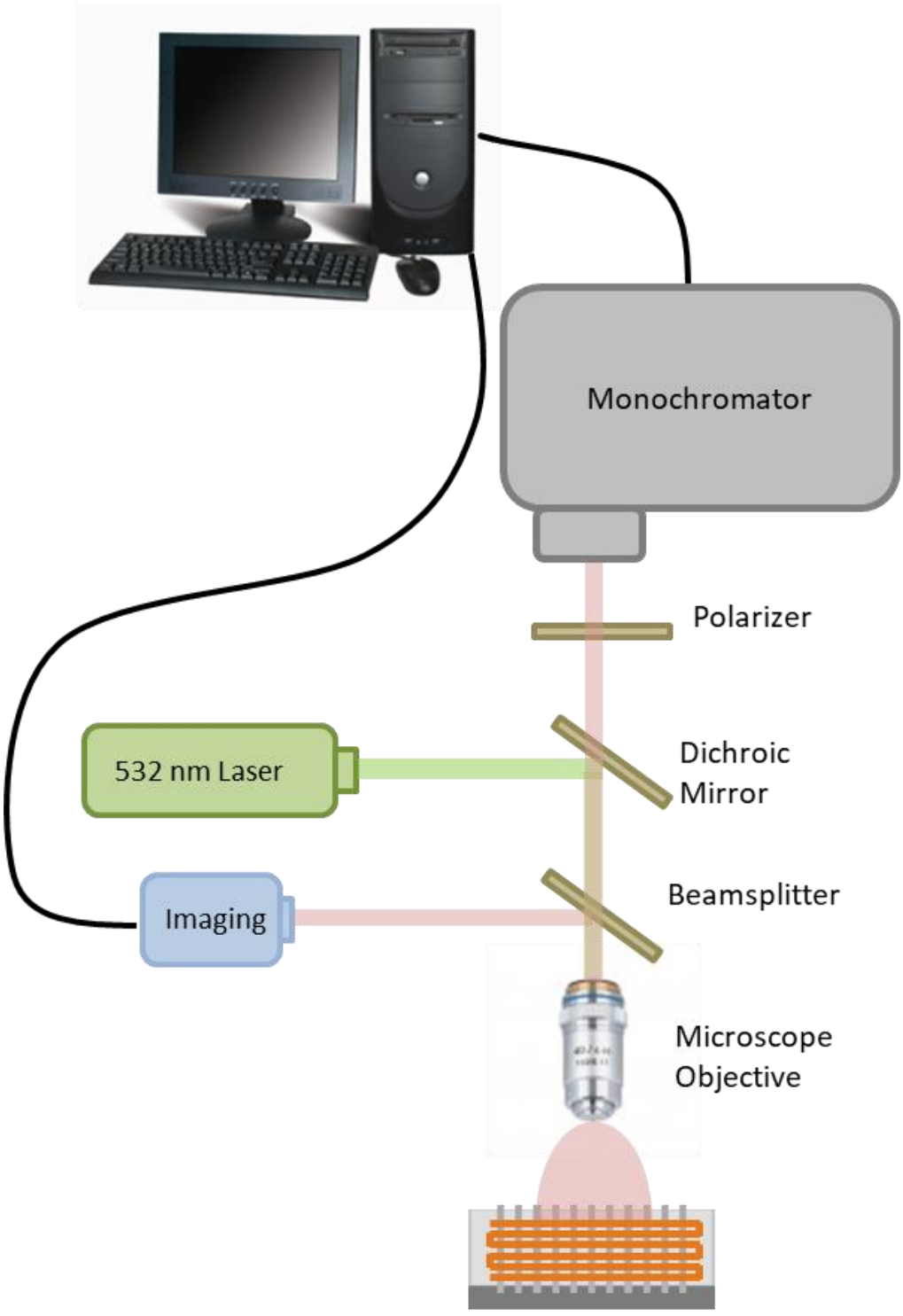

Figure 5.1: Schematic of µPL system. The path of the excitation beam is tracked in green and the path of the emission is tracked in red.

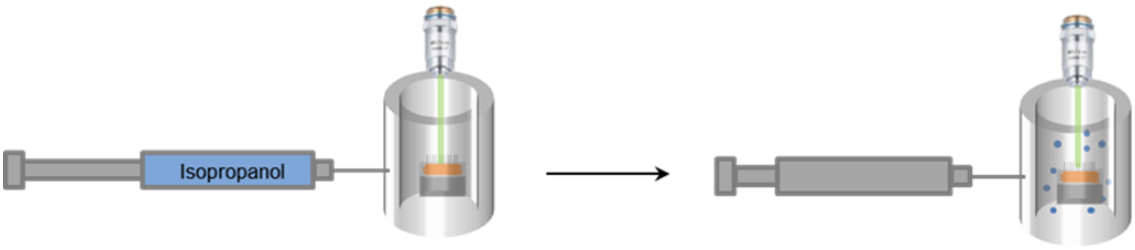

Figure 5.2: Vapor sensing setup. The sample is placed in a petri dish under the µPL objective. Small volumes of IPA or methanol were pumped into the chamber and the spectrum was incrementally measured.

increased to 2 µW because of the loss of excitation power at the interfaces of the petri dish or the water.

5.3 Results and Discussion

5.3.1 Emission, Mode Assignment, and Polarization Studies

Figure 5.3, shows the fluorescence emission along the length of three consecutively written lines of fiber. R6G fluorescence was bright and relatively uniform throughout the fibers, without evidence of substantial dye molecule agglomeration. Emission from the R6G-doped fiber optical cavities was measured using a µPL set-up. To minimize dye bleaching yet ensure an adequate signal-to-noise ratio, 1 µW of excitation power was used. Figure 5.1a shows a representative spectrum of a single, as-spun dye-doped PVA fiber with a measured diameter of 4.2 µm. The investigation

focused on wavelengths greater than 575 nm due to the minimal overlap in R6G absorbance and emission within this spectral region. Paired groups of sharp resonances were observed to decorate the broad fluorescence emission of R6G. A polarizer that was placed between the fiber and the monochromator was used to distinguish modes with similar electromagnetic field oscillation. Representative polarization-dependent spectra are shown in Figure 5.4b. Within a group, all the peaks were the same polarization. The shorter and longer wavelength groups were TM and TE, respectively. Spectra were further analyzed using an asymptotic formula for resonance and mode identification

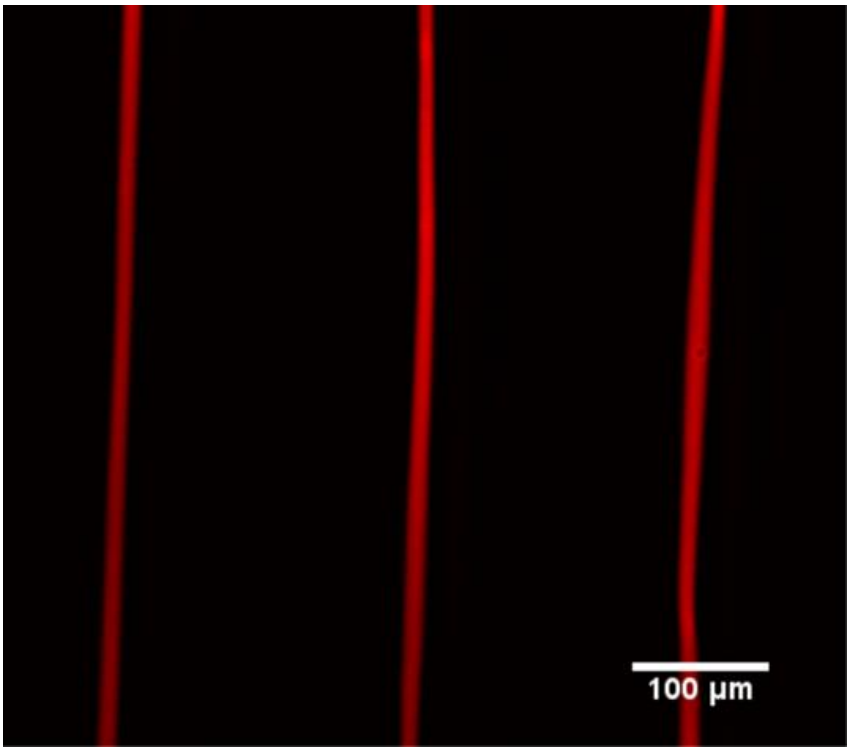

Figure 5.3: Confocal fluorescence image showing R6G fluorescence down the length of the fibers.

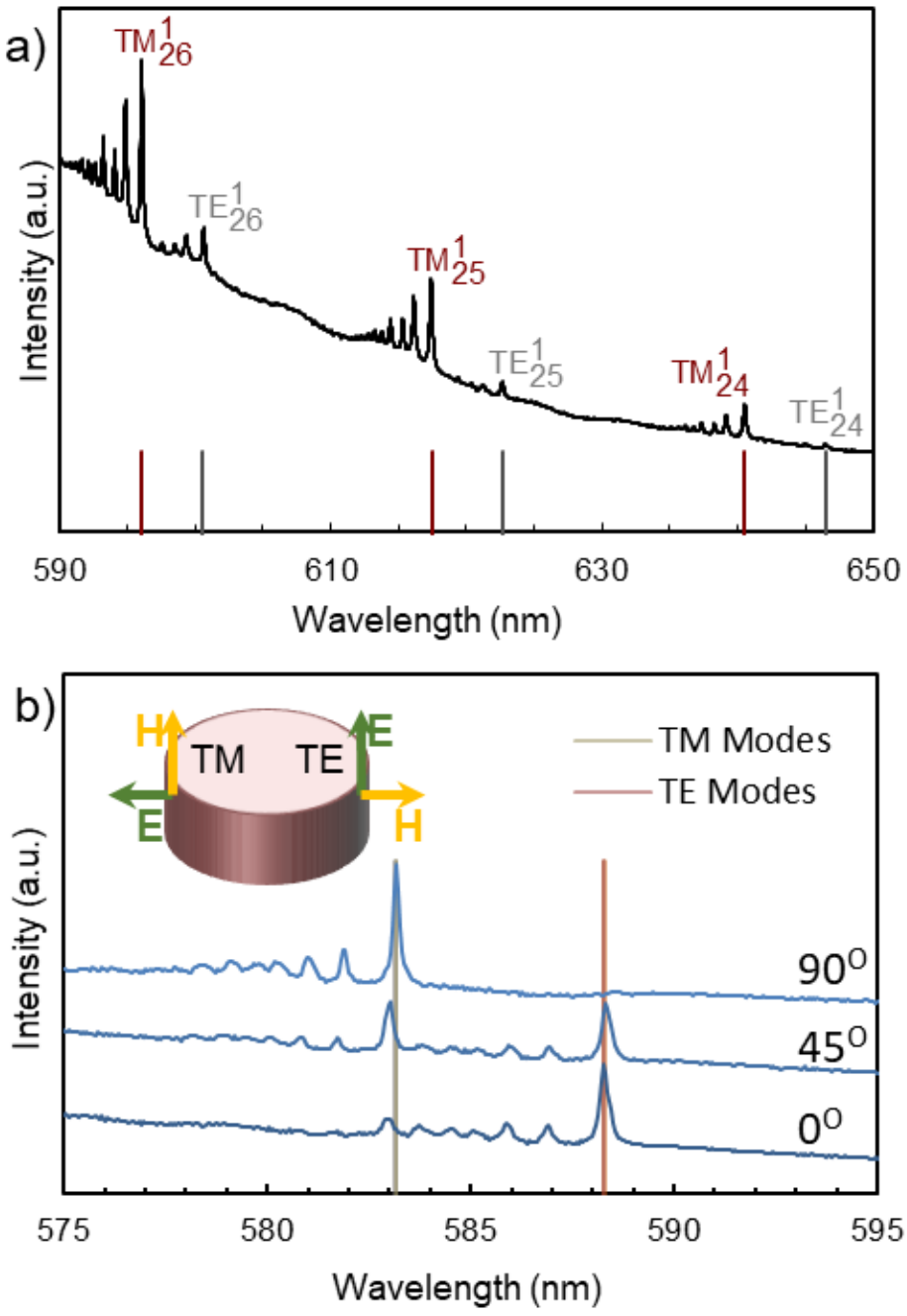

Figure 5.4: a) Spectra of 4.2 µm fiber showing groups of peaks with different polarizations and b) µPL spectra with polarizer of a 4.7 µm fiber showing longer and shorter wavelength groups of peaks having different polarizations.

based on Mie theory[91]. The formula, as developed by Lam et. al. is[91]:

$$n_{eff}\frac{n_h 2\pi R}{\lambda_0} \approx \nu + \frac{\alpha_s \nu^{\frac{1}{3}}}{2^{\frac{1}{3}}} - \frac{P}{(n^2-1)^{\frac{1}{2}}} + \frac{3}{10}\frac{\alpha_s^2}{2^{\frac{2}{3}}\nu^{\frac{1}{3}}} - \frac{P\left(n^2-\frac{2P}{3}\right)}{(n^2-1)^{\frac{3}{2}}}\frac{\alpha_s}{2^{\frac{1}{3}}\nu^{\frac{2}{3}}} + \cdots \quad (6)$$

Where P = n_{eff} or P = 1/n_{eff} for TE and TM modes, respectively. α_s is the negative of first airy root, 2.338, since all modes we analyzed are assumed to be first radial order. Lastly, ν = m+1/2 and n_h being the RI of PVA (1.464). This equation was programmed into Excel with R, n_{eff}, and AMN adjusted for best fit using the least squares method. Mode assignments in Figure 5.4a used a diameter of 4.6 μm, close to the measured value of 4.2 μm, and n_{eff} of 1.288 (TE) and 1.266 (TM), which were consistent with ellipsometry measurements and FDTD simulations. Because TM and TE modes penetrate the surrounding environment to different degrees, a small difference in n_{eff} values was appropriate.

5.3.2 Explanation of Peak Groups

Next, the groups of closely spaced modes were attributed to WGMs supported within the fiber cross-section, in addition to spiral or conical modes with finite longitudinal components and wavelengths slightly smaller than WGM resonance[92–94]. Variations in fiber geometry including both bottle structures[95,96] and tapers[97,98] can facilitate the observed optical confinement. In particular, the aforementioned diameter changes along the fiber z-axis were likely contributors. As shown in Figure 5.5a, emission was collected along the length of the fiber in 800 nm increments. Within each

spectrum the dominant intensity peak was dependent on measurement location. As the excitation and collection optic was scanned along the fiber length, resonance features emerged and faded within a very short distance, typically < 10 µm, indicating fairly compact mode localization. Furthermore, an individual mode appears then disappears over a range of ~3 µm, which is also the size of the excitation spot. Figure 5.5b is a schematic that shows how various modes along the tapered fiber z-axis may be getting highlighted by the excitation spot. Additional electrospinning process development is

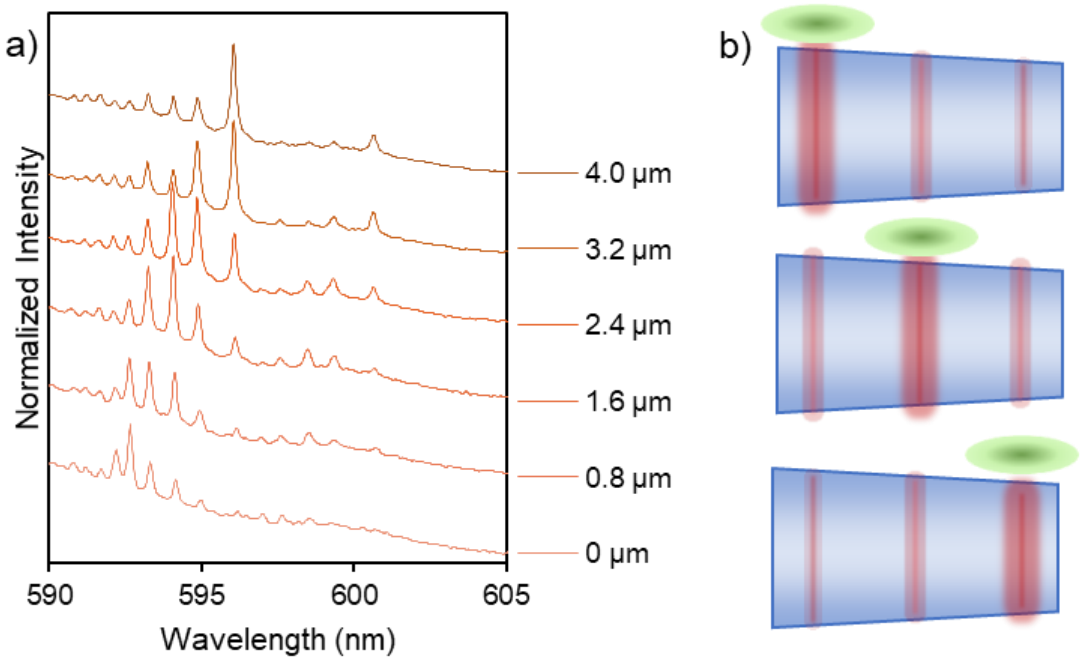

Figure 5.5: a) Spectra taken at different positions along the z-axis of a fiber showing a change in the peak with dominant intensity from a shorter wavelength to a longer wavelength and b) schematic showing different WGM having dominant excitation along the z-axis of a fiber with a taper.

required to more precisely control fiber diameter, and further suppress longitudinal resonance components.

5.3.3 Free Spectral Range Analysis

As illustrated in Figure 5.6a, the longest wavelength peaks, associated with in-plane WGM resonances, from two successive groups within the same polarization were used to determine free spectral range (FSR). At the smallest diameter resonator, individual peaks can be seen with a long FSR of 17.7 nm. As the diameter increases, the peaks become sharper and closer together, directly correlating to what was observed in the simulations. The spacing between consecutive modes was expected to decrease with increasing cavity length as defined by Equation 3. Also, more modes appear in the larger diameter resonators, which was attributed to these groups of peaks discussed earlier. FSR is plotted versus fiber diameter in Figure 5.6b for dye-doped electrospun fibers ranging from 3 to 14 μm in size. The inverse relationship between FSR and D (as emphasized by the solid curve), is characteristic of WGMs and further excludes both Fabry-Perot resonances[60] along the fiber length and random cavity resonances[61,62]. Furthermore, the 1/D curve from the FDTD simulations is plotted. The two curves follow each other nearly perfectly, with the FDTD curve lying slightly underneath the experimental curve. This is because the RI used for the simulations was slightly higher than the actual RI of the PVA. Nonetheless, this data further validates the argument that the observed resonances are WGMs.

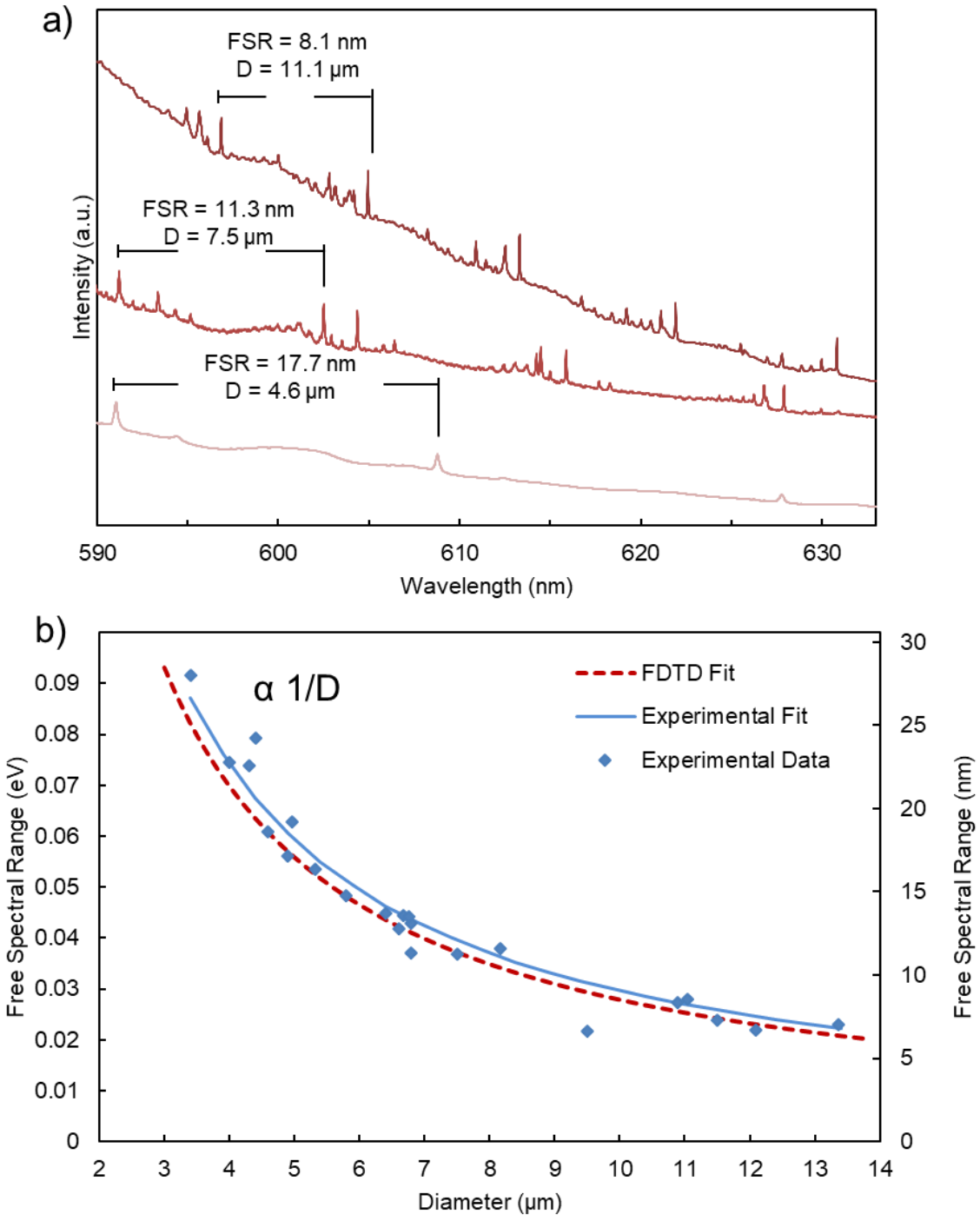

Figure 5.6: a) Spectra showing an increased Q and decreased FSR with increase in diameter and b) plot of FSR vs Diameter of several fibers.

5.3.4 Quality Factor Analysis

Cavity quality (Q) factors characterize the resonator's ability to sustain resonance. It is defined as[99]:

$$Q = \frac{2\pi c}{\lambda_0}\frac{Energy\ Stored}{Energy\ Lost\ per\ Second} = \frac{\lambda_{Resonance}}{\lambda_{FWHM}} \quad (7)$$

The Q factors in this system were extrapolated for several optical cavities by fitting each peak with a Lorentzian function. As mentioned in chapter 2, Q factors are limited by radiative decay, material absorption, and surface roughness. While the simulations were only limited by radiative decay, experimental devices are typically limited by one of the other two. The contributors for material absorption and surface scattering are[71,100]:

$$Q^{-1}_{Absorption} = \frac{\alpha\lambda}{2\pi n} \quad (8)$$

where α is the material absorption coefficient and

$$Q^{-1}_{Surface\ Scattering} = \frac{\pi^2\sigma^2 B}{\lambda^2 R} \quad (9)$$

where σ is the root-mean-square size and B is the correlation length of the surface inhomogeneity. One immediate observation is that the contribution for material absorption does not depend on diameter while the surface scattering and radiative decay does. This means that if a trend in Q factor is observed as a function of resonator size, the limitation on Q would be surface scattering.

A single high Q peak with a 0.044 nm FWHM is represented in Figure 5.7a and measured Q values for a range of as-spun fiber diameters are shown in Figure 5.7c. Given the relatively weak dependence of Q factor on diameter, radiative losses were not dominant, rather material absorption or more likely surface scattering were considered the main limitations on resonator performance[71,100].

The μPL spectra of several crosslinked fibers in air was also measured. Figure 5.7b shows the highest Q peak was a bit larger than in the as-spun case, having a value of over 19,700. Furthermore, as shown in Figure 5.7c, Q factors increased overall after crosslinking. Further studies are necessary to fully understand this phenomena, but it is believed that the crosslinking process may reduce fiber surface roughness and the associated scattering losses via solvent-vapor surface smoothing[101].

5.3.5 Yield Experiment

To determine how likely a WGM was to be present in a suspended region of fiber, a yield experiment was performed on the as-spun fibers. The experiment examined the regions of fiber suspended over scribe marks and determined if any WGMs existed in these areas. A total of 32 sections were measured on consecutive suspended regions of fiber on a single sample. Of the regions measured, 30 of them displayed clear WGMs giving a yield of 93.75%. This remarkable success rate further reinforces the ability of NFES to produce WGM resonators.

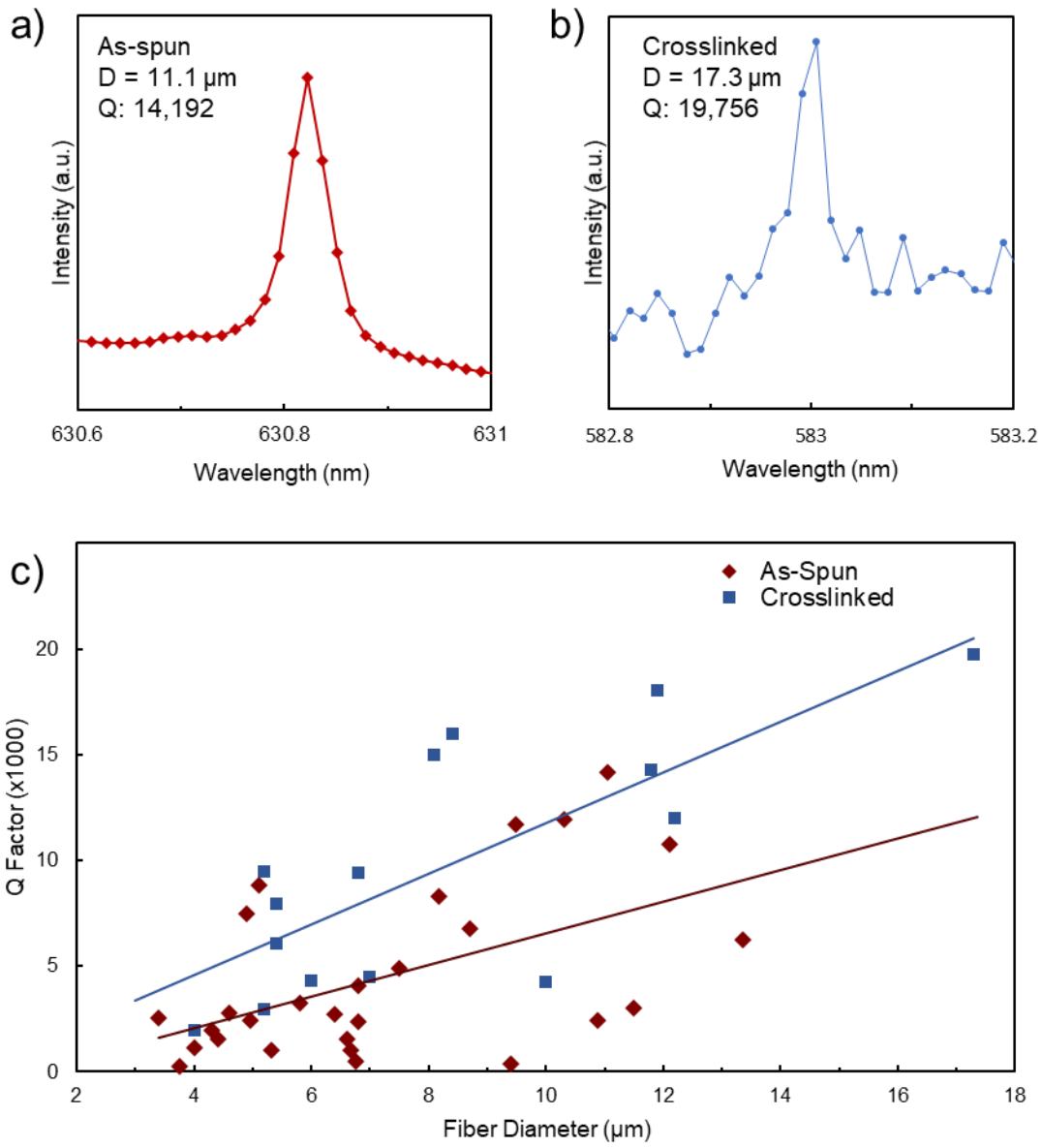

Figure 5.7: a) Highest Q peak from the as-spun fibers, b) highest Q peak measured of a crosslinked fiber, and c) plot showing increase in Q with diameter for both as-spun and crosslinked fibers.

5.3.6 Lasing Experiment

Excitation power experiments were performed to determine if lasing in the resonators was achieved. Power was incrementally varied from 5 nW to 50 μW. Figure 5.8a shows three spectra at different excitation powers. The spectra show an increase in output intensity; however, the P_{out}/P_{in} plot shown in Figure 5.8b shows that as the excitation power was increased, the output intensities do not change slope. Instead, they continue to increase linearly up to 5 μW, confirming that they remain in the spontaneous emission regime. Furthermore, no modes begin to dominate the emission spectra or show a narrowing of FWHM, which would also be indicative of lasing[64,102,103]. Beyond which the output intensity plateaus, which may be indicative of photobleaching, likely due to the insufficient photostability of fluorescent dye for cw lasing applications, a common problem for cw dye lasers[104].

5.3.7 Bulk Refractive Index Sensing

WGM resonators have shown great utility as chemical and biological sensors[13,17,21].This is because their evanescent waves, which extend into resonator surroundings, make them highly sensitive to environmental changes. Changes in RI of environment increase effective index, causing the resonant wavelength to red-shift. Electrospun R6G-PVA fibers were assessed as sensors using isopropanol and methanol vapor, as well as ethanol in water as a model system.

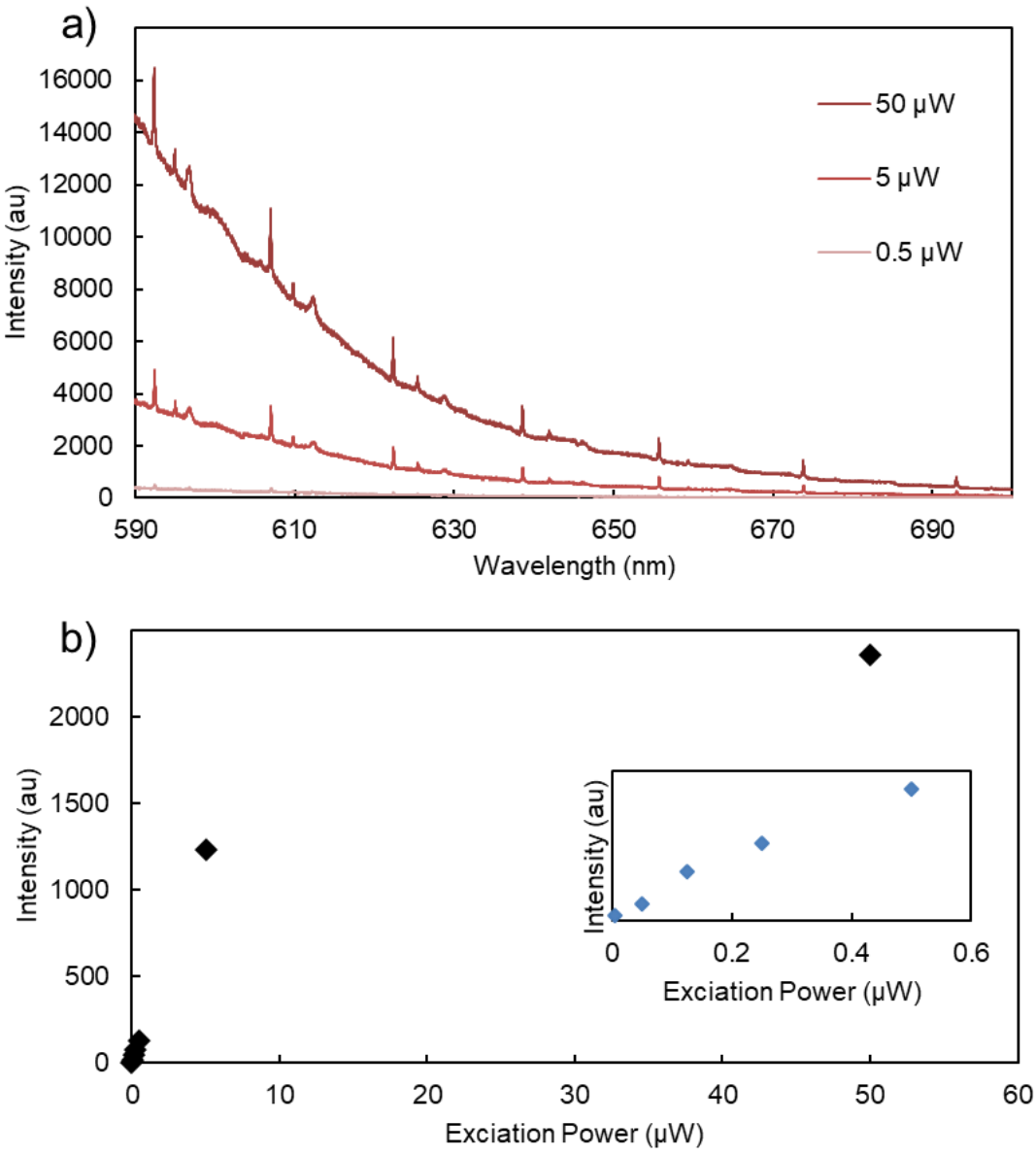

Figure 5.8: a) Spectra of a fiber at different excitation intensities and b) plot of peak intensity as a function of excitation power. The inset shows the same plot from 0 – 0.5 µW excitation showing linear increase in intensity with power.

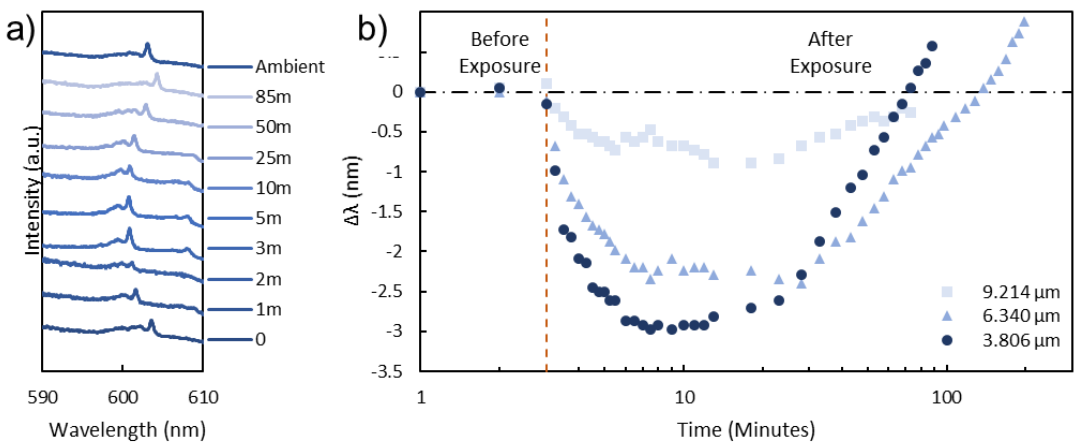

Figure 5.9: a) Stacked spectra showing the shift of peak wavelength over time exposed to IPA vapor and b) plot tracking change in peak wavelength over time of sensors with three different diameters.

5.3.7.1 Isopropanol Vapor Sensing of As-Spun Fibers

The results of the IPA vapor sensing experiments are shown in Figure 5.9. Figure 5.9a shows the WGM spectra of a 3.806 µm diameter fiber at different selected exposure times to IPA vapor. At time zero, just before exposure to vapor, a distinct WGM peak can be seen. After exposure to vapor for just 1 minute, the peak had already blue shifted by about 2 nm. By 5 minutes, the peak had blue shifted almost 3 nm from its original position. After continuous exposure to vapor, the peak began to red shift around 10 minutes. This shift continued to a value slightly past the initial position at 85 minutes. Finally, after removing the sample from the chamber and leaving it in ambient conditions for ten minutes, the peak position returned to its initial point.

The same experiment monitoring peak shift with exposure to IPA vapor was repeated with two larger fibers of diameters 6.340 μm, and 9.214 μm. Figure 5.9b plots the peak position as a function of time for all three fibers. The same trend of a blue-shift followed by a red-shift was observed with the two larger fibers. Before exposure to any IPA vapor, all WGM peaks were stable over a time span of three minutes. As soon an IPA was pumped into the chamber, however, all fibers displayed an immediate blue-shift, followed by a red-shift that occurs over a much longer time. The two larger fibers appear to display a small discontinuity in their peak shifts around two minutes. This is likely due to the μPL machine drifting off fiber or the microscope losing focus due to the presence of IPA vapor changing the RI inside the chamber or condensing on the inside of the petri dish, causing a high signal-to-noise and the measured peak position to become less accurate. The small discontinuity happened after the fiber was re-aligned in both cases. Further observation into the peaks' maximum blue shifts shows a correlation between fiber size and the peak's blue-shift. As the fiber diameter increased, the maximum blue-shift decreased substantially. The 3.806 μm fiber shifted by 2.97 nm, while the 6.340 μm and 9.214 μm fibers shifted by just 1.41 nm and 0.89 nm, respectively. The reason for the larger blue shift in the smaller fibers is likely that the mode volume takes up a larger fraction of the entire resonator than with the larger diameters, so the effect of the reduced n_{eff} is more significant in the blue-shifting regime.

Based on these wavelength shifts, the sensing was determined to be due to solvent uptake by the resonator causing an initial reduced n_{eff} which led to a blue-shift, followed

by swelling, which led to red-shift, which has been reported previously[105]. The phenomenon of the smaller fibers having a greater blue-shift can be explained by the smaller fibers having less polymer swelling while the vapor diffuses over the WGM volume, causing the reduction in n_{eff} to have a more dominate effect on the blue-shift than in larger fibers.

5.3.7.2 Methanol Vapor Sensing

To further characterize vapor sensing, a smaller polar molecule, methanol, was used for both an as-spun and a crosslinked fiber. Figure 5.10a shows the peak position over time after exposure to methanol of a 5.1 μm as-spun fiber. The same blue-shift and red-shift is observed, though on a much shorter time frame. The max blue-shift was 1.9 nm, close to what was observed for a fiber of similar size with IPA vapor. Furthermore, the red-shift is much larger than the IPA case. This fast reaction is likely due to the fast evaporation and small size of the methanol molecule[64]. The small size allows faster diffusion into the fibers as well as much more diffusion, causing a much more drastic amount of fiber swelling and the subsequent red- shift. After about 30 minutes, the peak began to blue-shift until it returned to its initial location after 73 minutes. This was likely just that the chamber was not completely sealed where the solvent was injected, causing the vapor to escape and the peak to return.

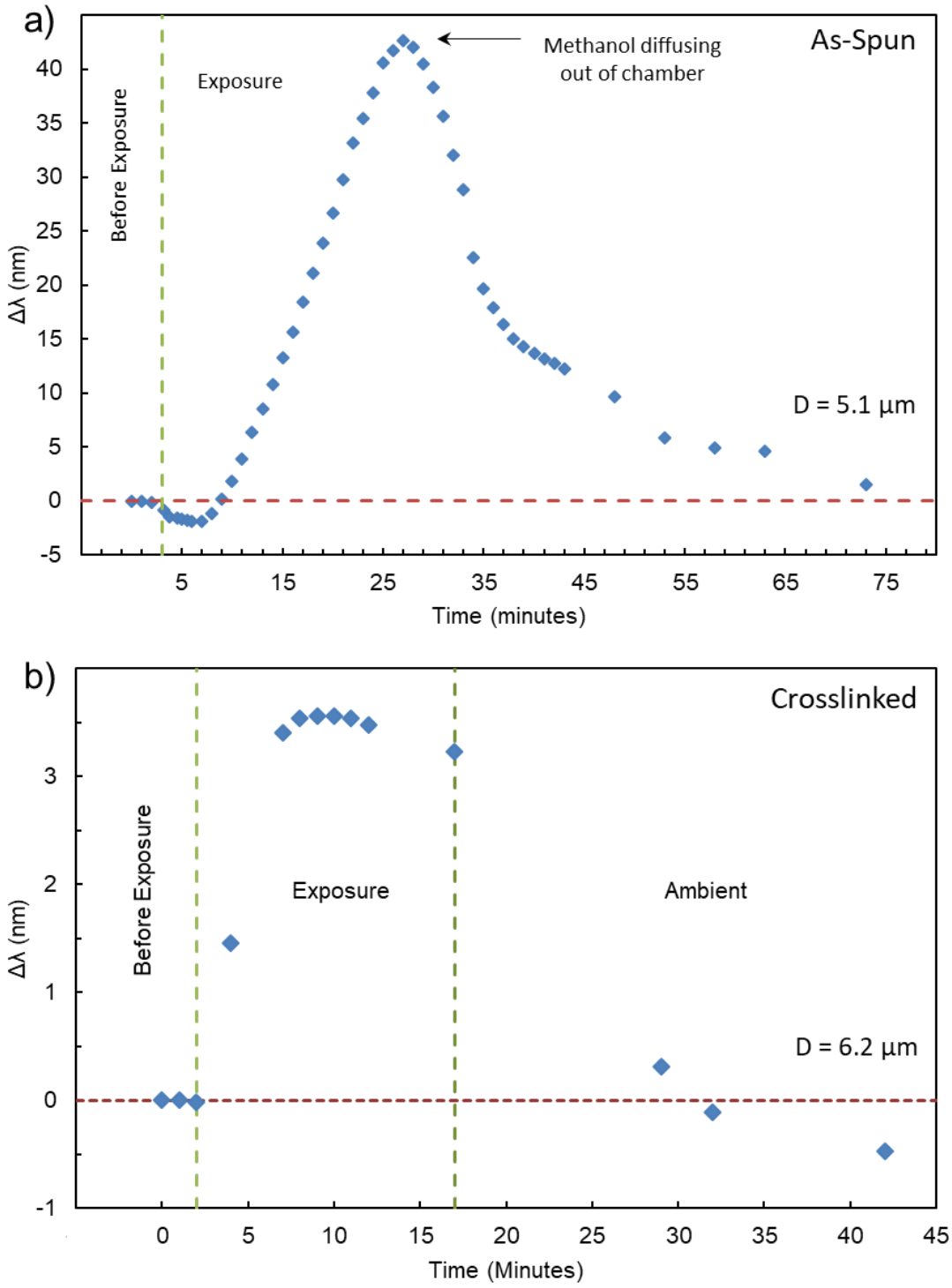

Figure 5.10: a) Peak position over time of a 5.1 µm resonator after exposure to methanol and b) peak position over time of a 6.2 µm crosslinked resonator after exposure to methanol.

Another experiment performed was exposing a crosslinked resonator to methanol vapor. The results are shown in Figure 5.10b. Contrary to the previous sensing experiments, no blue-shift is observed after exposure to vapor. Furthermore, only a red-shift of ~2.5 nm occurs. This much smaller red-shift is on-par with what would be expected from just an environmental refractive index change indicating that there is no diffusion of vapor into the fiber because the crosslinking process prevents it. This changes the sensing process from being caused by diffusion to being caused by an environmental refractive index change. If the concentration of the solvent vapor in air were controlled, a much more comprehensive study could be completed on these fibers. After about 10 minutes, the peak began to shift back towards its initial position, again this is believed to be due to methanol diffusing out of the chamber. At 17 minutes, the top of the chamber was removed and the sample was allowed to return to its initial location.

5.3.7.3 Refractive Index Sensing in Aqueous with Crosslinked Fibers

The fibers were placed in a water bath to perform RI sensing experiments. A WGM fiber resonator was placed in a water bath, as in Figure 5.11a. Following immersion, Q values shrunk by roughly a factor of 9 and FSR decreased slightly due to the sizable reduction in RI difference between the cavity and its surroundings. Notably, once submerged, resonance wavelengths were invariant in the water bath, thus supporting optical microscopy evidence that cross-linked fibers were water stable. Ethanol was added to the water bath in 10% (v/v) increments. As shown in Figure 5.11b, a

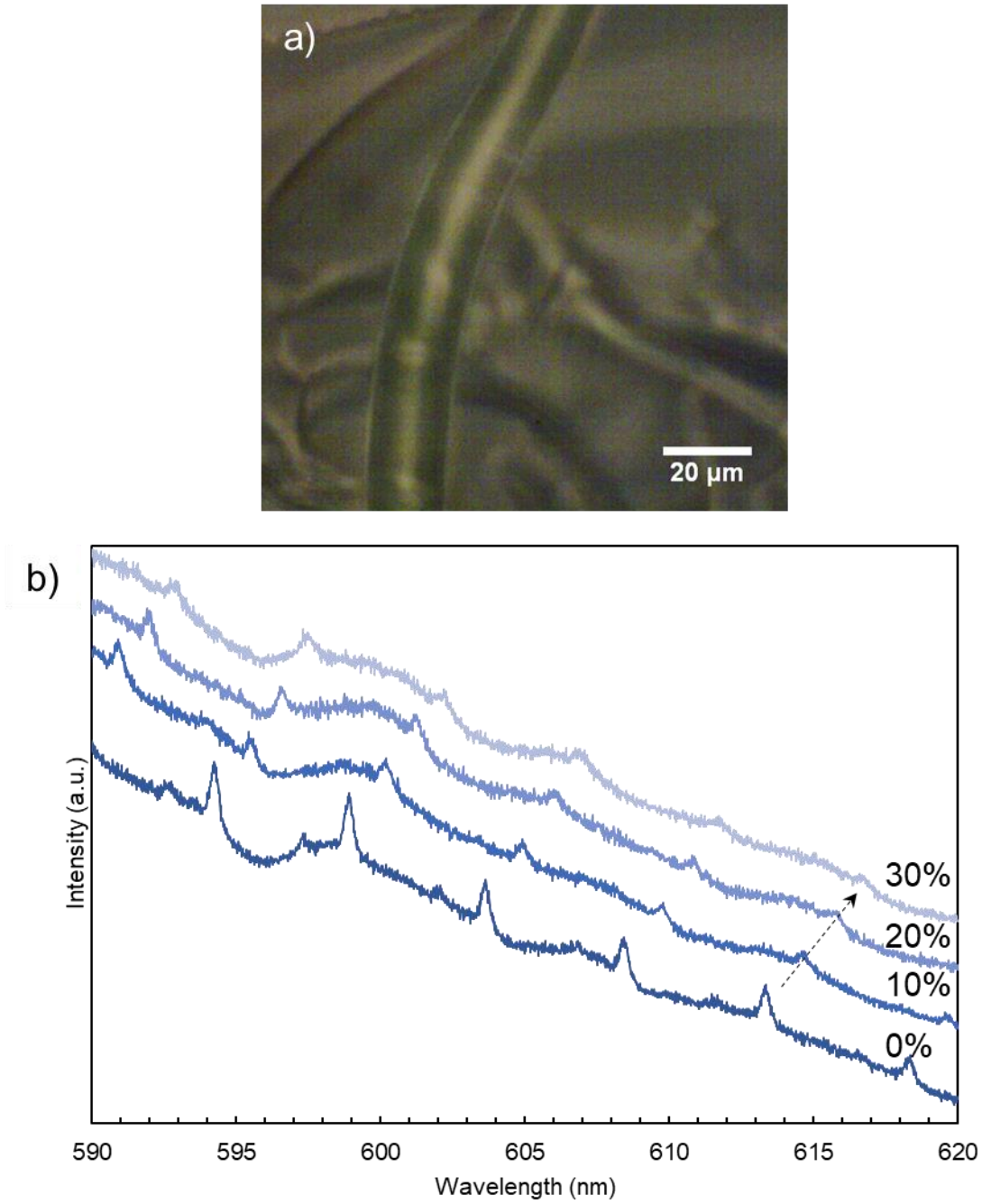

Figure 5.11: a) 15.9 µm fiber submerged in water used for sensing ethanol, b) stacked spectra showing peak shift at different ethanol concentrations by volume in water.

corresponding red-shift of the WGMs was observed with each addition, as indicated by the black dashed arrow. The position of the peak, initially at 613.5 nm, was plotted as a function of time in Figure 5.12a. Immediately after the addition of ethanol, the resonant wavelength increased by a few nanometers, then stabilized. Evaporation losses at higher ethanol concentrations resulted in small, but discernable blue-shifts at longer measurement times. Figure 5.12b depicts the resonance wavelength of the several peaks at increasing wavelengths versus solution refractive index. The refractive indices of water-ethanol solutions were calculated using well-known optical constants[106]. The spectral response of the resonator was linear within the range of ethanol concentrations evaluated. Furthermore, the sensitivity can be seen increasing as the resonant wavelength increases, corroborating the FDTD simulation data showing that longer wavelengths will have a larger evanescent wave. The highest fiber sensitivity was over 190 nm/RIU, on par with reports for similar active polymer-based WGM devices[17,19,24,28,107].

Another sensing experiment was performed on a slightly larger fiber (18.3 μm). The results are shown in Figure 5.13. The spectra shown in Figure 5.13a show that the presence of groups of peaks also remained, indicating that the water system would not suppress the peak groups. As ethanol was added in 10 vol% increments, the peak wavelength red-shifts accordingly. Figure 5.13b shows peak position of the 594 nm peak plotted as a function of RI. The fiber gave a sensitivity of 156.8 nm/RIU, which is comparable with previous reports, though not as high as the previous experiment. The reason for the lower sensitivity fiber is simply a result of the fiber being larger. Another observation, shown by the first data point in Figure 5.13c, is that this resonator's Q factor

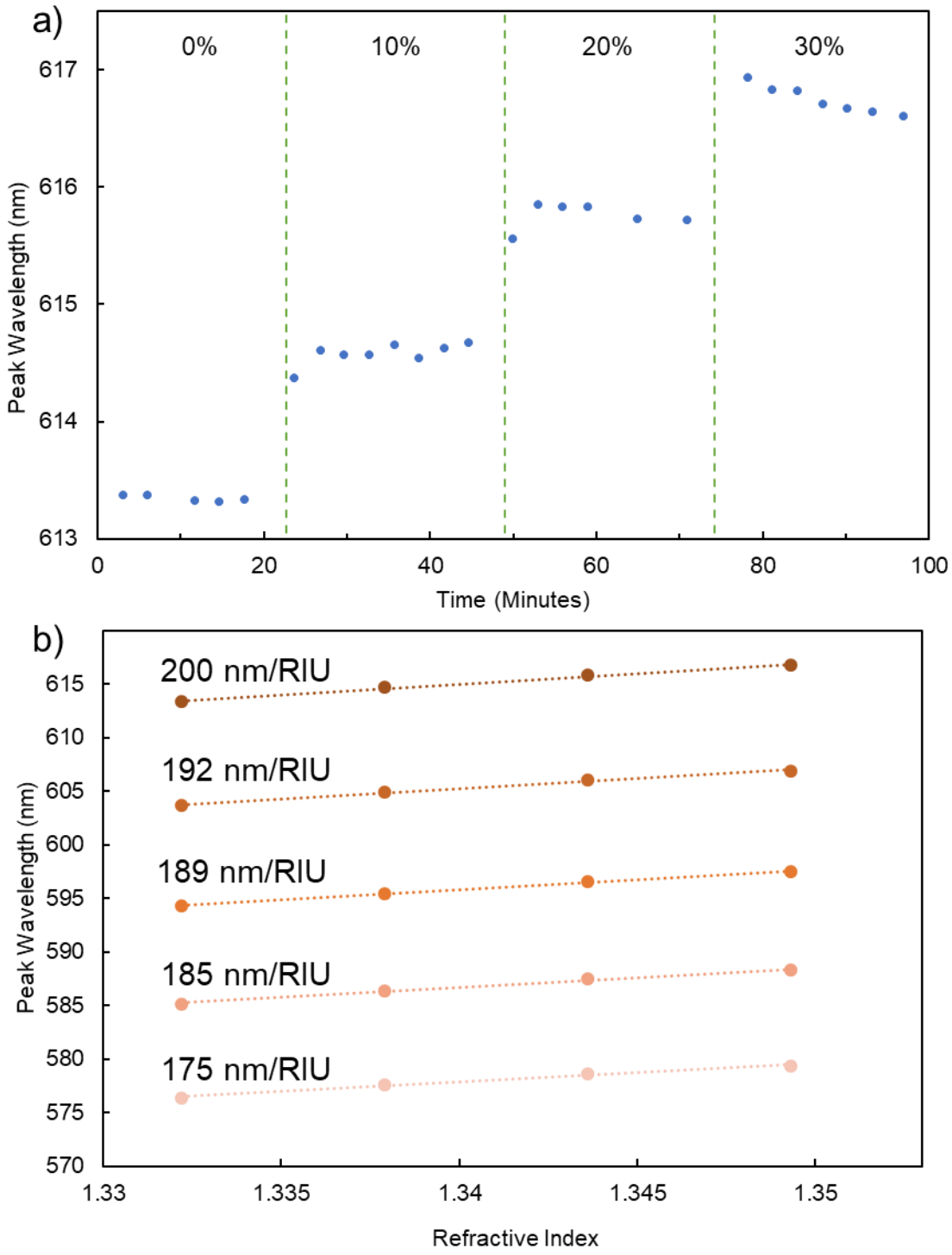

Figure 5.12: a) Plot monitoring peak shift with additions of ethanol, and b) plot monitoring peak position at different ethanol concentrations showing a sensitivity as high as nm/RIU.

is over 7,500, almost twice that of the previous resonator. Figure 5.13c shows the reduction in resonator Q factor with increased environmental RI. The reduction in Q factor is explained by the reduced RI mismatch between resonator and environment as the ethanol concentration is increased.

5.5 Conclusions

The R6G displayed bright fluorescence and uniform distribution down the length of the fibers. μPL experiments showed that the broad fluorescence emission of these fibers was decorated by groups of high Q peaks. These resonances were ascribed to WGMs which circulated around the fiber circumference, as well as spiral or conical modes with small longitudinal components and slightly smaller wavelengths. Additional studies are needed to minimize axial components and simplify the spectra of these optically active resonators. A mode fitting process and FSR analysis were performed to confirm that these resonances were WGMs. The FSR analysis showed these resonators were in good agreement with the FDTD simulations. Peaks were fit with a Lorentzian curve to determine Q factor. As-spun fibers displayed Q factors over 14,000 and the crosslinked fibers displayed Qs over 19,700. Table 2 shows that these Q factors are very competitive with other emitter-doped polymer resonators. Furthermore, the table shows that these resonators are relatively small when compared to other resonators, indicating that they may have even lower surface roughness[71,100] and greater sensitivity[13] than many

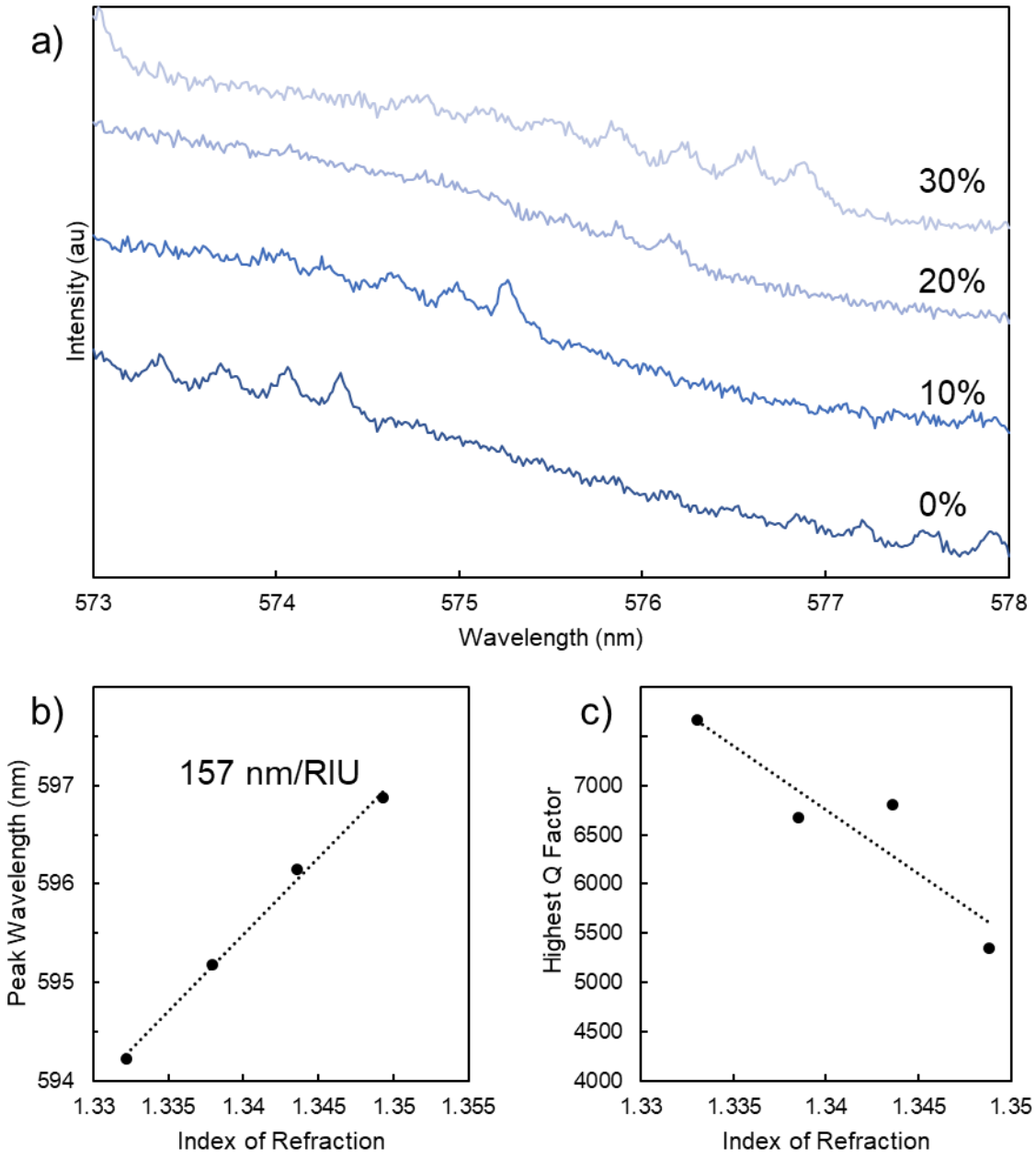

Figure 5.13: a) Stacked spectra presence of groups of peaks as well as peak shift with increased ethanol concentration of an 18.3 µm fiber, b) plot showing peak wavelength vs RI of sensing experiment showing sensitivity of 156.8 nm/RIU, and c) plot showing reduced Q factor with increased solution RI.

other polymer WGM resonators. A lasing experiment showed that these fibers failed to break the lasing threshold due to the lack of photostability in fluorescent dyes. A yield experiment showed that, of the scanned fibers, 93.75% of them demonstrated WGMs.

Sensing experiments showed the ability of our resonators to sense IPA vapor. Under exposure to IPA vapor, the WGMs contained in the fibers first blue shifted, then red shifted, indicating that IPA diffusion into the resonator was likely causing cavity swelling, as well as a reduced n_{eff}. The peaks were shown to be able to return to their starting wavelengths after being returned to ambient conditions. One uncontrolled parameter in these vapor-diffusion experiments was the concentration of the organic solvent vapor. Because the concentration could not be monitored, a more quantitative analysis of vapor sensing could not be performed. Future work should include measurements made with varied vapor concentrations to quantify device sensitivity for these applications.

Changing the vapor to methanol caused the diffusion process to occur more rapidly and the peak red-shift was much greater, likely due to the smaller size of the methanol molecule compared to the IPA molecule. Furthermore, using crosslinked fibers to sense methanol showed only a red-shift, indicating that crosslinking prevents vapor diffusion into the fibers.

To demonstrate refractive index sensing in aqueous, crosslinked R6G-PVA fibers were submerged in water. Despite emission spectrum complexity, refractive index sensing of the ethanol-water system exhibited a sensitivity of 200 nm/RIU. Since

Table 2: Chart comparing WGM devices based on Q factor and diameter.

Q	Material	Diameter (μm)	Source
21,400	Pyrromethene 597-Poly(methyl methacrylate) (PMMA)	40-65	Flatae et. al. 2015[108]
19,756	R6G-PVA	17.3	This Work
14,700	R6G-PMMA	500	Sun et. al. 2017[109]
11,800	R6G-PMMA	40	Grossmann et. al. 2010[16]
10,000	RhB-PMMA	280	Linslal et. al. 2015[49]
10,000	Nile Red and Pyrromethene-Polystyrene (PS)	10	Gonokami et. al. 1998[36]
9,410	Ethyl Orange-PVA	100	Li et. al. 2017[110]
8,200	R6G-PMMA	36	Ta et. al. 2013[17]
7,580	RhB-PMMA	150-1000	Anand et. al. 2017[48]
7,000	Nile red-PS	10	Francois et. al. 2015[19]
1,000	CdSe/ZnS Quantum Dots-PS	10	Beier et. al. 2009[47]

polymer materials can easily have other materials incorporated into their solutions, these devices may be able to be tailored to perform biosensing by adding receptor molecules such as antibodies to the polymer solutions before spinning. Those receptor molecules may be displayed on the surface of the resonators and allow for detectable binding

events. Due to the orderly and controlled deposition, these devices may also find future applications in multiplexed sensing if fibers with different receptors can be deposited closely enough to simultaneously be measured. Lastly, due to their high Q factors and easy fabrication, as well as the ability to incorporate other materials, such as quantum dots and rare-earth ions, these devices may find use in other optical applications such as microlasers.

Chapter 6. Conclusions

This work shows that we have developed a method for fabricating micron-scale R6G doped PVA fibers via NFES that support high-Q WGM resonance in their cross-sections. The fiber cross-sections were first simulated with FDTD, then fabricated and studied for their morphological and optical properties. To demonstrate application of the fibers, the resonator was first used as an organic solvent vapor sensor. The fibers were also crosslinked to make them water insoluble and demonstrated further application as sensors in aqueous environments.

Our literature review found that NFES, only having been around since 2006[65], has already demonstrated utility in fabricating fiber meshes[66], as well as its ability to suspend fibers between posts just a few tens of microns in diameter[67], and in a few optical applications[66]. Despite its usefulness, it has not been previously used to fabricate polymer fibers capable of sustaining WGMs in their cross-sections. This process was attractive for our purposes because of its facile, controlled deposition and scalability in easily producing many resonators in a compact area, which may provide future applications for device manufacturing and potentially with multiplexed devices, as discussed below.

The first objective of this study was to determine what polymer material our resonators should be fabricated from. Because it is a well-studied polymer capable of being easily electrospun[59,74,77,86,87] and has the advantages of being water-soluble, non-toxic, biodegradable, and low-cost, PVA was thus chosen. Rhodamine 6G is a ubiquitous

dye because of its high photostability, high quantum efficiency, and water solubility and was therefore chosen as well.

Before fabricating any fibers, the appropriate size of resonator that could produce a high-quality resonance for in-air and in-aqueous applications needed to be determined. To do this, FDTD simulations were performed and their spectra were analyzed for FSR, Q factors, evanescent field penetration, and field profiles. The simulations showed that high-Q resonators would have to be at least 4 μm in diameter for in-air systems and 10 μm for in-aqueous systems. They also showed a 1/diameter trend with FSR and an increasing Q factor with diameter that were compared with the experimentally obtained values later. The evanescent field penetration was reduced with higher diameters, indicating that larger resonators would be less sensitive. Conversely, the evanescent field penetration was greater at longer wavelengths of individual resonators, indicating that the longer wavelength modes would provide greater sensitivity. They gave insight into evanescent field penetration with changing fiber diameter so that fibers could be suspended over trench that was deep enough to prevent unwanted coupling.

The first step for device fabrication was to mix PVA solutions and characterize for their physicochemical and optical properties with and without the presence of R6G. Viscosity, surface tension, and conductivity measurements were determined to be consistent across all R6G-doped and undoped samples, indicating the process for solution mixing was robust as well as indicating that the presence of R6G did not significantly affect the solution and would not affect fiber fabrication during electrospinning. A substantial change in viscosity over time was observed, likely due to hydrogen bonding

among PVA molecules in the solutions, however, this was later shown to not have an impact on fiber diameters during electrospinning. The solutions were also spin coated onto glass slides where optical characterizations revealed that a concentration of 3.5 mgR6G/gPVA gave the highest absorption at 532 nm, where excitation would occur and the highest emission at 580 nm, where WGMs were anticipated, indicating that this concentration would best produce resonance among the concentrations analyzed. Furthermore, refractive index measurements gave values near 1.464 at all R6G concentrations, showing that the presence of the R6G had no noticeable effect on the RI, reinforcing that the incorporation of R6G would not greatly impact resonance, regardless of the range of concentrations analyzed. Furthermore, the RI measured was slightly lower than what was used in FDTD simulations, which suggested that values for n_{eff} and FSR may have been higher than what would be obtained experimentally.

For fiber fabrication, the NFES process was employed and fiber formation was characterized with the stage speed, applied voltage, and substrate material. As determined by the FDTD simulations, the goal was to produce fibers with diameters around 4 μm or greater. Initial characterization was done on SiO_2/Si substrates and showed that, while applied voltage had little effect on fiber diameter, by varying the stage speed, the fiber diameters could be manipulated to produce fibers larger than 20 μm. The incorporation of R6G, as predicted by solution characterization, did not significantly affect fiber size and the large fibers were able to be produced. Lastly, changing the collection substrate from 0.5 mm thick SiO_2/Si to 1 mm thick glass and performing the same diameter vs stage speed experiment showed nearly identical diameters produced on either substrate. SEM

images showed that the fibers can be suspended over scribe marks, have smooth surfaces, and have very circular cross-sections and relatively smooth surfaces. The fibers also had a gradual taper along the z-axis, which was shown to influence the spectra in subsequent experiments. Crosslinking and subsequent characterization was performed on the fibers. The fibers demonstrated the presence of the crosslinking agent, glutaraldehyde, as well as water stability. SEM characterization showed no noticeable change in fiber's surface roughness after crosslinking. Furthermore, optical characterization showed the fibers became larger and slightly more disorderly, though, this was not expected to prevent resonance capabilities.

Confocal fluorescence imaging showed uniform R6G distribution, indicating that there were no aggregates that may negatively impact resonance. Upon measuring for resonance with a μPL system, distinct peak groups of peaks with identical polarization on top of the R6G fluorescence were observed. Those FSRs over a breadth of fiber diameters agreed well with the FSRs from the FDTD simulations. Furthermore, a mode fitting analysis showed the peaks were determined to be WGMs. The groups of peaks are thought to be spiral or conical shaped cavities that exist along the z-axis of the fibers. Calculating the Q factors from the spectra showed a linear increase in Q with increasing diameter, indicating that surface roughness is likely the limiting factor on Q. Qs as high as 14,191 were found for the as-spun case and over 19,500 for the crosslinked fibers, which is among the best measured Q factors for dye-doped polymer WGM resonators. Furthermore, a yield experiment showed that 30 out of 32 fibers measured displayed WGMs, giving a yield of 93.75%. Sensing experiments showed the ability of the fibers to

detect isopropanol vapor. Lasing experiments showed the fibers did not achieve lasing due to the lack of a high enough photostability from the dye. During sensing experiments, the as-spun WGMs first displayed a blue-shift, followed by a red-shift. This trend, predicted by Foreman et. al.[105], indicates that the isopropanol vapor is diffusing into the fibers. When changed to methanol vapor, the process took place on a much shorter time scale. This is likely a result of the smaller size of the methanol molecule. When the crosslinked fiber was exposed to methanol vapor, only a red-shift was observed, indicating the vapor was no longer diffusing into the resonator. When the crosslinked fibers were placed in water, groups of peaks were still present and Q factors greater than 7,500 were displayed. The resonances displayed a red-shift when ethanol was introduced into the environment as well as a gradual reduction in Q factor. As predicted by FDTD simulations, the smaller fibers and longer wavelength modes were the most sensitive to environmental changes, displaying sensitivity as high as 190 nm/RIU.

R6G-doped PVA micron-scale fibers that displayed high-Q factor WGM resonance were successfully fabricated with an electrospinning process. These electrospun sensing devices present great potential for future multiplexed, highly sensitive devices with analyte specificity.

Chapter 7. Future Work

The most obvious avenue for future progress in this research is quantifying the fiber's sensitivity to organic vapor concentrations, as this is believed to be a highly sensitive detection method, being able to detect concentrations as low as attoliters[105]. Furthermore, the case study in the report used a resonator with diameter of 50 µm. Since sensitivity is known to increase with a reduced diameter while maintaining a high Q factor[13] and these resonators demonstrate viable resonance for diameters below 4 µm, sensitivity may be much greater.

Another future application is to obtain sensing specificity. This can be done in a few different ways. For specificity in detecting vapor, one way is to fabricate resonators from two different polymer systems and to utilize the different diffusion mechanics of the polymers to differentiate the analyte gases[41]. If NFES could be utilized to electrospin resonators of two or more polymers close enough to each other to measure resonances from each fiber, this could be obtained.

Sensing specificity can also be obtained by incorporating into the resonator various receptor molecules that display binding affinity to specific analytes, such as antibodies or other biomolecules. Polymer materials are particularly attractive in this regard because of their ability to integrate receptor molecules such as oligonucleotides, antibodies, and aptamers to allow for label-free detection of the analyte[111–115]. Furthermore, WGMs have a high level of sensitivity, as some reports have shown the

detection of individual molecules, viruses, and even ions[29,34,116]. If a bioreceptor could be integrated into the resonator either by incorporating into the polymer solution before electrospinning or after the electrospinning via diffusion or direct deposition onto the resonator surface, these devices may show favorable biosensing capabilities.

Specifically, one type of bioreceptor that has often been used are viruses. Different viruses such as the tobacco mosaic virus and T4 phage can be genetically modified[117,118] and have been electrospun into PVA fibers[119]. A particularly attractive receptor molecule is the M13 bacteriophage virus. This is a filamentous virus that has two genetically modifiable proteins: its pVIII major coat protein and pIII minor coat protein[120,121]. Specifically, the pVIII major coat protein has 2,700 copies along the 880 nm length of the virus that each serve as potential receptor. Furthermore, genetically modified M13 have already been shown to bind various biomolecules such as streptavidin, avidin, and β galactosidase[122] and have been electrospun into polymer fibers[123]. Because PVA is both water soluble and biocompatible, M13 could be electrospun into the fibers in this report and their ability to sense biomolecules can be assessed. Furthermore, because the M13 can be tailored to bind to different biomolecules and NFES has the potential to deposit fibers closely to each other, the potential for having multiplexed sensing can also be explored.

Another application of these fibers comes from the perspective of their applications as microlasers. The R6G-PVA fibers failed to produce lasing due to the R6G dye not being photostable under cw excitation. However, dye-doped polymer resonators

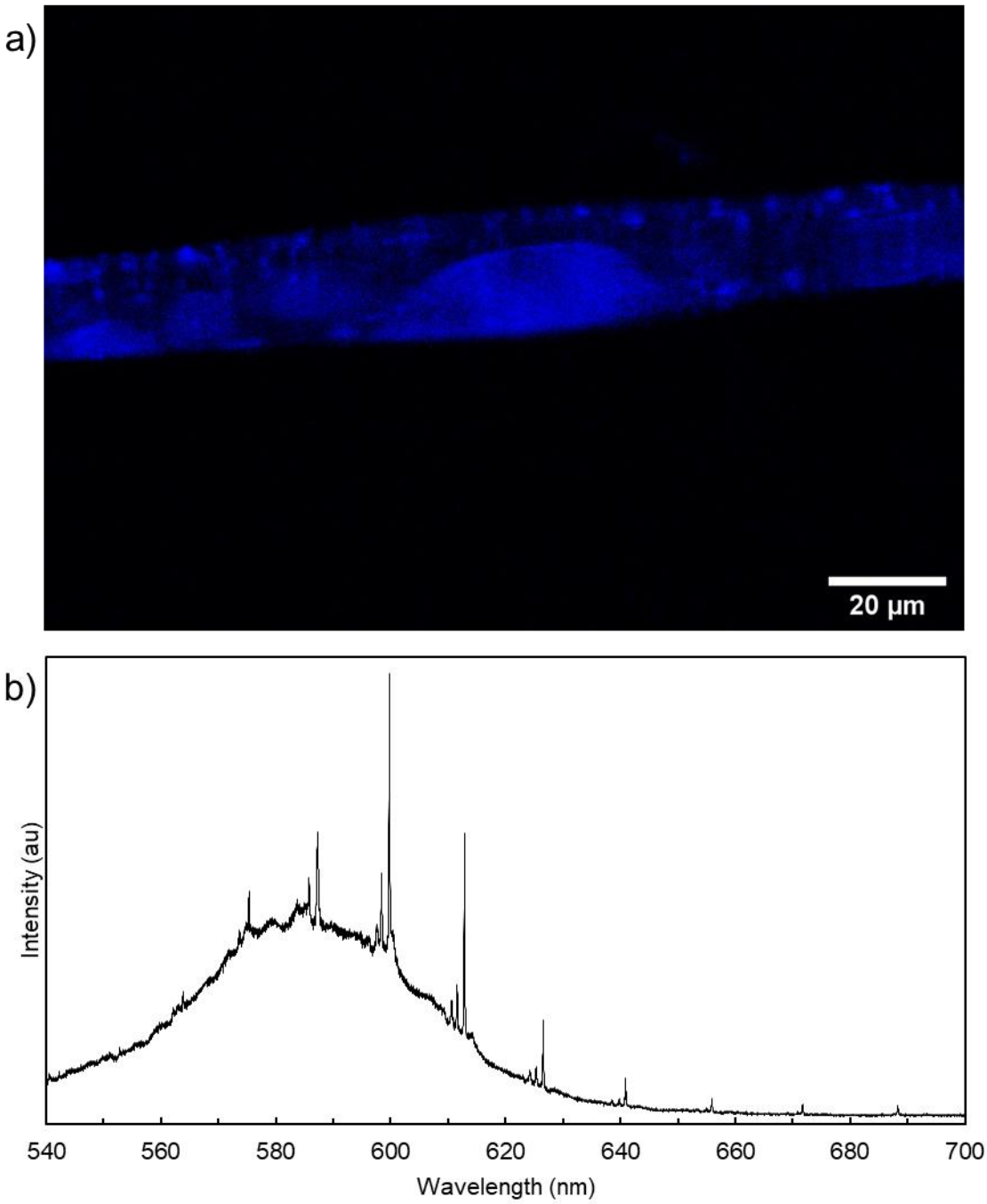

Figure 7.1 a) Confocal fluorescence image of CdSe QD doped fiber and b) spectra of fiber showing WGMs along the QD fluorescence backbone.

have shown lasing many times under pulsed excitation[16,58,124,125]. Furthermore, resonator Q factor can be expected to increase an order of magnitude above lasing threshold[126], meaning that these resonators may display Q factors ~10^5, which would be among the best resonance for dye doped polymer WGM devices.

Alternatively, a more photostable emitter such as quantum dots or rare-earth ions could be incorporated into the resonators. Already, QDs have been demonstrated in WGM resonators[37,47,127,128] and have been electrospun in polymer fibers[129–132]. Briefly, octadecylamine coated CdSe QDs were incorporated as the emitter into the NFES PVA fibers. Figure 7.1a shows a confocal fluorescence image of a fiber electrospun with these QDs. Unlike with the R6G case, the QD fibers show clear regions of emitter agglomeration, likely due to their lack of water solubility, which would hinder their resonance capabilities. Despite this, the fibers show strong fluorescence all along the fiber. These fibers also displayed WGM resonance with extremely high signal-to-noise and Q factors greater than 5,100 (competitive with the literature) at the 611 nm peak as shown in Figure 7.1b. Resonance from QDs would likely have lower Q factors than dye due to them being a more likely location to scatter light. This resonator was able to be excited with much higher powers than dye and remained impervious to photobleaching. However, lasing experiments showed that these fibers still failed to produce lasing. This is likely the result Auger recombination and thermal runaway, which has been shown to be the restricting factor in QD microlasers[20,133–135]. Nonetheless, this serves as strong proof-of-concept for incorporating QDs as emitters into these NFES fibers. Furthermore, the surfaces of QDs can be functionalized to include binding materials such as antibodies.

If these functionalized QDs are electrospun with PVA into fibers, it may facilitate an easily fabricated biosensor.

Bibliography

1. Vahala, K. J. Optical microcavities. *Nature* **424,** 839–846 (2003).
2. Meier, M. *et al.* Laser action from two-dimensional distributed feedback in photonic crystals. *Appl. Phys. Lett.* **74,** 7–9 (1999).
3. Kanno, E. *et al.* Twin-mirror membrane distributed-reflector lasers using 20-μm-long active region on Si substrates. *Light. Technol. Opt. EXPRESS J.* (2013). doi:10.1364/OE.26.001268
4. Russell, P. Photonic crystal fibers. *Science* **299,** 358–62 (2003).
5. Akahane, Y., Asano, T., Song, B. S. & Noda, S. High-Q photonic nanocavity in a two-dimensional photonic crystal. *Nature* **425,** 944–947 (2003).
6. Rayleigh, Lord. The problem of the whispering gallery. *Philos. Mag. Ser. 6* **20,** 1001–1004 (1910).
7. Imamura, S. *et al.* Optical control of individual carbon nanotube light emitters by spectral double resonance in silicon microdisk resonators. **161102,** (2013).
8. Jones, B. D. *et al.* Splitting and lasing of whispering gallery modes in quantum dot micropillars. *Opt. Express* **18,** 22578 (2010).
9. Mccall, S. L. *et al.* Whispering - gallery mode microdisk lasers Whispering-gallery mode microdisk lasers. **289,** 1–4 (2014).
10. Haberer, E. D. *et al.* Free-standing, optically pumped, GaN/InGaN microdisk lasers fabricated by photoelectrochemical etching. *Appl. Phys. Lett.* **85,** 5179–5181 (2004).
11. Kipp, T., Welsch, H., Strelow, C., Heyn, C. & Heitmann, D. Optical modes in semiconductor microtube ring resonators. *Phys. Rev. Lett.* **96,** 1–4 (2006).
12. Srinivasan, K., Stintz, A., Krishna, S. & Painter, O. Photoluminescence measurements of quantum-dot-containing semiconductor microdisk resonators using optical fiber taper waveguides. *Phys. Rev. B - Condens. Matter Mater. Phys.* **72,** 1–10 (2005).
13. Vollmer, F. & Arnold, S. Whispering-gallery-mode biosensing: Label-free detection down to single molecules. *Nat. Methods* **5,** 591–596 (2008).
14. Senthil Murugan, G., Wilkinson, J. S. & Zervas, M. N. Selective excitation of whispering gallery modes in a novel bottle microresonator. *Opt. Express* **17,** 11916 (2009).

15. Navarro-Urrios, D. *et al.* Local characterization of rare-earth-doped single microspheres by combined microtransmission and microphotoluminescence techniques. *J. Opt. Soc. Am. B* **29,** 3293 (2012).

16. Grossmann, T. *et al.* Low-threshold conical microcavity dye lasers. *Appl. Phys. Lett.* **97,** 8–11 (2010).

17. Duong Ta, V., Chen, R., Ma, L., Jun Ying, Y. & Dong Sun, H. Whispering gallery mode microlasers and refractive index sensing based on single polymer fiber. *Laser Photon. Rev.* **7,** 133–139 (2013).

18. Armani, A. M., Srinivasan, A. & Vahala, K. J. Soft Lithographic Fabrication of High Q Polymer Microcavity Arrays Soft Lithographic Fabrication of High Q Polymer Microcavity Arrays. (2016). doi:10.1021/nl0708359

19. François, A., Riesen, N., Ji, H., Afshar V., S. & Monro, T. M. Polymer based whispering gallery mode laser for biosensing applications. *Appl. Phys. Lett.* **106,** (2015).

20. Wang, Y. *et al.* Robust Whispering-Gallery-Mode Microbubble Lasers from Colloidal Quantum Dots. *Nano Lett.* **17,** 2640–2646 (2017).

21. Ta, V. D., Chen, R. & Sun, H. Coupled polymer microfiber lasers for single mode operation and enhanced refractive index sensing. *Adv. Opt. Mater.* **2,** 220–225 (2014).

22. Choi, H. & Armani, A. M. Raman–Kerr frequency combs in Zr-doped silica hybrid microresonators. *Opt. Lett.* **43,** 2949 (2018).

23. Savchenkov, A. A., Liang, W., Ilchenko, V., Matsko, A. & Maleki, L. Crystalline Waveguides for Optical Gyroscopes. *IEEE J. Sel. Top. Quantum Electron.* **24,** (2018).

24. Wienhold, T. *et al.* Lab on a Chip whispering-gallery mode microgoblet lasers. 3800–3806 (2015). doi:10.1039/c5lc00670h

25. Bischler, R., Olszyna, M., Himmelhaus, M. & Dähne, L. Development of a fully automated in-vitro diagnostics system based on low-Q whispering gallery modes in fluorescent microparticles. *Eur. Phys. J. Spec. Top.* **223,** 2041–2055 (2014).

26. Gregor, M. *et al.* Refractometric sensors based on microsphere resonators. *Appl. Phys. Lett.* **96,** 231102 (2010).

27. Zamora, V., Díez, A., Andrés, M. V & Gimeno, B. Refractometric sensor based on whispering-gallery modes of thin capillarie. *Opt. Express* **15,** 12011–6 (2007).

28. Ta, V. D., Chen, R. & Sun, H. D. Tuning Whispering Gallery Mode Lasing from Self-Assembled Polymer Droplets. *Sci. Rep.* **3,** 1362 (2013).

29. Vollmer, F., Arnold, S. & Keng, D. Single virus detection from the reactive shift of a whispering-gallery mode. *Proc. Natl. Acad. Sci. U. S. A.* **105,** 20701–4 (2008).

30. Shao, L. *et al.* Detection of single nanoparticles and lentiviruses using microcavity resonance broadening. *Adv. Mater.* **25,** 5616–5620 (2013).

31. Baaske, M. D., Foreman, M. R. & Vollmer, F. Single-molecule nucleic acid interactions monitored on a label-free microcavity biosensor platform. *Nat. Nanotechnol.* **9,** 933–939 (2014).

32. Armani, A. M., Kulkarni, R. P., Fraser, S. E., Flagan, R. C. & Vahala, K. J. Label-free, single-molecule detection with optical microcavities. *Science (80-.).* **317,** 783–787 (2007).

33. He, L., Özdemir, Ş. K., Zhu, J., Kim, W. & Yang, L. Detecting single viruses and nanoparticles using whispering gallery microlasers. *Nat. Nanotechnol.* **6,** 428–432 (2011).

34. Baaske, M. D. & Vollmer, F. Optical observation of single atomic ions interacting with plasmonic nanorods in aqueous solution. *Nat. Photonics* **10,** 733–739 (2016).

35. Huckabay, H. A. & Dunn, R. C. Whispering gallery mode imaging for the multiplexed detection of biomarkers. *Sensors Actuators, B Chem.* **160,** 1262–1267 (2011).

36. Kuwata-Gonokami, M. & Takeda, K. Polymer whispering gallery mode lasers. *Opt. Mater. (Amst).* **9,** 12–17 (1998).

37. Pang, S., Beckham, R. E. & Meissner, K. E. Quantum dot-embedded microspheres for remote refractive index sensing. *Appl. Phys. Lett.* **92,** 22–24 (2008).

38. Ristić, D. *et al.* Photoluminescence and lasing in whispering gallery mode glass microspherical resonators. *J. Lumin.* (2016). doi:10.1016/j.ecolind.2018.06.049

39. Lu, T., Yang, L., van Loon, R. V. A., Polman, A. & Vahala, K. J. On-chip green silica upconversion microlaser. *Opt. Lett.* (2009). doi:10.1364/OL.34.000482

40. Foreman, M. R. & Vollmer, F. Optical tracking of anomalous diffusion kinetics in polymer microspheres. *Phys. Rev. Lett.* **114,** (2015).

41. Sun, Y., Shopova, S. I., Frye-Mason, G. & Fan, X. Rapid chemical-vapor sensing using optofluidic ring resonators. *Opt. Lett.* **33,** 788–90 (2008).

42. Ksendzov, A., Homer, M. L. & Manfreda, A. M. Integrated optics ring-resonator chemical sensor with polymer transduction layer. *Electron. Lett.* **40,** 63–65 (2004).

43. Grossmann, T. *et al.* High-Q conical polymeric microcavities. *Appl. Phys. Lett.* **96,** (2010).

44. Chandrahalim, H. & Fan, X. Reconfigurable Solid-state Dye-doped Polymer Ring Resonator Lasers. *Sci. Rep.* **5,** 1–8 (2015).

45. Kawabe, Y. *et al.* Whispering-gallery-mode microring laser using a conjugated polymer. *Appl. Phys. Lett.* **72,** 141–143 (1998).

46. Jordan, R. H., Dodabalapur, A., Katz, H. E., Schilling, M. L. & Slusher, R. E. Polymer microdisk and microring lasers. *Opt. Lett.* **20,** 2093–2095 (1995).

47. Beier, H. T., Coté, G. L. & Meissner, K. E. Whispering gallery mode biosensors consisting of quantum dot-embedded microspheres. *Ann. Biomed. Eng.* **37,** 1974–1983 (2009).

48. Anand, V. R., Mathew, S., Samuel, B., Radhakrishnan, P. & Kailasnath, M. Thermo-optic tuning of whispering gallery mode lasing from a dye-doped hollow polymer optical fiber. *Opt. Lett.* **42,** 2926–2929 (2017).

49. Linslal, C. L. *et al.* Microring embedded hollow polymer fiber laser. *Appl. Phys. Lett.* **106,** (2015).

50. Gu, F. *et al.* Single whispering-gallery mode lasing in polymer bottle microresonators via spatial pump engineering. *Light Sci. Appl.* **6,** 1–7 (2017).

51. Polyanskiy, M. Refractive index database. *RefractiveIndex.INFO* http://refractiveindex.info/?group=LIQUIDS&materia (2008).

52. Liu, D. *et al.* Facile preparation of soy protein/poly(vinyl alcohol) blend fibers with high mechanical performance by wet-spinning. *Ind. Eng. Chem. Res.* **52,** 6177–6181 (2013).

53. Paradossi, G., Cavalieri, F., Chiessi, E., Spagnoli, C. & Cowman, M. K. Poly(vinyl alcohol) as versatile biomaterial for potential biomedical applications. in *Journal of Materials Science: Materials in Medicine* **14,** 687–691 (2003).

54. Jaffe, H. L. & Rosenblum, F. M. Poly(Vinyl Alcohol) for Adhesives. in *Handbook of Adhesives* (ed. Skeist, I.) 401–407 (Springer US, 1990). doi:10.1007/978-1-4613-0671-9_22

55. Kubin, R. F. & Fletcher, A. N. Fluorescence quantum yields of some rhodamine dyes. *J. Lumin.* **27,** 455–462 (1982).

56. Igarashi, K. *et al.* Operation of rhodamine 6g dye laser in water solution. *Jpn. J. Appl. Phys.* **34,** 3093–3096 (1995).

57. Csaba, N., Sánchez, A. & Alonso, M. J. PLGA: Poloxamer and PLGA: Poloxamine blend nanostructures as carriers for nasal gene delivery. *J. Control. Release* **113,** 164–172 (2006).

58. Wan, L. *et al.* On-chip, high-sensitivity temperature sensors based on dye-doped solid-state polymer microring lasers. *Appl. Phys. Lett.* **111,** 061109 (2017).

59. Bhardwaj, N. & Kundu, S. C. Electrospinning: A fascinating fiber fabrication technique. *Biotechnol. Adv.* **28,** 325–347 (2010).

60. Das, A. J., Lafargue, C., Lebental, M., Zyss, J. & Narayan, K. S. Three-dimensional microlasers based on polymer fibers fabricated by electrospinning. *Appl. Phys. Lett.* **99,** 2009–2012 (2011).

61. Krämmer, S. *et al.* Random-cavity lasing from electrospun polymer fiber networks. *Adv. Mater.* **26,** 8096–8100 (2014).

62. Camposeo, A. *et al.* Laser emission from electrospun polymer nanofibers. *Small* **5,** 562–566 (2009).

63. Ubaid, S., Liao, F., Linghu, S., Yu, J. & Gu, F. Electrospun polymer bottle microresonators for stretchable single-mode lasing devices. *Opt. Lett.* **43,** 3128–3131 (2018).

64. Krämmer, S. *et al.* Electrospun Polymer Fiber Lasers for Applications in Vapor Sensing. *Adv. Opt. Mater.* **5,** 1–5 (2017).

65. Sun, D., Chang, C., Li, S. & Lin, L. Near-field electrospinning. *Nano Lett.* **6,** 839–842 (2006).

66. Di Camillo, D. *et al.* Near-field electrospinning of light-emitting conjugated polymer nanofibers. *Nanoscale* **5,** 11637 (2013).

67. Bisht, G. S. *et al.* Controlled continuous patterning of polymeric nanofibers on three-dimensional substrates using low-voltage near-field electrospinning. *Nano Lett.* **11,** 1831–1837 (2011).

68. Tamboli, A. C. *et al.* Room-temperature continuous-wave lasing in GaNInGaN microdisks. *Nat. Photonics* (2007). doi:10.1038/nphoton.2006.52

69. Mexis, M. *et al.* High quality factor nitride-based optical cavities: microdisks with embedded GaN/Al(Ga)N quantum dots. (2011).

70. Braginsky, V. B., Gorodetsky, M. L. & Ilchenko, V. S. Quality-factor and nonlinear properties of optical whispering-gallery modes. *Phys. Lett. A* **137,** 393–397 (1989).

71. Gorodetsky, M. L., Savchenkov, A. A. & Ilchenko, V. S. Ultimate Q of optical microsphere resonators. *Opt. Lett.* **21,** 453 (1996).

72. Slusher, R. E. *et al.* Threshold characteristics of semiconductor microdisk lasers. *Appl. Phys. Lett.* **63,** 1310–1312 (1993).

73. Deitzel, J. M., Kleinmeyer, J., Harris, D. & Beck Tan, N. C. The effect of processing variables on the morphology of electrospun nanofibers and textiles. *Polymer (Guildf).* **42,** 261–272 (2001).

74. Koski, A., Yim, K. & Shivkumar, S. Effect of molecular weight on fibrous PVA produced by electrospinning. *Mater. Lett.* (2004). doi:10.1016/S0167-577X(03)00532-9

75. Gao, H.-W., Yang, R.-J., He, J.-Y. & Yang, L. Rheological Behaviors of PVA/H2O Solutions of High-Polymer Concentration. *J. Appl. Polym. Sci.* **116,** 1459–1466 (2010).

76. Song, S. I. & Kim, B. C. Characteristic rheological features of PVA solutions in water-containing solvents with different hydration states. *Polymer (Guildf).* **45,** 2381–2386 (2004).

77. Tao, J. Effects of Molecular Weight and Solution Concentration on Electrospinning of PVA. *Master Thesis, Mater. Sci. Eng. Worcester Polytech. Inst.* 1–107 (2003).

78. Chang, C., Limkrailassiri, K. & Lin, L. Continuous near-field electrospinning for large area deposition of orderly nanofiber patterns. *Appl. Phys. Lett.* **93,** 1–3 (2008).

79. Bu, N., Huang, Y., Wang, X. & Yin, Z. Continuously tunable and oriented nanofiber direct-written by mechano-electrospinning. *Mater. Manuf. Process.* **27,** 1318–1323 (2012).

80. Zhou, F. L., Hubbard, P. L., Eichhorn, S. J. & Parker, G. J. M. Jet deposition in near-field electrospinning of patterned polycaprolactone and sugar-polycaprolactone core-shell fibres. *Polymer (Guildf).* **52,** 3603–3610 (2011).

81. Wang, H., Zheng, G., Li, W., Wang, X. & Sun, D. Direct-writing organic three-dimensional nanofibrous structure. *Appl. Phys. A Mater. Sci. Process.* **102,** 457–461 (2011).

82. Gupta, P., Elkins, C., Long, T. E. & Wilkes, G. L. Electrospinning of linear homopolymers of poly(methyl methacrylate): Exploring relationships between fiber formation, viscosity, molecular weight and concentration in a good solvent. *Polymer (Guildf).* (2005). doi:10.1016/j.polymer.2005.04.021

83. Hohman, M. M., Shin, M., Rutledge, G. & Brenner, M. P. Electrospinning and electrically forced jets. II. Applications. *Phys. Fluids* (2001). doi:10.1063/1.1384013

84. Casper, C. L., Stephens, J. S., Tassi, N. G., Chase, D. B. & Rabolt, J. F. Controlling surface morphology of electrospun polystyrene fibers: Effect of humidity and molecular weight in the electrospinning process. *Macromolecules* (2004). doi:10.1021/ma0351975

85. Wendorff, J. H., Agarwal, S. & Greiner, A. *Electrospinning: Materials, Processing, and Applications*. *Electrospinning: Materials, Processing, and Applications* (2012). doi:10.1002/9783527647705

86. Shaikh, R. P., Kumar, P., Choonara, Y. E., Du Toit, L. C. & Pillay, V. Crosslinked electrospun PVA nanofibrous membranes: Elucidation of their physicochemical, physicomechanical and molecular disposition. *Biofabrication* **4,** (2012).

87. Destaye, A. G., Lin, C. K. & Lee, C. K. Glutaraldehyde vapor cross-linked nanofibrous PVA mat with in situ formed silver nanoparticles. *ACS Appl. Mater. Interfaces* **5,** 4745–4752 (2013).

88. Pu, J., Yan, X., Jiang, Y., Chang, C. & Lin, L. Piezoelectric actuation of direct-write electrospun fibers. *Sensors Actuators, A Phys.* **164,** 131–136 (2010).

89. Martinelli, A. *et al.* Structural analysis of PVA-based proton conducting membranes. *Solid State Ionics* **177,** 2431–2435 (2006).

90. Dodda, J. M. *et al.* Comparative study of PVA/SiO2 and PVA/SiO2/glutaraldehyde (GA) nanocomposite membranes prepared by single-step solution casting method. *J. Mater. Sci.* **50,** 6477–6490 (2015).

91. Lam, C. C., Leung, P. T. & Young, K. Explicit asymptotic formulas for the positions, widths, and strengths of resonances in Mie scattering. *J. Opt. Soc. Am. B* **9,** 1585 (1992).

92. Sumetsky, M. Localization of light on a cone: theoretical evidence and experimental demonstration for an optical fiber. *Opt. Lett.* **36,** 145 (2011).

93. Sumetsky, M. Localization of light in optical fibers: Cylinder, conical and bottle microresonators. *Int. Conf. Transparent Opt. Networks* 1–4 (2011). doi:10.1109/ICTON.2011.5970932

94. Luan, F., Magi, E., Gong, T., Kabakova, I. & Eggleton, B. J. Photoinduced whispering gallery mode microcavity resonator in a chalcogenide microfiber. *Opt. Lett.* **36,** 4761–3 (2011).

95. Xie, F. *et al.* Single-mode lasing via loss engineering in fiber-taper-coupled polymer bottle microresonators. *Photonics Res.* **5,** B29 (2017).

96. Strelow, C. *et al.* Optical microcavities formed by semiconductor microtubes using a bottlelike geometry. *Phys. Rev. Lett.* **101,** 1–4 (2008).

97. Birks, T. A., Knight, J. C. & Dimmick, T. E. High-resolution measurement of the fiber diameter variations using whispering gallery modes and no optical alignment. *IEEE Photonics Technol. Lett.* **12,** 182–183 (2000).

98. Wang, J. *et al.* Tubular oxide microcavity with high-index-contrast walls: Mie scattering theory and 3D confinement of resonant modes. *Opt. Express* **20,** 18555–67 (2012).

99. Thyagarajan, K., Ghatak, A. K. & Brown, R. T. Lasers, Theory and Applications. *IEEE J. Quantum Electron.* **18,** 1983 (1982).

100. Borselli, M., Johnson, T. J. & Painter, O. Beyond the Rayleigh scattering limit in high-Q silicon microdisks: theory and experiment. *Opt. Express* **13,** 1515 (2005).

101. Anthamatten, M., Letts, S. a & Cook, R. C. Controlling surface roughness in vapor-deposited poly(amic acid) films by solvent-vapor exposure. *Langmuir* **20,** 6288–96 (2004).

102. Gardner, K. *et al.* Whispering gallery mode structure in polymer-coated lasing microspheres. *J. Opt. Soc. Am. B* **34,** 2140 (2017).

103. Schubert, M. *et al.* Lasing within Live Cells Containing Intracellular Optical Microresonators for Barcode-Type Cell Tagging and Tracking. *Nano Lett.* **15,** 5647–5652 (2015).

104. Siegle, T. *et al.* A comparison of various excitation and detection schemes for dye-doped polymeric whispering gallery mode micro-lasers. *Opt. Express* **26,** 3579–3593 (2017).

105. Foreman, M. R. & Vollmer, F. Optical Tracking of Anomalous Diffusion Kinetics in Polymer Microspheres. *Phys. Rev. Lett.* **114,** 118001 (2015).

106. Scott, T. A. Refractive index of ethanol-water mixtures and density and refractive index of ethanol-water-ethyl ether mixtures. *J. Phys. Chem.* **50,** 406–412 (1946).

107. Beck, T. *et al.* High-Q polymer resonators with spatially controlled photo-functionalization for biosensing applications. **121108,** (2017).

108. Flatae, A. M. *et al.* Optically controlled elastic microcavities. *Light Sci. Appl.* **4,** e282 (2015).

109. Sun, H., Zhang, H., Feng, G. & Zhou, H. Freestanding polymeric microdisk laser based on a microfiber knot. *Laser Phys. Latters* **055806,** (2017).

110. Li, Y. *et al.* Laser-tuned whispering gallery modes in a silica-based microsphere resonator integrated with ethyl-orange-doped polyvinyl alcohol coating. *Sensors Actuators, B Chem.* **238,** 98–104 (2017).

111. Hawk, R. M., Chistiakova, M. V & Armani, A. M. Monitoring DNA hybridization using optical microcavities. *Opt. Lett.* **38,** 4690–3 (2013).

112. Wu, Y., Zhang, D. Y., Yin, P. & Vollmer, F. Ultraspecific and highly sensitive nucleic acid detection by integrating a DNA catalytic network with a label-free microcavity. *Small* **10,** 2067–2076 (2014).

113. Luchansky, M. S. & Bailey, R. C. Rapid, multiparameter profiling of cellular secretion using silicon photonic microring resonator arrays. *J. Am. Chem. Soc.* **133,** 20500–20506 (2011).

114. Tajiri, T., Matsumoto, S., Imato, T., Okamoto, T. & Haraguchi, M. Optical characterization of the antigen-antibody thin layer using the whispering gallery mode. *Anal. Sci.* **30,** 799–804 (2014).

115. Pasquardini, L. *et al.* Whispering gallery mode aptasensors for detection of blood proteins. in *Progress in Biomedical Optics and Imaging - Proceedings of SPIE* **8576,** (2013).

116. Dantham, V. R. *et al.* Label-free detection of single protein using a nanoplasmonic-photonic hybrid microcavity. *Nano Lett.* **13,** 3347–3351 (2013).

117. Haynes, J. R. *et al.* Development of a Genetically–Engineered, Candidate Polio Vaccine Employing the Self–Assembling Properties of the Tobacco Mosaic Virus Coat Protein. *Biotechnology* **4,** 637–641 (1986).

118. Chan, L. Y., Kosuri, S. & Endy, D. Refactoring bacteriophage T7. *Mol. Syst. Biol.* **1,** E1–E10 (2005).

119. Salalha, W., Kuhn, J., Dror, Y. & Zussman, E. Encapsulation of bacteria and viruses in electrospun nanofibres. *Nanotechnology* **17,** 4675–4681 (2006).

120. Lee, S. K., Yun, D. S. & Belcher, A. M. Cobalt ion mediated self-assembly of genetically engineered bacteriophage for biomimetic Co - Pt hybrid material. *Biomacromolecules* **7,** 14–17 (2006).

121. Petrenko, V. a, Smith, G. P., Gong, X. & Quinn, T. A library of organic landscapes on filamentous phage. *Protein Eng.* **9,** 797–801 (1996).

122. Petrenko, V. a & Smith, G. P. Phages from landscape libraries as substitute antibodies. *Protein Eng.* **13,** 589–92 (2000).

123. Lee, S. W. & Belcher, A. M. Virus-based fabrication of micro- and nanofibers using electrospinning. *Nano Lett.* **4,** 387–390 (2004).

124. Ta, V. D., Chen, R. & Sun, H. D. Self-assembled flexible microlasers. *Adv. Mater.* **24,** (2012).

125. Sun, H. *et al.* Fabrication of Lasing Whispering Gallery Mode Microresonators by Controllable Injection Method. *IEEE Photonics J.* **9,** 1–6 (2017).

126. François, A., Riesen, N., Ji, H., Afshar V., S. & Monro, T. M. Polymer based whispering gallery mode laser for biosensing applications. *Appl. Phys. Lett.* **106,** (2015).

127. Wang, Y., Yang, S., Yang, H. & Sun, H. Quaternary Alloy Quantum Dots: Toward Low-Threshold Stimulated Emission and All-Solution-Processed Lasers in the Green Region. *Adv. Opt. Mater*. **3,** 652–657 (2015).

128. Beier, H. T., Coté, G. L. & Meissner, K. E. Dot Embedded Polystyrene Microspheres. **27,** 536–543 (2010).

129. Atabey, E. *et al.* Fluorescent electrospun polyvinyl alcohol/CdSe@ZnS nanocomposite fibers. *J. Compos. Mater*. **47,** 3175–3185 (2013).

130. Kim, N. *et al.* CuInS2/ZnS quantum dot-embedded polymer nanofibers for color conversion films. *J. Mater. Chem. C* **4,** 2457–2462 (2016).

131. Mahmoudifard, M., Shoushtari, A. M. & Shanehsaz, M. Quantum dot/polyvinyl alcohol composite nanofibers membrane as highly sensitive fluorescence quenching-based sensors. *Fibers Polym.* **15,** 1797–1803 (2014).

132. Başlak, C., Köysüren, Ö. & Kuş, M. Electrospun Nanofibers prepared with CdTe QDs, CdTeSe QDs and CdTe/CdS Core-shell QDs. *Celal Bayar Üniversitesi Fen Bilim. Derg.* **14,** 119–124 (2018).

133. Park, Y. S., Bae, W. K., Baker, T., Lim, J. & Klimov, V. I. Effect of Auger Recombination on Lasing in Heterostructured Quantum Dots with Engineered Core/Shell Interfaces. *Nano Lett.* (2015). doi:10.1021/acs.nanolett.5b02595

134. Kiraz, A., Chen, Q. & Fan, X. Optofluidic Lasers with Aqueous Quantum Dots. *ACS Photonics* **2,** 707–713 (2015).

135. Zubov, F. I. *et al.* Laser characteristics of an injection microdisk with quantum dots and its free-space outcoupling efficiency. *Semiconductors* **50,** 1408–1411 (2016).